Defect and coherent transient optical spectroscopy of rare earth doped crystals
by Guangming Wang

A thesis submitted in partial fulfillment of the requirements for the degree of Doctor of Philosophy in Physics
Montana State University
© Copyright by Guangming Wang (1997)

Abstract:
Spectral and structural properties of rare earth doped crystals have been investigated with white light absorption, fluorescence, fluorescence excitation, optically-detected nuclear-magnetic-resonance (ODNMR), photon echo and optical nutation.

Conventional spectroscopy was used to study Pr3+, Nd3+, Sm3+, Eu3+, Ho3+, Er3+ and Tm3"4" doped Y3Al5O12 crystals. Besides the intrinsic site spectroscopy, systematic studies on dopant ions in defect sites were carried out. There were generally 3-6 defect lines within ± 60 cm"1 of the intrinsic line. Quantitative optical absorption measurements showed that 4-7% of the dopants appeared in defect sites for the Eu3+, Ho3+, Er3+ and Tm3+ doped Y3Al5O12 crystals and 15-21% of the dopants appeared in defect sites for the Pr3+ and Nd3+ doped Y3Al5O12 crystals. These defects were attributed to the 1% of excess Y3+ substituting at Al3+ a sites (C3i symmetry) with a random distribution for Eu3+, Ho3+, Er3+ and Tm3"4" ions whose radii were close to Y3+ and a preferred distribution for Pr3+ and Nd3+ ions whose radii were much larger than Y3+.

Angle dependent ODNMR was used to determine the nuclear principal axis orientations of Pr3"4" ions in the intrinsic and defect sites of Pr3:Y3Al5O12. The intrinsic site has D2 symmetry which constrains the orientation of Pr3+ nuclear principal axes to specific directions. These directions were verified through ODNMR measurements. Using angle dependent ODNMR, one defect site was found to have C1 symmetry which is attributed to Y3+ substituting at Al3+ a sites.

Optical dephasing was studied for Tm3+:Y2Si2O7 as a function of temperature and laser excitation intensity via photon epho measurements. Temperature dependence of the optical dephasing was attributed to phonon coupling between the ground states 3H6(1) and 3H6(2) which were 6 cm"1 apart. Instantaneous spectral diffusion is another dephasing mechanism in this crystal. Using photon echoes, a homogeneous linewidth of 14 kHz was measured at 1.24 K for the 3H6(1) —> 3H4(1) transition. The relatively broad inhomogeneous linewidth of 100 GHz gave an inhomogeneous-to-homogeneous linewidth ratio of 7 x 106. This large ratio combined with a transition wavelength suitable for GaAlAs semiconductor lasers and the absence of hyperfine structure hole burning make this material an interesting candidate for time-domain signal processing and transient optically-addressed data storage.

Coherent transients were also studied for Tm3+:Y3Al5O12 via optical nutation measurements. Beats were observed due to the presence of several Rabi frequencies from the crystallographically-equivalent but orientationally-inequivalent crystal sites. Using symmetry considerations, we found for the first time that when the light electric field was along one of two special directions (111) and (001), the nutation had a single Rabi frequency. A general procedure for obtaining single Rabi frequency nutation (“single-dipole”) in arbitrary crystals is presented.

DEFECT AND COHERENT TRANSIENT OPTICAL SPECTROSCOPY OF RARE EARTH DOPED CRYSTALS

by

Guangming Wang

A thesis submitted in partial fulfillment
of the requirements for the degree

of

Doctor of Philosophy

in

Physics

MONTANA STATE UNIVERSITY
Bozeman, Montana

April, 1997

D378
W1853

APPROVAL

of a thesis submitted by

Guangming Wang

This thesis has been read by each member of the thesis committee and has been found to be satisfactory regarding content, English usage, format, citations, bibliographic style, and consistency, and is ready for submission to the College of Graduate Studies.

18 April 1997
Date

Rufus L Cone
Chairman, Graduate Committee

Approved for the Major Department

4-18-97
Date

Head, Major Department

Approved for the College of Graduate Studies

5/8/97
Date

Graduate Dean

STATEMENT OF PERMISSION TO USE

In presenting this thesis in partial fulfillment of the requirements for a doctoral degree at Montana State University, I agree that the library shall make it available to borrowers under rules of the Library. I further agree that copying of this thesis is allowable only for scholarly purposes, consistent with "fair use" as prescribed in the U. S. Copyright Law. Requests for extensive copying or reproduction of this thesis should be referred to University Microfilms International, 300 North Zeeb Road, Ann Arbor, Michigan 48106, to whom I have granted "the exclusive right to reproduce and distribute my dissertation for sale in and from microform or electronic format, along with the right to reproduce and distribute my abstract in any format in whole or in part."

Signature

Date 4/18/1997

ACKNOWLEDGMENTS

The author is grateful to all those who gave their time, expertise and wise counsel to him during his graduate career. First and foremost, he wants to thank his advisor, Professor Rufus L. Cone; only with his countless advice and assistance, could this thesis become possible.

The author also wishes to acknowledge the technical assistance from Norman Williams and Erik Andersen, and for the useful discussion and assistance from his lab colleagues: Greg White, Charles Thiel, Todd Harris, Gregory Reinemer, Dr. Nicholas Strickland, Dr. Flurin Koenz, and Sebastien Ermeneux, special thanks to Dr. Yongchen Sun and Dr. Randy W. Equall for their relentless tutoring in running the experiments and analyzing the data.

The author is indebted to Dr. R. M. Macfarlane and Dr. M. J. M. Leask for their stimulating discussion and productive collaboration.

The author would like to thank Scientific Materials Corporation for providing high quality crystal samples.

Finally, the author would like to express his gratitude to his wife Bingbing Chen and his family for all of their love and encouragement over the years.

TABLE OF CONTENTS

TABLE OF CONTENTS — Continued

TABLE OF CONTENTS — Continued

Page

LIST OF TABLES

Page

LIST OF TABLES — Continued

Page

LIST OF FIGURES

Page

LIST OF FIGURES — Continued

Page

LIST OF FIGURES — Continued

Page

LIST OF FIGURES — Continued

Page

LIST OF FIGURES — Continued

Page

LIST OF FIGURES — Continued

Page

LIST OF FIGURES — Continued

Page

ABSTRACT

Spectral and structural properties of rare earth doped crystals have been investigated with white light absorption, fluorescence, fluorescence excitation, optically-detected nuclear-magnetic-resonance (ODNMR), photon echo and optical nutation.

Conventional spectroscopy was used to study Pr^{3+}, Nd^{3+}, Sm^{3+}, Eu^{3+}, Ho^{3+}, Er^{3+} and Tm^{3+} doped $Y_3Al_5O_{12}$ crystals. Besides the intrinsic site spectroscopy, systematic studies on dopant ions in defect sites were carried out. There were generally 3-6 defect lines within $\pm$ 60 cm^{-1} of the intrinsic line. Quantitative optical absorption measurements showed that 4-7% of the dopants appeared in defect sites for the Eu^{3+}, Ho^{3+}, Er^{3+} and Tm^{3+} doped $Y_3Al_5O_{12}$ crystals and 15-21% of the dopants appeared in defect sites for the Pr^{3+} and Nd^{3+} doped $Y_3Al_5O_{12}$ crystals. These defects were attributed to the 1% of excess Y^{3+} substituting at Al^{3+} *a* sites (C_{3i} symmetry) with a random distribution for Eu^{3+}, Ho^{3+}, Er^{3+} and Tm^{3+} ions whose radii were close to Y^{3+} and a preferred distribution for Pr^{3+} and Nd^{3+} ions whose radii were much larger than Y^{3+}.

Angle dependent ODNMR was used to determine the nuclear principal axis orientations of Pr^{3+} ions in the intrinsic and defect sites of Pr^{3+}:$Y_3Al_5O_{12}$. The intrinsic site has D_2 symmetry which constrains the orientation of Pr^{3+} nuclear principal axes to specific directions. These directions were verified through ODNMR measurements. Using angle dependent ODNMR, one defect site was found to have C_1 symmetry which is attributed to Y^{3+} substituting at Al^{3+} *a* sites.

Optical dephasing was studied for Tm^{3+}:$Y_2Si_2O_7$ as a function of temperature and laser excitation intensity via photon echo measurements. Temperature dependence of the optical dephasing was attributed to phonon coupling between the ground states $^3H_6(1)$ and $^3H_6(2)$ which were 6 cm^{-1} apart. Instantaneous spectral diffusion is another dephasing mechanism in this crystal. Using photon echoes, a homogeneous linewidth of 14 kHz was measured at 1.24 K for the $^3H_6(1) \rightarrow {}^3H_4(1)$ transition. The relatively broad inhomogeneous linewidth of 100 GHz gave an inhomogeneous-to-homogeneous linewidth ratio of 7×10^6. This large ratio combined with a transition wavelength suitable for GaAlAs semiconductor lasers and the absence of hyperfine structure hole burning make this material an interesting candidate for time-domain signal processing and transient optically-addressed data storage.

Coherent transients were also studied for Tm^{3+}:$Y_3Al_5O_{12}$ via optical nutation measurements. Beats were observed due to the presence of several Rabi frequencies from the crystallographically-equivalent but orientationally-inequivalent crystal sites. Using symmetry considerations, we found for the first time that when the light electric field was along one of two special directions (111) and (001), the nutation had a single Rabi frequency. A general procedure for obtaining single Rabi frequency nutation ("single-dipole") in arbitrary crystals is presented.

CHAPTER 1

INTRODUCTION

Defect sites in crystals doped with trivalent rare earth ions have been studied extensively, but there are still many interesting and challenging questions waiting to be answered. This thesis studies the defects in rare earth ion doped $Y_3Al_5O_{12}$ crystals. In particular, the defects in Pr^{3+}, Nd^{3+}, Sm^{3+}, Eu^{3+}, Ho^{3+}, Er^{3+}, and Tm^{3+} doped $Y_3Al_5O_{12}$ crystals were systematically studied using conventional spectroscopic methods including white light absorption, fluorescence, and fluorescence excitation. Energy levels of the rare earth ion in defect sites were measured, and the intensities of the transitions were used to determine the defect site concentration. The local structure of one defect site in Pr^{3+} doped $Y_3Al_5O_{12}$ crystal was studied using nonlinear spectroscopic methods including optically detected nuclear magnetic resonance (ODNMR) and Raman heterodyne detection of NMR.

A better understanding of the defects is very helpful in improving laser efficiency, laser longevity and crystal growth techniques. Because the $Y_3Al_5O_{12}$ crystal has a relatively complex structure compared to other crystals, the techniques used in this thesis can also be applied to other crystals for defect or structural studies.

There are several excellent books on rare earth ion spectroscopy.[1-3] Readers are referred to these books for overviews. This chapter introduces several spectroscopic and structural topics: homogeneous broadening, inhomogeneous broadening, satellite lines in the spectra, crystal structure and selection rules for R^{3+} doped $Y_3Al_5O_{12}$, crystal growth and sample preparation, defects in R^{3+} doped $Y_3Al_5O_{12}$, and mechanisms for defect formation. These topics will provide the background for further discussion in the following chapters.

Homogeneous Broadening

Spectral lines of the rare earth ions in crystals are normally broadened by two major classes of mechanisms i.e. homogeneous broadening and inhomogeneous broadening. Homogeneous broadening arises from dynamic perturbations caused by lattice phonon coupling, nuclear or electron spin couplings and population decay. This broadening is experienced equally by all the ions but can be different for different energy levels. Within one J manifold, the splittings between different crystal field components are less than average phonon frequencies. When the upper crystal field components are excited, they nonradiatively decay to the lowest crystal field component through phonon coupling which increases their homogeneous linewidth. On the other hand, since the separation between J manifolds is often larger than the maximum phonon frequency at liquid helium temperatures, multiphonon emission is normally required to relax the lowest crystal field component. Therefore, the lowest component of a J-manifold has

smaller homogeneous broadening (kHz-MHz scale) than the upper crystal field components.

The lowest crystal field component is generally chosen for detailed spectroscopic studies for several reasons. Small broadening makes the satellite lines easily resolved around this lowest crystal field component. With little non-radiative decay, it is possible to detect fluorescence, apply optical pumping and use advanced nonlinear spectroscopic techniques. A long lifetime is also desirable for optical memory applications by allowing time for recording and retrieving optical data pulses.

Changes in temperature can dramatically change the homogeneous broadening by changing the phonon population. In order to reduce the homogeneous broadening, most of our experiments were done with the samples immersed in superfluid liquid helium pumped to a temperature of 1.4 K unless otherwise specified.

Inhomogeneous Broadening

No crystal is perfect; strains, impurities, and defects are common. For example, $Y_3Al_5O_{12}$ crystals are grown from the melt at high temperature. Compositions can change on a microscopic scale during growth introducing strains. When the crystals are cooled, static lattice strains are also introduced. Impurities may come from the raw oxide starting materials and from the melt crucible. Defects such as striae may appear when there are small temperature variations during the growth. Growth departing from the stoichiometric composition can also form local defects.

All of these perturbations will generate local environments with slightly different crystal fields. When the rare earth ions are doped into these various environments, the resulting distribution of transition frequencies for all the ions will have a typically Gaussian form; this is called inhomogeneous broadening. When the dopant concentration is high, the dopant ions themselves can also cause extra perturbations which will in turn inhomogeneously broaden the lines.

Inhomogeneous broadening usually completely dominates the linewidths of transitions of the lowest level in a given J manifold at temperatures below ~50 K. The inhomogeneous linewidth obscures other important spectroscopic parameters such as the homogeneous linewidth and hyperfine or superhyperfine splittings that are on the order of kHz - MHz. Advanced techniques are needed to extract these important parameters.

Satellite Lines in the Spectra

Impurities not only cause inhomogeneous broadening but may also give rise to additional lines in the absorption and emission spectra. This phenomenon was attributed to the formation of different impurity clusters, as a result of which a distribution of R^{3+} ions among different sites with different crystal fields occurred. This subject has been studied by many researchers. A recent paper was published by John Wright's group.[4] More detailed references will be provided for specific R^{3+}:$Y_3Al_5O_{12}$ crystals.

Using the conventional spectroscopic techniques described in Chapter 2, one can separate the spectra of R^{3+} ions with inequivalent crystallographic environments (activator centers) and consequently analyze the mechanism of cluster formation in

connection with the nature of the valence and size of the impurity ions and the specific crystal structure. This phenomenon is closely related to the laser performance of rare earth doped $Y_3Al_5O_{12}$ crystals. This thesis will classify and study $Y_3Al_5O_{12}$ defects with a variety of spectroscopic techniques.

Crystal Structure and Selection Rules for R^{3+} Doped $Y_3Al_5O_{12}$

The $Y_3Al_5O_{12}$ garnet crystal structure is shown in Figure 1. The ideal structure of the simple rare-earth garnets $A_3B_2C_3O_{12}$ is cubic O^{10}_h (Ia3d), and the unit cell contains eight molecules. In these garnets all the cations are trivalent; the *A* ions are rare-earth elements such as Pr^{3+}, Nd^{3+}, or group-III elements such as Y^{3+} located at dodecahedral *c* sites (with local D_2 symmetry), while the *B* and *C* ions are group-III elements such as Al^{3+} or Ga^{3+}. The *B* ions are placed in trigonally distorted octahedral *a* sites (C_{3i} symmetry), while the *C* ions occupy tetrahedral *d* sites (S_4 symmetry). Crystallographic data for $Y_3Al_5O_{12}$ is shown in Table 1.

The R^{3+} ions that substitute for Y^{3+} ions on the dodecahedral sites experience a crystal field of D_2 symmetry. There are six magnetically-inequivalent orientations of these sites in the crystal, as shown in Figure 2.[6] The local x, $\acute{y}$, and z axes of site 1 are oriented along the (110), $(1\,\bar{1}\,0)$ and (001) directions of the crystal with the z axis coinciding with the (001) axis by convention. The local axes of other sites can be obtained by applying the cubic symmetry operation.

Table 1. Crystallographic data for $Y_3Al_5O_{12}$. Cubic Ia3d, #230, Z = 8. X-ray data: a = 12.000 angstrom, x = -0.0306, y = 0.0512, z = 0.1500.[5]

Ion	Position	Symmetry	X	Y	Z
Y	24©	D_2	0	1/4	1/8
Al_1	16(*a*)	C_{3i}	0	0	0
Al_2	24(*d*)	S_4	3/8	0	1/4
O	96(*h*)	C_1	x	y	z

The D_2 point group contains four one-dimensional irreducible representations, Γ_1, Γ_2, Γ_3, and Γ_4. For R^{3+} ions with an even number of *f* electrons such as Pr^{3+} with a ($4f^2$) configuration, each $^{2S+1}L_J$ manifold is split into 2J+1 nondegenerate components, often called Stark levels. Table 2 gives the irreducible group representations for each value of J up to 6. From the multiplication tables given by Koster et al.,[7] the selection rules for electric-dipole and magnetic-dipole transitions can be determined and are summarized in Table 3. When the initial and final states have the same representation, the electric-dipole and magnetic-dipole transitions between them are forbidden.

Table 2. Full rotation compatibility table for the D_2 group[7]

J	Γ_1	Γ_2	Γ_3	Γ_4
0	1	0	0	0
1	0	1	1	1
2	2	1	1	1
3	1	2	2	2
4	3	2	2	2
5	2	3	3	3
6	4	3	3	3

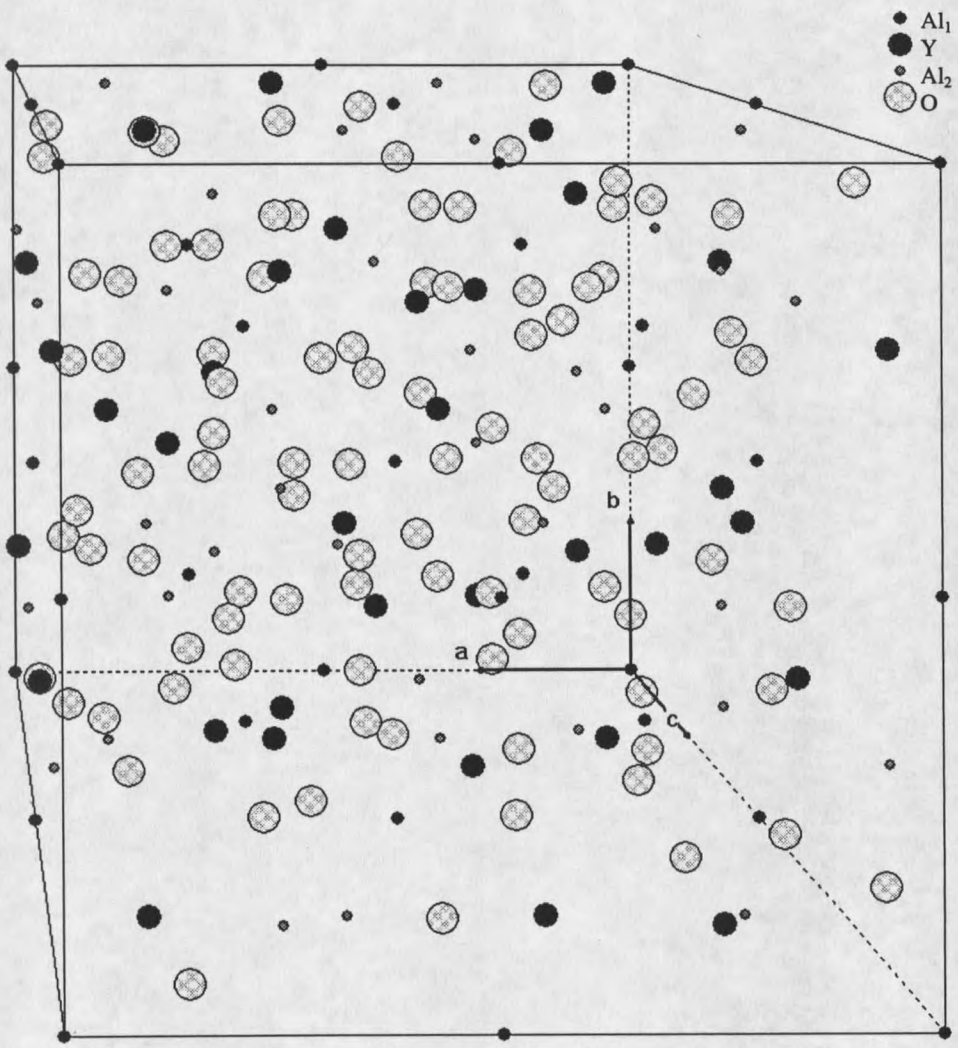

Figure 1. The very complex $Y_3Al_5O_{12}$ crystal structure. Al_1 represents the Al^{3+} ion in an *a* site and Al_2 represents the Al^{3+} ion in a *d* site. There are eight molecules and a total of 160 ions per unit cell.

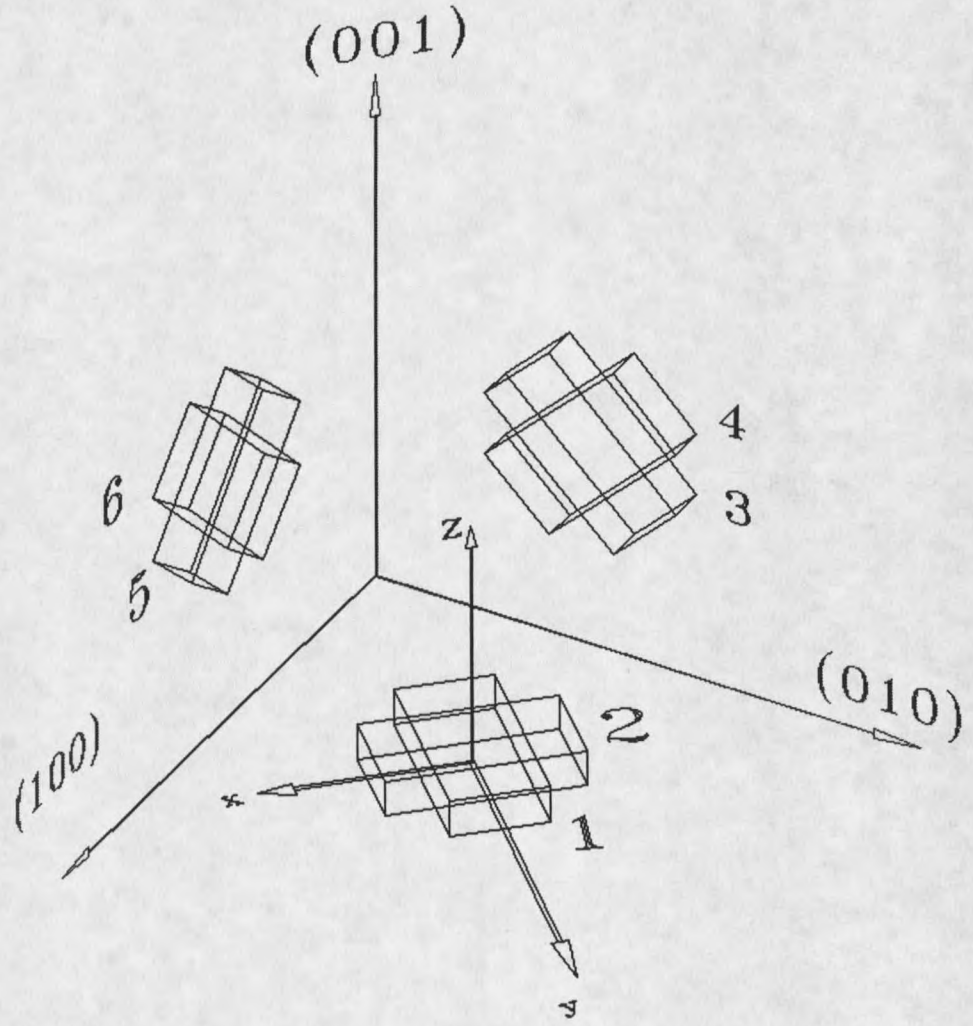

Figure 2. Orientation in the crystal lattice of the six orientationally-inequivalent sites of the Y^{3+} ion in the unit cell of yttrium aluminum garnet.[6] The rectangular boxes represent the local D_2 symmetries where each axis direction is different, and x, y and z are the local axes for site 1 of 6 sites.

Table 3. Electric-dipole and magnetic-dipole selection rules for D_2 symmetry. The Γ_i's are the representations of the initial & final states. E denotes electric-dipole; M, magnetic-dipole. The indices x, y, and z refer to the local site symmetry axes.

	Γ_1	Γ_2	Γ_3	Γ_4
Γ_1	-	E_y, M_y	E_z, M_z	E_x, M_x
Γ_2	E_y, M_y	-	E_x, M_x	E_z, M_z
Γ_3	E_z, M_z	E_x, M_x	-	E_y, M_y
Γ_4	E_x, M_x	E_z, M_z	E_y, M_y	-

For R^{3+} ions with an odd number of *f* electrons, such as Nd^{3+} ($4f^1$), each $^{2S+1}L_J$ manifold is split into (2J+1)/2 doubly-degenerate components. For an arbitrarily oriented crystal there are no restrictions by the selection rules for electric dipole transitions; hence, the crystal field levels of excited states can all be directly obtained from the absorption spectra.

Crystal Growth and Sample Preparation

Most of the samples studied in this thesis and their measured concentrations were provided by Scientific Materials Corporation in Bozeman, Montana. Growth of garnet materials has been carried out for more than 35 years and is technologically well advanced. Yttrium aluminum garnet is a congruently melting compound (m.p. 1970 °C). The dopant incorporation into the host crystal is governed by the following expression[8]

$$C_S = kC_L \tag{1.1}$$

where C_S is the dopant concentration in the solid, C_L is the starting melt composition, and k is the distribution of the dopant between the solid and liquid phases. The value of k is

ordinarily less than unity and depends markedly upon the dopant radius and growth condition.[8]

Pure R_2O_3, Y_2O_3, and Al_2O_3 powder is mixed and melted in a crucible to growth R^{3+}:$Y_3Al_5O_{12}$ crystal. The maximum R^{3+} concentration is limited by the ionic radius mismatch between relatively large rare earth ions and smaller aluminum ions. In the extreme end, the rare earth garnet $R_3Al_5O_{12}$ grown from three part R_2O_3 and five part Al_2O_3 mixture is found only for the R^{3+} ions between Gd^{3+} and Lu^{3+}. Ions larger than Gd^{3+} do not form garnets in the simple two oxide system. However, a garnet crystal with low concentration of ions from Ce^{3+} to Sm^{3+} can be formed from the molten phase.

Single crystals used in this study were grown parallel to the (111) direction by the Czochralski technique from yttrium aluminum garnet melts doped with R^{3+} oxide. Normally rods about 5mm in diameter were cut from the boules parallel to the (111) direction. Two end faces were polished to optical quality. Most white light absorption experiments were done along (111). The sides of some rods were polished for fluorescence experiments. Most crystals studied in this thesis have low dopant concentration for high resolution spectroscopy, hence, they are colorless.

Defects in R^{3+} Doped $Y_3Al_5O_{12}$ and Mechanisms for Defect Formation

Doping of garnet crystals with R^{3+} ions is expected to lead to the appearance of a very limited variety of structural centers, according to the site preference of the dopant. Conventionally, one assumes that only the transitions belonging to a single structural center (D_2 site for the R^{3+} doped garnet) exist, but this is not the case in practice. A much

more complex behavior is observed in optical spectra. The multisite structure of R^{3+} ions in garnet crystals is not a completely elucidated problem, and is a major focus of this thesis. The analysis of defect structures requires further attention, due to the structural information that can be obtained, the impact on laser design, and information on the R^{3+} - R^{3+} interaction mechanisms. One objective of this thesis is to develop a better understanding of structural defects, using both conventional spectroscopy and nonlinear spectroscopy.

The ideal garnet has the compound formula $A_3B_2C_3O_{12}$, where *A*, *B*, *C* ions occupy the dodechedral D_2 *c* site, the octahedral C_{3i} *a* site, and the tetrahedral S_4 *d* site, respectively. Lattice parameter measurements using X-ray powder diffraction on rare-earth gallium garnets have shown that the compositions of garnet crystals grown from the melt are different from the compositions of stoichiometric ceramic samples.[9,10] This difference is attributed to an excess (up to several percent as a function of composition) of *A* ions occupying the octahedral sites; the composition can be written as $A_3(B_{1-x}A_x)_2C_3O_{12}$. The value x may vary depending on the synthesis temperature, the composition of the melt, and the type of RE ions. For $Y_3Al_5O_{12}$ crystals grown from the melt at 1970 °C, the estimated formula is $Y_3(Al_{0.985}Y_{0.015})_2Al_3O_{12}$.[9]

Several types of optical spectra for R^{3+}:$A_3B_2C_3O_{12}$ have been investigated by a number of groups:[11-14]

(1) the main spectrum, corresponding to R^{3+} in unperturbed dodecahedral *c* sites,

(2) satellite lines, whose relative intensity does not depend on R^{3+} content, assigned to R^{3+} in *c* sites perturbed by the presence of *A* ions in anomalous *a* sites,

(3) satellite lines, whose relative intensity does depend on dopant concentration, assigned to the near-neighbor pairs of R^{3+} ions in *c* sites,

(4) weak lines assigned to R^{3+} in octahedral *a* sites,

(5) lines arising from the perturbation by anionic impurities such as OH^-.

Spectra of type (1) are usually studied first. Energy levels can be readily determined using the selection rules for D_2 symmetry given in Table 3. This provides the starting point for studying the satellite lines. Spectra of types (2), (3), and (5) originate from R^{3+} ions in perturbed dodecahedral *c* sites. Normally for each type, there are several weak lines surrounding the main line of type (1); these three types have different properties such as fluorescence lifetime and energy transfer rate, and their properties are closely related to the local environment. Spectra of type (4) originate from R^{3+} ions in the C_{3i} site and have selection rules quite different from those in Table 3. Different types of the defect spectra mentioned above may dominate depending on the dopant concentration, dopant radius, and host crystals. Spectrum types (1), (2), and (4) were observed and will be explained in this thesis. More work needs to be done to correlate the spectrum type (5) to OH^- impurity by comparing samples with different OH^- concentrations.

In order to have a quantitative study of the defect lines, we need to consider the distributions of R^{3+} ions and of the defects in the crystal. Substitution of trivalent *A* ions by R^{3+} activators does not require charge compensation, and therefore there is no reason

for an electrostatic-interaction correlation in their distribution in the lattice. Since at low concentration the difference in the ionic radii between an R^{3+} ion and the host cation A normally does not lead to size correlation, the most likely model for R^{3+} distribution in garnets is random uniform occupancy of the available sites. Similar arguments are valid for other structural defects such as anomalous A ions in octahedral sites.[15]

For a random uniform distribution of activators, the probability of occurrence of ensembles formed by a given activator ion with n neighbor activators in a sphere with m sites is given by[16]

$$C_{nm} = \frac{m!}{n!(m-n)!} C^{n+1}(1-C)^{m-n}, \tag{1.2}$$

where C is the concentration of activators. For low C values, the most probable ensembles are pairs, i.e., $n = 1$. From Eq. (1.2), the pair concentration is $C_{1m} = mC^2(1-C)^{m-1}$. For low dopant such as $C = 0.1\%$ the pair concentration is negligible (~ 1ppm).

The probability of occurrence of ensembles formed by a given activator ion with n' neighbor defects in a sphere with m' sites is given by[16]

$$C_{n'm'} = \frac{m'!}{n'!(m'-n')!} C(C')^{n'}(1-C')^{m'-n'}, \tag{1.3}$$

where C' is the concentration of defects. The most probable ensembles are with one defect neighbor, i.e., n'=1, whose concentration is $C_{1m'} = m'CC'(1-C')^{m'-1}$. When C' is a few percent, these clusters make a significant contribution to the defect lines.

The number of sites in the neighboring spheres around different sites and the radii of these spheres for $Y_3Al_5O_{12}$ are given in Table 4.

Table 4. The cationic coordination for Y^{3+} in $Y_3Al_5O_{12}$. *m* represents the number of neighbors in a sphere of radius r.

Ion site	Site sym.	Neighbors	Ion Radius	Sphere I		Sphere II		Sphere III	
			(Å)	*m*	r (Å)	*m*	r (Å)	*m*	r (Å)
Y^{3+} (*c*)	D_2	Y^{3+} (*c*)	1.02	4	3.674	8	5.612	2	6.000
		Al^{3+} (*a*)	0.53	4	3.354	4	5.408	8	6.874
		Al^{3+} (*d*)	0.39	2	3.000	4	3.674	8	5.612
		O^{2-} (*h*)	1.38	4	2.303	4	2.432	4	3.827
Al^{3+} (*a*)	C_{3i}	Y^{3+} (*c*)		6	3.354	6	5.408	6	6.874
		Al^{3+} (*a*)		8	5.196	6	6.000	12	8.485
		Al^{3+} (*d*)		6	3.354	6	5.408	6	6.874
		O^{2-} (*h*)		6	1.937	6	3.750	6	4.261
Al^{3+} (*d*)	S_4	Y^{3+} (*c*)		2	3.000	4	3.674	8	5.612
		Al^{3+} (*a*)		4	3.354	4	5.408	8	6.874
		Al^{3+} (*d*)		4	3.674	8	5.612	2	6.000
		O^{2-} (*h*)		4	1.761	4	3.310	4	3.622
O^{2-} (*h*)	C_1	Y^{3+} (*c*)		1	2.303	1	2.432	1	3.827
		Al^{3+} (*a*)		1	1.937	1	3.750	1	4.261
		Al^{3+} (*d*)		1	1.761	1	3.310	1	3.622

References for Chapter 1

1. B. G. Wybourne, *Spectroscopic Properties of Rare Earths* (Interscience, New York, 1965).

2. G. H. Dieke, *Spectra and Energy Levels of Rare Earth Ions in Crystals* (Wiley-Interscience, New York, 1968).

3. S. Hufner, *Optical Spectra of Transparent Rare-Earth Compounds* (Academic Press, New York, 1978).

4. L. J. Knott, N. J. Cockroft, and J. C. Wright, Phys. Rev. B, **51**, 5649 (1995).

5. F. Euler and J. A. Bruce, Acta Cryst. **19**, 971 (1965).

6. J. F. Dillon, Jr., and L. R. Walker, Phys. Rev. **124**, 1401 (1961).

7. G. F. Koster, J. O. Dimmock, R. G. Wheeler, and H. Statz, *Properties of the 32 Point Groups* (M.I.T. Press, Cambridge, 1963).

8. J. A. Burton, R. C. Prim, and W. P. Slichter, J. Chem. Phys. **21**, 1987 (1953).

9. S. Geller, G. P. Espinosa, L. D. Fullmer, and P. B. Crandall, Mater. Res. Bull. **7**, 1219 (1972).

10. C. D. Brandle and L. R. Barns, J. Cryst. Growth **26**, 169 (1974).

11. Yu. K. Voronko and A. A. Sobol, Phys. Status Solidi A **27**, 657 (1975).

12. M. Kh. Ashurov, Yu. K. Voronko, A. A. Sobol, and M. I. Timoshechkin, Phys. Status Solidi A **42**, 101 (1977).

13. D. P. Devor and L. G. Deshazer, Opt. Commun. **46**, 97 (1983).

14. D. P. Devor, L. G. DeShazer, and R. C. Pastor, IEEE J. Quantum Electron. **25**, 1863 (1989).

15. V. Lupei, A. Lupei, C. Tiseanu, S. Georgescu, C. Stoicescu, and P. M. Nanau, Phys. Rev. B **51**, 8 (1995).

16. V. V. Osiko, Yu. K. Voronko, and A. A. Sobol, *Crystals* (Springer-Verlag, Berlin, 1984), Vol. **10**, P. 37.

CHAPTER 2

CONVENTIONAL SPECTROSCOPY

White Light Absorption

When investigating a new rare earth doped crystal, white light absorption experiments were first used to measure the energy levels of the dopant ions. The standard experimental setup has been described previously.[1] Further details need to be mentioned in the context of infrared spectroscopy. When using the SPEX 14018 monochrometer in the infrared region, the second order response of the grating should be considered. When measuring white light absorption for Tm^{3+} ($^3H_4$ at ~12500cm^{-1}) or Nd^{3+} ($^4F_{3/2}$ at ~11500cm^{-1}) etc., a long pass filter such as CORNING® 3-67 was used in the collimated beam to block out the blue spectral region and thus to avoid the second order response. The same was true when the uranium hollow cathode lamp was used for calibration in the IR region. The color filter was inserted in the collimated portion of the beam rather than the converging or diverging portions of the beam. This arrangement not only avoided realignment of the system, but also minimized the aberrations introduced by the thickness, tilt, and lack of surface parallelism of the color filter plate.

When working in the near IR region, the Hamamatsu R928 photomultiplier (PMT) and cooled RCA 31034 PMT were chosen since they had better gains than the EMI model 9558QB PMT.

Fluorescence

Fluorescence experiments were used to measure the excited state lifetime and the ground state splittings. The experimental setup for pulsed fluorescence and laser excitation spectroscopy is shown in Figure 3. The pulsed lasers were nitrogen-laser-pumped pulsed dye lasers. The cw dye lasers were Coherent model 599-21 and 899-21. The pulsed laser was focused onto the sample using a 25 cm lens and the cw laser was focused with a 33 cm lens. Fluorescence was collected at 90 degrees relative to the laser beam with a 7.5 cm lens. After the lens, a Dove prism was used to rotate the horizontal fluorescence image to vertical orientation so that more light was imaged onto the vertical entrance slit of the SPEX.

For cw fluorescence, the data acquisition was identical to that of white light absorption. For pulsed fluorescence, there were two methods for collecting data. The first used photon counting. In this case, the output of the PMT was passed through a preamplifier and discriminator and then converted to TTL pulses. The pulses were counted by a GPIB controlled Fluke 1953A counter/timer. When the fluorescence light is too intense, the pulses pile up and are too close to be separated, resulting in a loss of counts. This caused the center of strong fluorescence lines to saturate and have a dip. We could either choose a suitable SPEX slit size or adjust the laser power to avoid saturation.

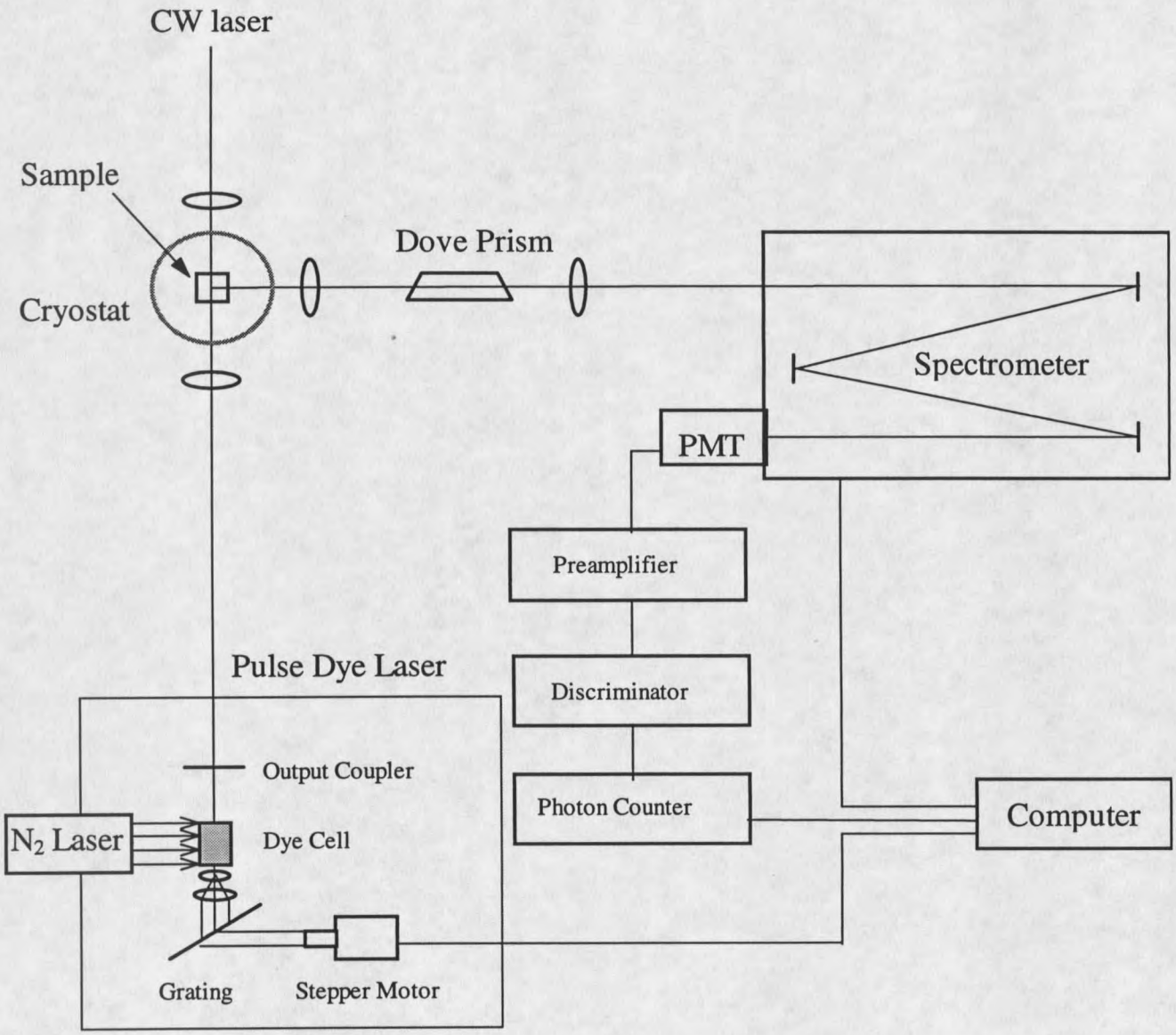

Figure 3. Experimental apparatus for fluorescence and laser excitation.

The second detection method used the GPIB interfaced Tektronix TDS620A digitizing oscilloscope as a sophisticated boxcar. The pulsed fluorescence was collected and averaged by the digitizer. The decay curve was then sent to the computer to be integrated over time. This analog detection does not have the pulse pileup problem of photon counting. On the other hand, the photon counting has higher sensitivity than using the TDS620A digitizer. To avoid internal sample reabsorption that could distort the fluorescence signal and lifetime (T_1), the excitation laser beam was steered as close as possible to the crystal surface.

When measuring fluorescence lifetimes (T_1) with the cw laser, two 80 MHz acousto-optic (A/O) modulators were used in series to generate laser pulses. The laser pulse duration was adjusted to get a suitable transient response for the fluorescence signal. The fluorescence signal was averaged with a Tektronix TDS620A digitizing oscilloscope. When the fluorescence signal was too weak, the SPEX was not used and the PMT was placed against the window of the cryostat. Great care was taken to avoid or reduce the laser scattering. Well polished crystal surfaces were important in this respect. A color filter was added to block the laser scattering when the fluorescence could be separated spectrally from the laser. When fluorescence from different energy levels occurred simultaneously, several color filters were used to isolate signals by selecting the desired spectral regions.

The laser wavelength was measured with a homemade wavemeter with high accuracy (± 50MHz), and it could be used as an excellent calibration source for the SPEX monochrometer.

Fluorescence Excitation

Fluorescence excitation was performed by monitoring the fluorescence while scanning the excitation frequency of the laser. This gives better sensitivity than the white light absorption, and could easily detect the defect lines which were buried in the noise of an absorption spectrum.

In addition to detecting weak absorption, fluorescence excitation also was used for site selective identification of absorbing transitions. When there were several sites, the fluorescence from a particular site was monitored with the SPEX while the laser frequency was scanned over the whole spectral region, i.e. covering several different J multiplets. When the laser was resonant with the transitions associated with the specific site, fluorescence was recorded. Using this method, energy levels from each site could be separated from those from the other sites. This is called site-selective fluorescence excitation.

When there was energy transfer among the sites, time resolved fluorescence excitation was applied to investigate the time dependence of energy transfer and the energy transfer path. As the SPEX spectrometer was scanned through the spectral region of interest, a fluorescence decay curve corresponding to each wavelength was averaged with the TDS 620A and sent to the computer. A 3-D spectrum was constructed from the fluorescence curves. The three axes were fluorescence intensity, wavelength, and time respectively.

When using the homemade N_2 pumped dye laser system, there were two methods for tuning the laser wavelength. The first one shown in Figure 3 used a stepper motor to adjust the horizontal angle of a grating relative to the cavity. It has a large tuning range of several hundred wavenumbers and a bandwidth of 0.5-0.7 cm^{-1}. The second method used a pressure scan; N_2 gas filled the chamber containing the grating and etalon. By adjusting the N_2 gas pressure, the laser wavelength could be tuned with high resolution. The bandwidth was ~ 0.1 cm^{-1}. The tuning range for each grating angle was only several tens of wavenumbers.

For the cw lasers the tuning is done manually. Directly coupled tuning by a stepper motor is mechanically too rough for the Coherent 599 and 899 lasers. A tuning system needs to be designed for cw lasers.

Experimental Results for $Pr^{3+}:Y_3Al_5O_{12}$

Introduction

The optical spectroscopy of $Pr^{3+}:Y_3Al_5O_{12}$ has been studied by various groups.[2-7] A thorough study of energy levels of this crystal was provided by Gruber et al.[8]

$Pr^{3+}:Y_3Al_5O_{12}$ crystals exhibit interesting luminescence properties. Room-temperature emission of Pr^{3+} ions can originate from three states: $^3P_0$, $^3P_1$ and $^1D_2$. Laser action at $\lambda = 690$ nm has been observed on the $^3P_0 \rightarrow {}^3F_6$ transition.[9] Multi-photon processes such as two step excitation[10,11] have also attracted a lot of attention for potential blue and UV lasers. A detailed understanding of the physics of this system is essential to further improvement of its lasing properties.

The $^3H_4 \leftrightarrow {}^1D_2$ transition at 609.6 nm is very convenient for access with a dye laser using Rhodamine 6G dye. As will be presented in Chapter 3, many advanced techniques were applied to this transition to study the hyperfine and coherent phenomena.

This section deals with the spectroscopic investigation of the microscopic disorder in $Pr^{3+}:Y_3Al_5O_{12}$ crystals. In $Y_3Al_5O_{12}$ the R^{3+} impurity substitutes predominantly for Y^{3+} ions in dodecahedral sites; the degree of lattice perturbation due to the substitution is related to the difference between the ionic radii of the two ions. Since Pr^{3+} has a relatively large ionic radius, we expect that the crystal-field distortion due to the presence of a Pr^{3+} neighbor is larger than that produced by Ho^{3+}, Er^{3+} or Tm^{3+} in the $Y_3Al_5O_{12}$ lattice; thus, this system was chosen to study defect sites.

Recently, the complex structure of the absorption and emission spectra of Pr-doped garnet crystals $Y_3Al_5O_{12}$, $Gd_3Ga_5O_{12}$, and $Y_3Ga_5O_{12}$ has been investigated by Antic-Fidancev et al.[6,12-14] They concentrated on analyzing the fluorescence from different ion sites after selective excitation of the $^1D_2$ and $^3P_0$ states. They showed that at least three different sites were responsible for the observed emission. Malinowski et al.[15] also studied the inhomogeneity of this crystal using time-resolved spectroscopy.

In this section, a detailed quantitative study of the absorption, fluorescence, and excitation spectra will be presented.

Results

A 0.018% Pr^{3+}:$Y_3Al_5O_{12}$ (1.04 mm) crystal was provided by Dr. Roger M. Macfarlane (IBM Almaden Research Center). The concentration was determined by electron beam microprobe analysis. A plasma mass spectroscopy analysis of material from the same boule gave 0.021%.

White light absorption spectra for $^1D_2$, $^3P_0$, $^3P_1$, $^3P_2$, and $^1I_6$ were recorded at 1.4K. The absorption spectrum in Figure 4 shows two peaks at 16400 cm^{-1} and 16410 cm^{-1}. These are transitions from the ground state to the lowest two Stark levels of the $^1D_2$ multiplet, denoted $^1D_2(1)$ and $^1D_2(2)$. The linewidth of $^1D_2(1)$ is 1.3 cm^{-1} and its absorption peak coefficient is 4.3cm^{-1}. There are several small satellite peaks around these two main peaks which come from Pr^{3+} ions in several inequivalent sites perturbed from the ideal D_2 site. These defect peaks have about the same linewidth as the intrinsic peak does. The peak at 16381.0 cm^{-1} is a 'hot' peak i.e. $^3H_4(2) \leftrightarrow {}^1D_2(1)$ transition, where

$^3H_4(2)$ is a thermally occupied state near the ground state $^3H_4(1)$. Since the $^1D_2(1)$ and $^1D_2(2)$ peaks for the defects overlapped in the absorption spectrum, fluorescence excitation was applied to separate the $^1D_2(1)$ peaks from the $^1D_2(2)$ peaks.

The percentage of Pr^{3+} in defect sites can be estimated by comparing absorption coefficients of the defect lines and the intrinsic line belonging to the same transition. The absorption intensities of the unsaturated $^1D_2$ (1) peak of the intrinsic site and defect sites were used to determined the defect site concentrations. Based on the assumption that the oscillator strength is independent of the rare earth site, we estimate the percentage of Pr^{3+} in defect sites to be 15%. Because the site distortion tends to introduce level mixing, which in turn might change the oscillator strength, the 15% should be considered a rough estimate of the defect concentration.

The same defect features can be seen in absorption transitions to the lowest levels of $^3P_0$ and $^3P_1$ as shown in Figure 5 and Figure 6. The intrinsic peaks are saturated so their tops are not shown. The peak at 20512.2 cm^{-1} is a hot peak of the intrinsic site. To verify that remaining satellite lines are from independent defect sites, we measured separate fluorescence spectra with the laser frequency tuned to each of the satellite lines. Since there is only one level in the $^3P_0$ manifold, each satellite line represents a defect site. Some excitation and fluorescence spectra are shown for this manifold in Figure 7. The bottom trace is an excitation spectrum monitoring all fluorescence signals and scanning the laser frequency through the $^3P_0$ region. It mimics the absorption spectrum. The site selective fluorescence spectra were obtained by pumping the $^3P_0$ level for each defect site.

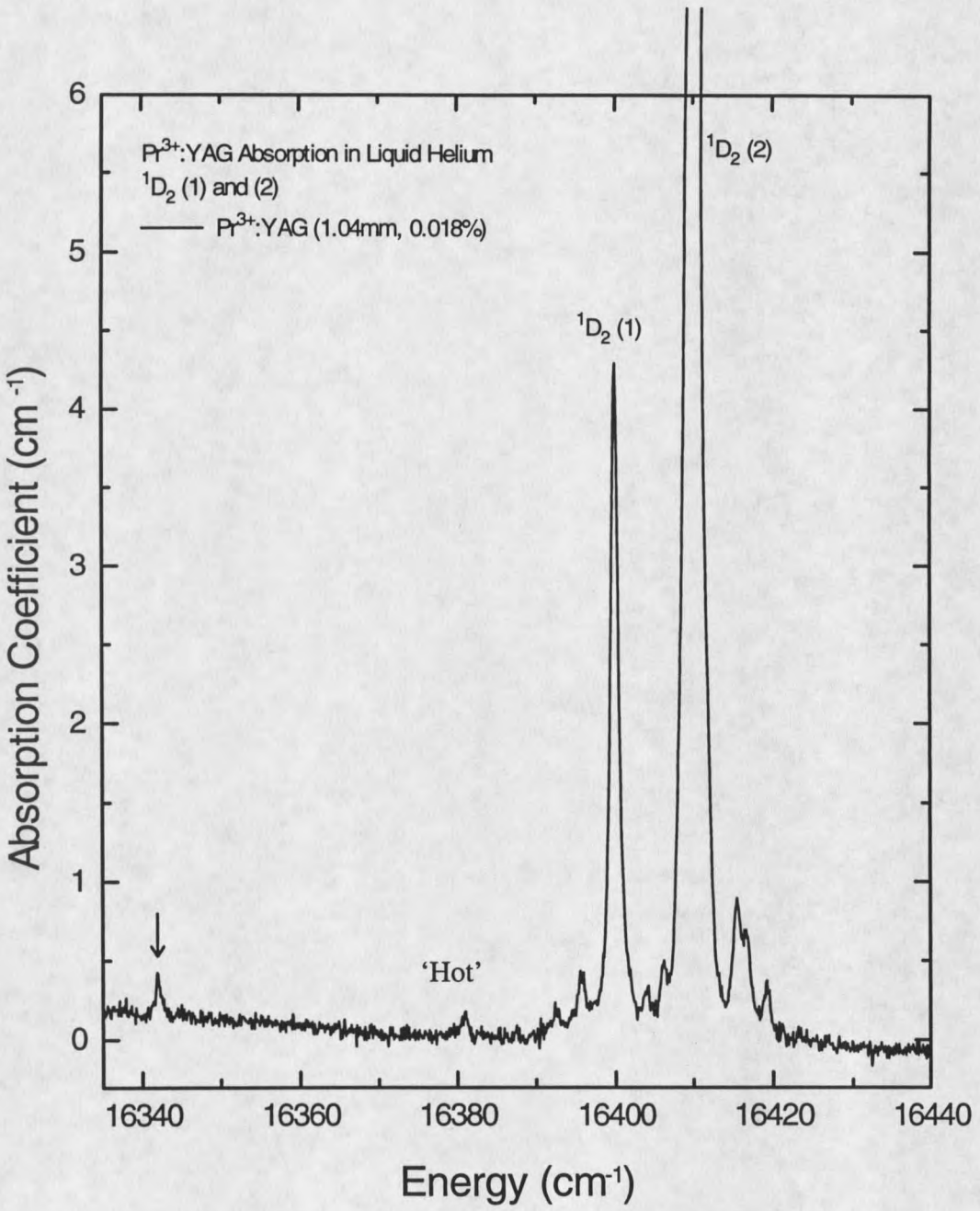

Figure 4. Helium temperature (1.4 K) white light absorption spectrum for $^3H_4(1) \rightarrow {}^1D_2(1)$ and $^3H_4(1) \rightarrow {}^1D_2(2)$ transitions of the 0.018% Pr^{3+}:$Y_3Al_5O_{12}$ (1.04 mm) crystal. The arrow indicates a defect peak which is used for further study in Chapter 3.

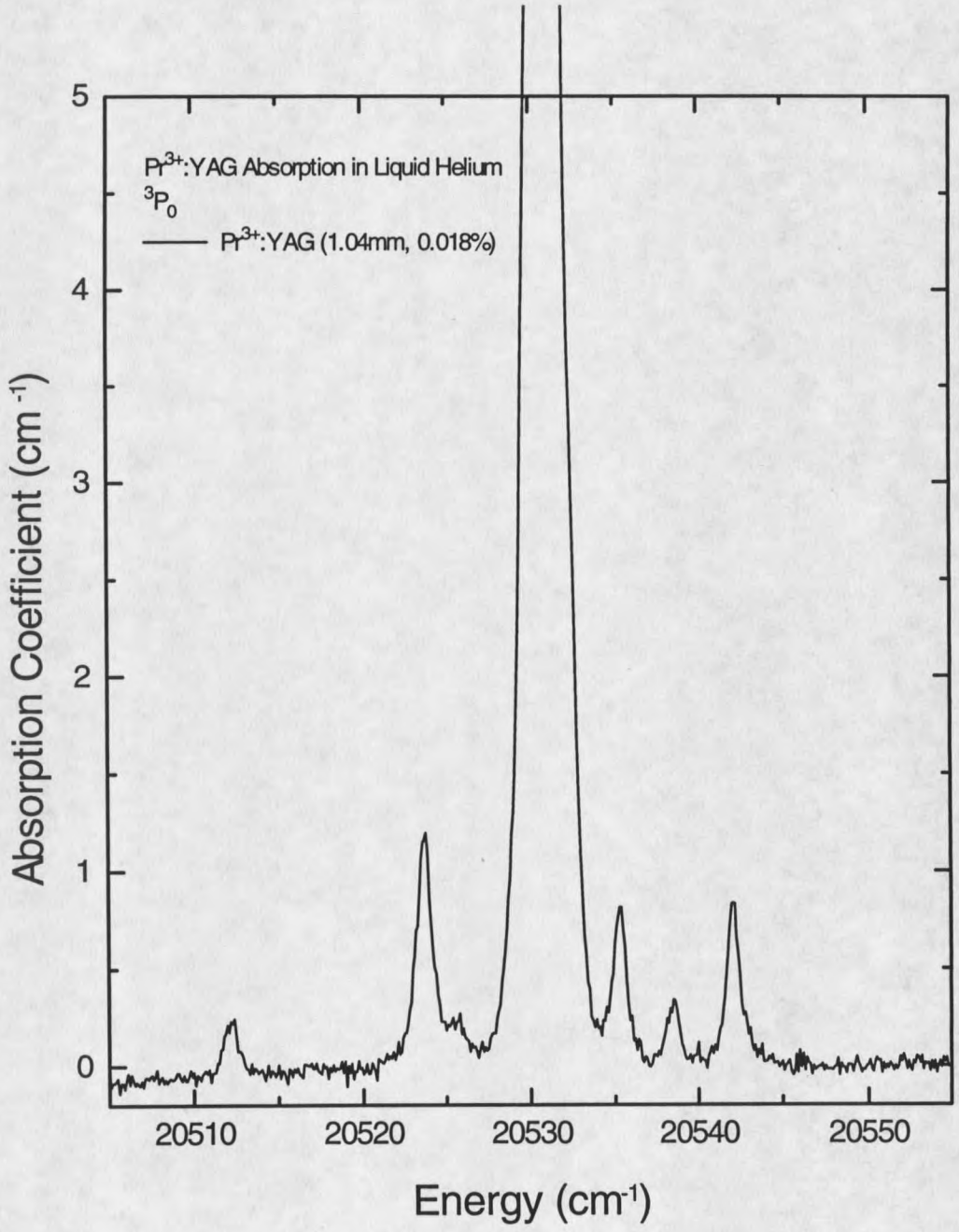

Figure 5. Helium temperature (1.4 K) white light absorption spectrum for $^3H_4(1) \rightarrow {}^3P_0$ transitions of the 0.018% Pr^{3+}:$Y_3Al_5O_{12}$ (1.04 mm) crystal.

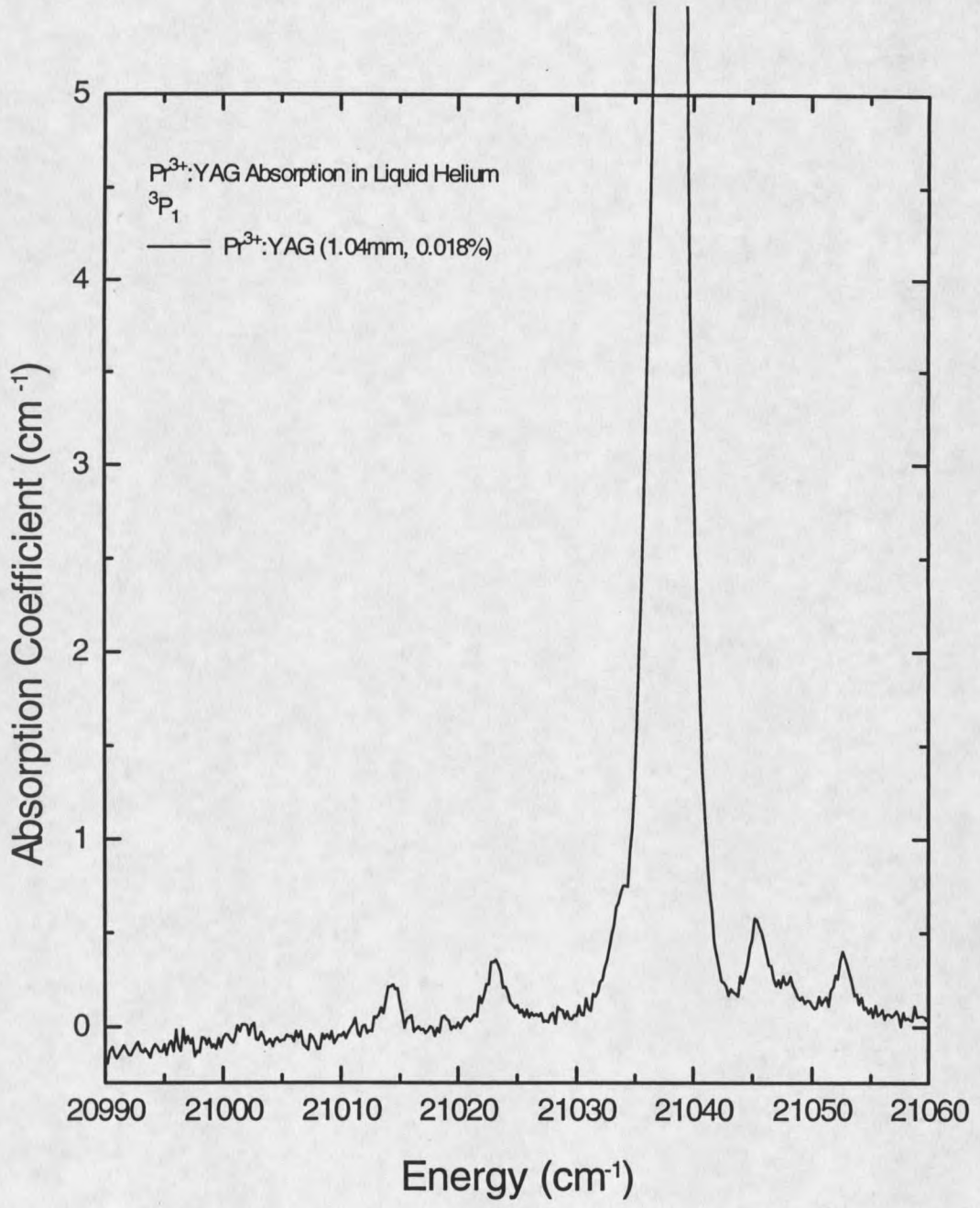

Figure 6. Helium temperature (1.4 K) white light absorption spectrum for $^3H_4(1) \rightarrow {}^3P_1$ transitions of the 0.018% Pr^{3+}:$Y_3Al_5O_{12}$ (1.04 mm) crystal.

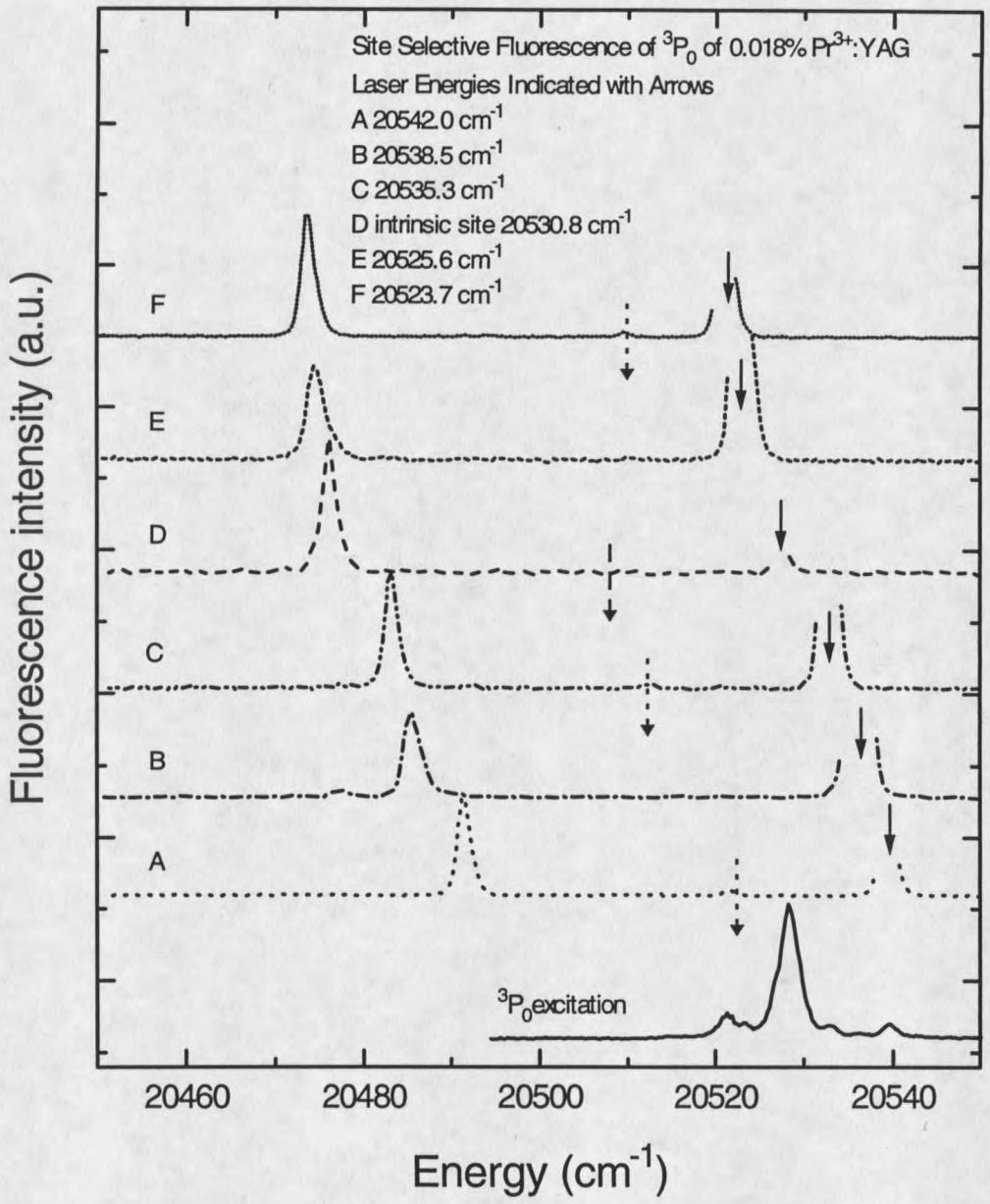

Figure 7. Excitation and site selective fluorescence of $^3P_0$ of the 0.018% Pr^{3+}:$Y_3Al_5O_{12}$ crystal. The portions without data in the fluorescence curves are due to scattered laser saturation. The solid arrows indicate the laser energies used for site selective fluorescence. The forbidden intrinsic site transition from $^3P_0$ to $^3H_4(2)$ is indicated with a dashed arrow. The dotted arrows show the partially allowed $^3P_0 \rightarrow {}^3H_4(2)$ transitions for some defect sites.

The $^3P_0$ level of that single site then fluoresces to $^3H_4(1, 2, 3)$. The transition from $^3P_0$ (Γ_1) to $^3H_4(2)$ (Γ_1) is forbidden by D_2 selection rules since both levels have same symmetry Γ_1. These transitions are partially allowed in defect sites, though, because the ideal site symmetry is perturbed.

From the absorption and fluorescence spectra, energy level diagrams for intrinsic and defect sites of the 0.018% Pr^{3+}:$Y_3Al_5O_{12}$ (1.04 mm) crystal were constructed. The details are listed in Table 5 and Table 6. A schematic diagram of energy levels of the intrinsic site for Pr^{3+}:$Y_3Al_5O_{12}$ is presented in Figure 8.

Since the $^3P_0$ and $^3P_1$ intrinsic lines are saturated, a thinner sample is needed for measuring accurate absorption coefficients and linewidths.

Table 5. Detailed energy level information for intrinsic and defect sites of the 0.018% Pr^{3+}:$Y_3Al_5O_{12}$ (1.04 mm) crystal at 1.4 K. The levels in the same column for defect sites do not necessarily belong to the same site except when in bold type. The number of intrinsic levels is 2J+1 for each manifold.

Level	intrinsic site (cm^{-1})
$^3H_4$	**0**
	18.0
	50.8
	533.0
	576.0
	742.0
$^1D_2$	**16400.0**
	16410.0
	16881.0
	17088.0
	17210.0
$^3P_0$	**20530.8**
$^3P_1$	**21037.7**
	21136.2

Level	defect sites (cm^{-1})					
$^3H_4$	**0**	**0**	**0**	**0**	**0**	**0**
	26.8	**20.8**	**11.5**	**20.4**	**25.6**	**16.8**
	78.2	**49.3**	**47.4**	**52.4**	**39.2**	**52**
$^1D_2$	**16342.2**	**16392.4**	**16395.6**	**16399.6**	**16391.6**	**16406.0**
		16419.4	**16404.4**	**16416.8**	**16415.6**	
$^3P_0$	20525.6	**20535.3**	**20523.7**	20538.5	20542.0	**20530.8**
$^3P_1$	21001.8	21014.2	21023.1	21034.1	21045.4	21052.7

Table 6. Linewidths and absorption coefficients for some transitions to $^1D_2$, $^3P_0$ and $^3P_1$ of intrinsic and defect sites of the 0.018% Pr^{3+}:$Y_3Al_5O_{12}$ (1.04 mm) crystal at 1.4 K.

	Line position (cm-1)	Linewidth (cm-1)	Peak Absorption Coefficient (cm-1)
$^1D_2$	16342.2	0.8	0.29
	16391.6	0.8	0.05
	16392.4	0.9	0.15
	16395.6	1.2	0.27
	16400.0	1.3	4.30
	16404.4	1.0	0.19
	16406.0	0.8	0.21
	16415.6	0.9	0.39
	16416.8	0.7	0.22
	16419.4	0.9	0.27
$^3P_0$	20523.7	1.0	1.16
	20525.6	0.8	0.11
	20535.3	0.8	0.69
	20538.5	0.9	0.33
	20542.0	0.9	0.81
$^3P_1$	21001.8	2.2	0.09
	21014.2	1.9	0.19
	21023.1	2.1	0.33
	21034.1	1.8	0.11
	21045.4	2.1	0.41
	21052.7	1.8	0.32

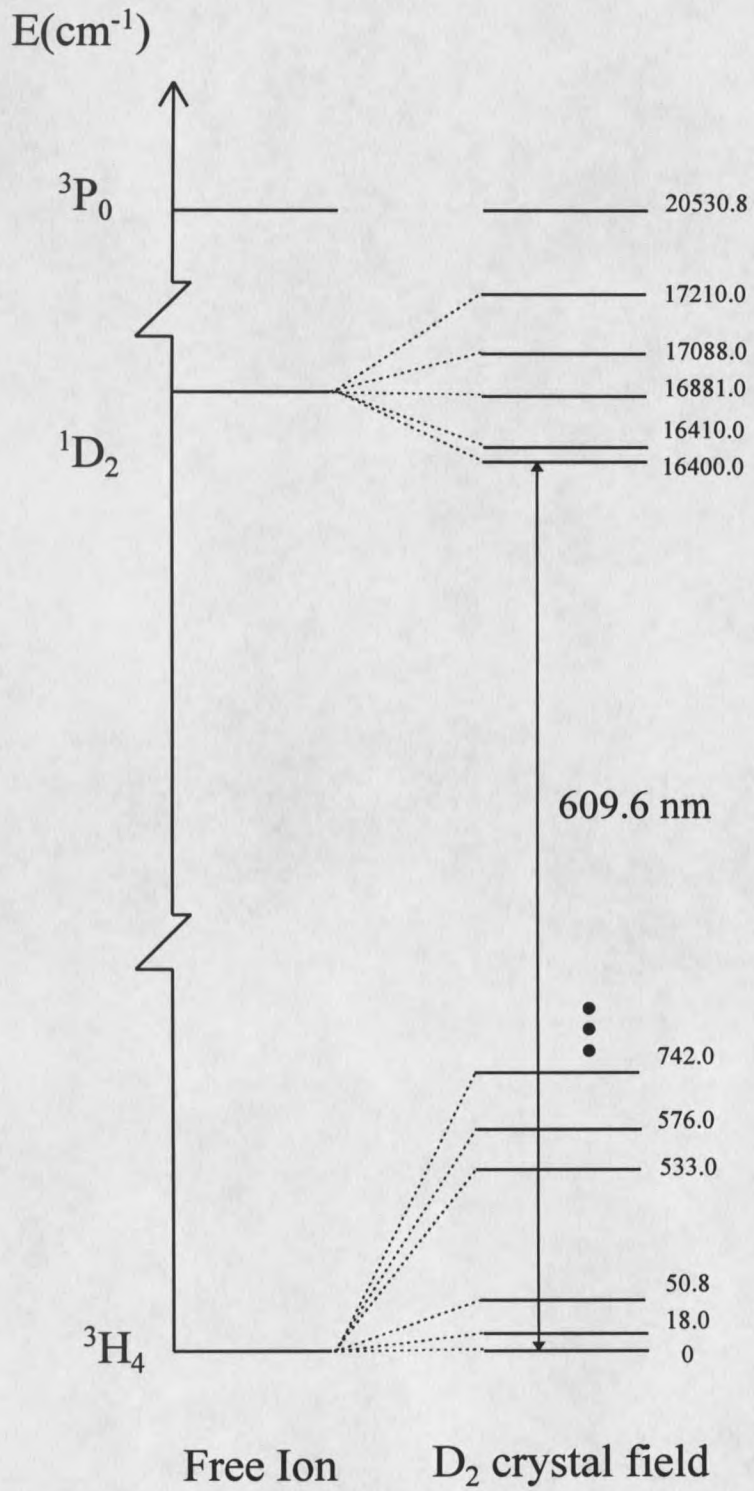

Figure 8. Schematic of energy levels of the intrinsic site for Pr^{3+}:$Y_3Al_5O_{12}$. Since some transitions from $^1D_2$ to $^3H_4$ are forbidden by transition rules, only six out of the nine levels of $^3H_4$ were determined.

Experimental Results for $Nd^{3+}:Y_3Al_5O_{12}$

Introduction

The neodymium $Y_3Al_5O_{12}$ laser is, beyond a doubt, the most popular rare earth doped solid-state laser in existence today. The spectroscopic studies on the intrinsic site and defect sites of $Nd^{3+}:Y_3Al_5O_{12}$ have been extensive.[16-30] These studies concentrated on the laser related properties, such as quantum efficiencies, fluorescence rates, inequivalent crystal field effects, line broadening, lattice-defect interactions, and their temperature dependences. These properties are influenced by defects in the crystal. The defects can affect color center formation, energy transfer, fluorescence quenching, and hence laser performance. In order to improve laser performance, further study of defect structure is desirable. This section will give accurate information about peak intensitites using high-resolution (0.1 cm^{-1}) white light absorption spectroscopy. The minimum step size of the SPEX 14018 monochrometer is 0.02 cm^{-1}. The resolution is about 0.1 cm^{-1} at 19000 cm^{-1} and is wavelength dependent with higher resolution at longer wavelengths.

Because of the big mismatch between the Nd^{3+} and Y^{3+} radii, the distribution coefficient of Nd^{3+} in $Y_3Al_5O_{12}$ is very low. According to Eq. (1.1), when the distribution coefficient is very low, the resulting dopant concentration in the solid can be very low even if the concentration in the melt is high. In this case, the maximum achievable concentration for $Nd^{3+}:Y_3Al_5O_{12}$ crystal is about 2.5%. The ion size mismatch may also contribute to the formation of defects.

Results

Several Nd^{3+}:$Y_3Al_5O_{12}$ crystals with different concentration and thickness were studied. They are growth 10-63B 1.247% (3.07 mm), 10-62T 0.745% (3.2 mm), 0.24% (11 and 2 mm), and 'clean out' 0.0013% (10 mm). The labels of the crystals represent the crystal growing batches at Scientific Materials Corporation, while B denotes that the sample was cut from the bottom of the boule and T, the top. The 'clean out' batch is a $Y_3Al_5O_{12}$ crystal grown from a crucible which has just been used to grow a doped $Y_3Al_5O_{12}$ crystal. The concentrations of Nd^{3+} dopant are determined with the room temperature absorption of $^4G_{7/2}$ with reference to the 0.745% sample (concentration provided by Scientific Materials Corporation). The absorption spectra of the 0.24% and the clean out 0.0013% samples are shown in Figure 9. Since the linewidth at room temperature is dominated by the homogeneous broadening due to lattice phonon coupling, these two samples have the same linewidth ($20cm^{-1}$). As shown in Figure 9, the intensities of all components scale similarly as the concentration increases, indicating that the oscillator strength is independent of the concentration. There are rare cases where a few transitions do not scale as the others because the experimental resolution is not high enough or the oscillator strength has changed due to the lattice distortion around a defect.

Absorption spectra of several manifolds of the 10-62T 0.745% Nd^{3+}:$Y_3Al_5O_{12}$ crystal (3.2 mm) at 1.4 K were recorded ranging from 11400 cm^{-1} to 21200 cm^{-1}. An example for the $^4F_{9/2}$ manifold which has well resolved defect lines is shown in Figure 10. The linewidths of these five intrinsic transitions range from 1 cm^{-1} to 7 cm^{-1}. The lowest component $^4F_{9/2}(1)$ is inhomogeneously broadened and the upper components are

homogeneously broadened due to phonon coupling. Figure 11 shows the lowest component $^4F_{9/2}(1)$ on an expanded horizontal scale. The rounded top of the intrinsic line is due to saturation.

As we notice in Figure 11, there are 6 satellite peaks surrounding the intrinsic peak within ± 10 cm^{-1}. These satellite peaks are well resolved around the lowest component of the J-manifolds, for which the homogeneous broadening is the smallest. The detailed energy level information for intrinsic and defect sites is summarized in Table 7.

High resolution absorption spectra of $^4F_{9/2}(1)$ were measured for crystals of three different concentrations 1.247%, 0.745% and 0.24% as shown in Figure 12. The intrinsic lines for the 1.247% and 0.745% samples are saturated. The intrinsic line for the 0.24% sample has a linewidth of 1 cm^{-1} and an absorption coefficent of 4.9 cm^{-1}. The defect line intensities as functions of the concentration x are plotted in Figure 13. The defect data points are fitted with the function $ax+bx^2$. The sum of all the defect data is well fitted with a linear function.

Two more sets of data for $^4F_{3/2}(1)$ and $^4G_{7/2}(1)$ are shown in Figure 14 and Figure 15. They have the same features as for $^4F_{9/2}(1)$. The detailed defect line absorption coefficient information is summarized in Table 8.

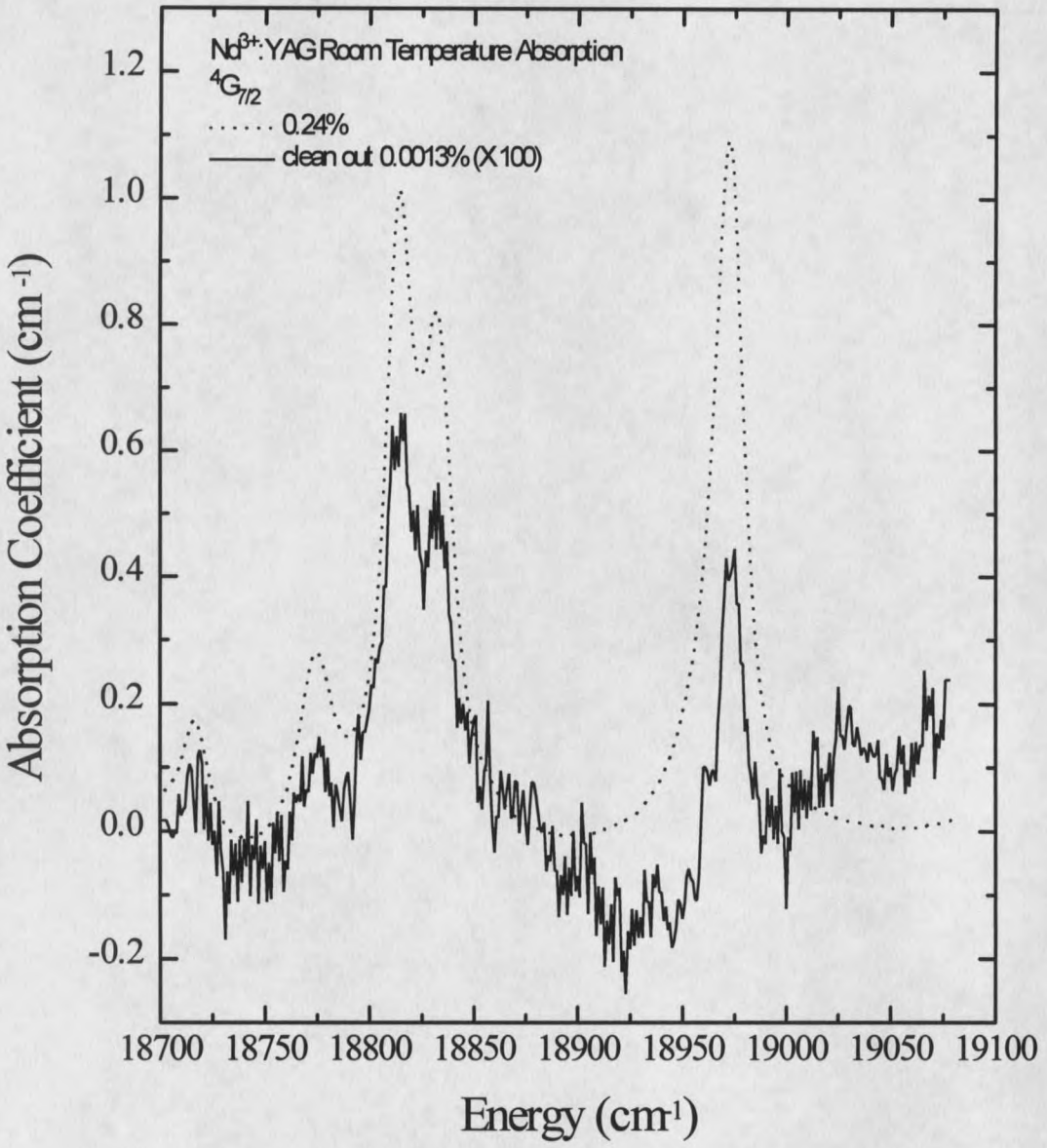

Figure 9. The room temperature absorption spectra on two Nd^{3+}:$Y_3Al_5O_{12}$ samples. The $^4G_{7/2}$ manifold is shown. The spectrum for the 0.0013% sample is expanded 100 fold.

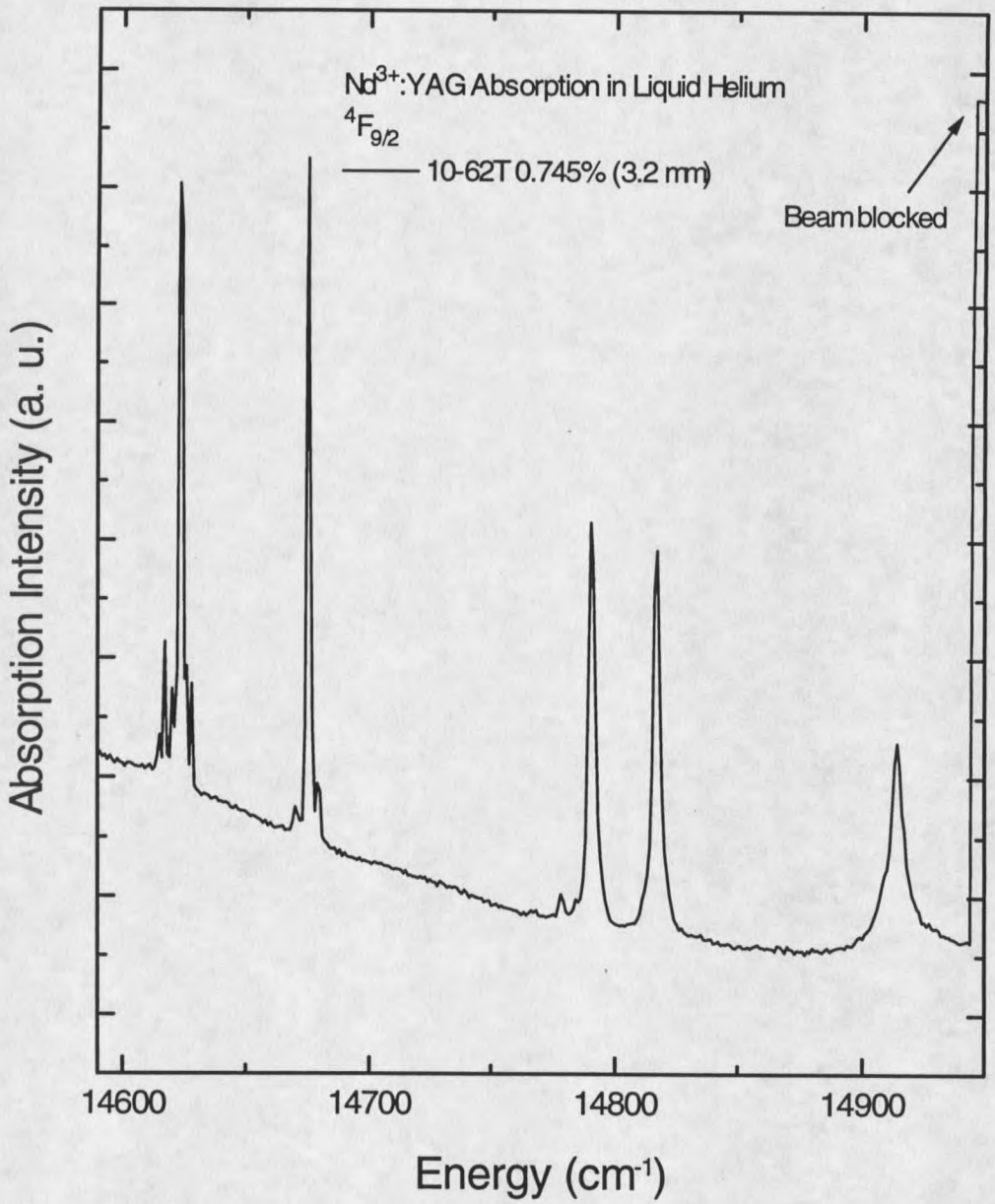

Figure 10. The absorption spectrum of the $^4F_{9/2}$ manifold of the 10-62T 0.745% Nd^{3+}:$Y_3Al_5O_{12}$ crystal (3.2 mm) at 1.4 K. The two lowest components of the intrinsic site are close to total absorption and saturated. High resolution spectra with absorption coefficients are given in Figure 12.

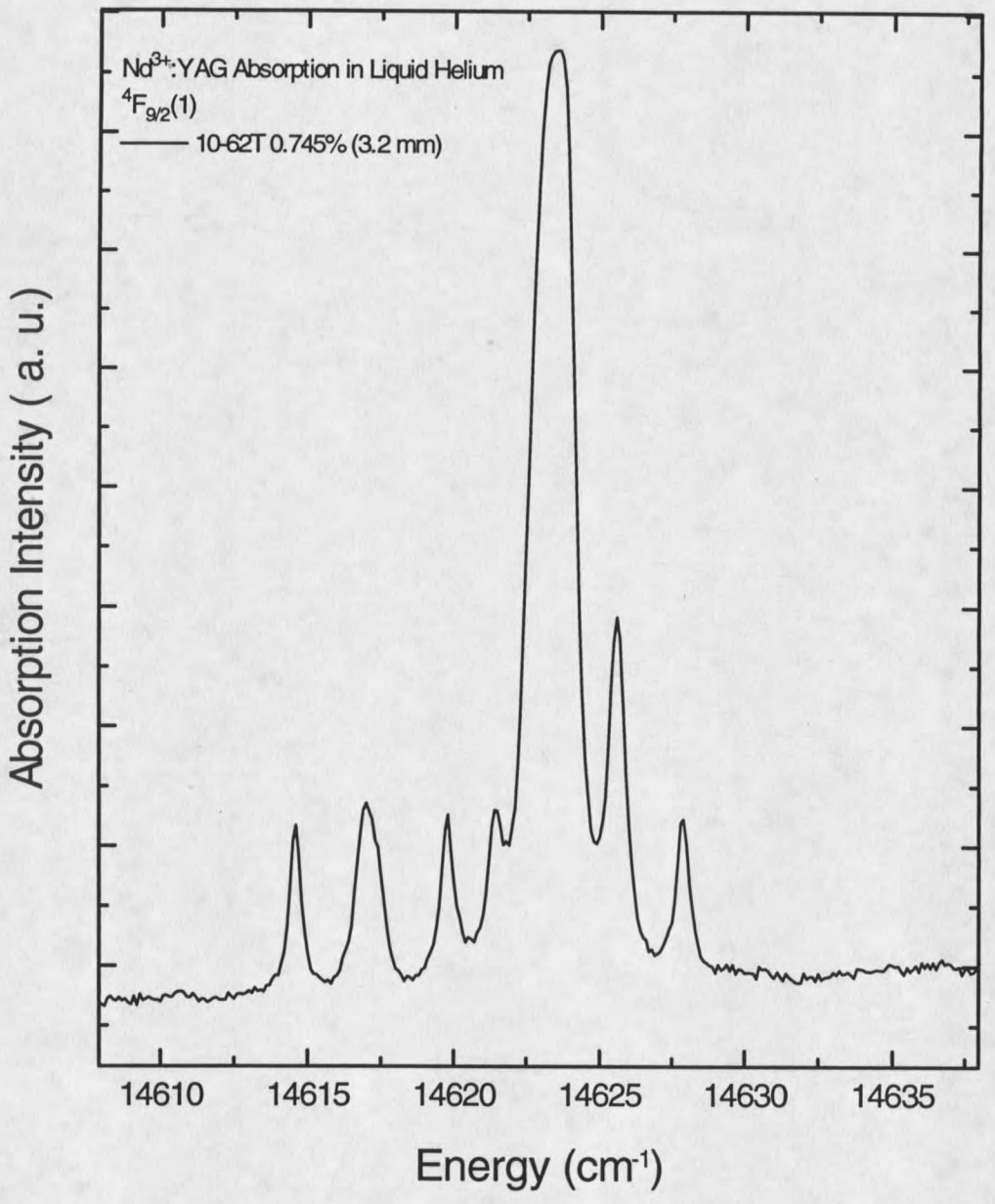

Figure 11. High resolution absorption spectrum of $^4F_{9/2}(1)$ of the 10-62T 0.745% Nd^{3+}:$Y_3Al_5O_{12}$ crystal (3.2 mm) at 1.4 K. The round shape of the intrinsic line is due to the saturation. There are 6 defect lines around the intrinsic line.

Table 7. Detailed energy level information for intrinsic and defect sites of the 10-62T 0.745% Nd^{3+}:$Y_3Al_5O_{12}$ (3.2 mm) crystal at 1.4 K. The defect transitions have about the same linewidth as the corresponding transition for the intrinsic site. The number of intrinsic levels is J+1/2 for each manifold.

Level	intrinsic site (cm^{-1})	linewidth (cm^{-1})	defect sites (cm^{-1})					
$^4F_{3/2}$	**11426.2**	**2.2**	11409.3	11421.4	11425.0	11427.2	11431.5	
	11510.9	**3.9**	11504.7	11518.7				
$^4F_{5/2}$, $^2H_{9/2}$	**12366.5**	**9.2**	12355.7					
	12428.5	**3.8**	12422.4					
	12517.4	**2.8**						
	12572.6	**12.0**	12556.3	12589.5				
	12605.0	**5.4**						
	12621.5	**6.0**						
	12824.9	**7.2**						
	12851.9	**13.6**						
$^4F_{7/2}$, $^4S_{3/2}$	**13361.0**	**16.7**	13347.1					
	13426.8	**3.7**						
	13560.6	**3.2**						
	13569.6	**4.1**						
	13593.5	**14.2**						
	13629.6	**14.4**						
$^4F_{9/2}$	**14624.5**	**1.0**	14615.7	14618.1	14620.9	14622.5	14626.7	14629.0
	14676.4	**2.0**	14671.4	14680.4				
	14791.6	**3.2**	14779.4	14785.3				
	14818.0	**3.6**						
	14915.3	**7.1**						
$^2H_{11/2}$	**15745.1**	**1.4**						
	15835.7	**2.0**						
	15870.1	**1.3**						
	15954.3	**3.1**						
	16093.1	**2.9**						
	16107.7	**4.9**						
$^2G_{7/2}$, $^4G_{5/2}$	**16847.4**	**2.8**	16841.9	16843.5	16844.3	16845.8	16848.9	16849.8
	16987.0	**11.4**	16977.9					
	17044.5	**6.4**	17035.3	17049.1				
	17241.5	**5.9**						
	17264.2	**1.06**						
	17322.5	**10.1**						
	17570.9	**23.7**	17541.7					
$^4G_{7/2}$	**18720.0**	**1.5**	18714.8	18716.5	18718.7	18721.9	18722.5	
	18819.2	**6.2**	18801.7	18812.7				

	18839.8	**7.2**	18860.8					
	18980.9	**13.4**						
$^2K_{13/2}, ^2G_{9/2}$	**19157.9**	**21.3**						
	19291.5	**20.0**						
	19321.6	**6.4**						
	19470.2	**25.3**						
	19543.0	**8.8**						
	19568.5	**16.8**						
	19612.7	**13.0**						
	19650.9	**20.5**						
	19818.5	**32.8**						
	20047.0	**53.4**						
$^4G_{9/2}, ^4G_{11/2}$	**20722.5**	**2.6**	20713.9					
	20764.3	**4.3**	20752.8					
	20782.1	**2.4**	20776.9					
	20795.1	**2.5**	20788.1					
	20970.0	**4.4**						
	21038.0	**4.1**						
	21085.2	**8.1**						
	21118.2	**8.2**						
	21160.2	**6.8**						
	21169.3	**6.7**						

Table 8. Detailed defect line absorption coefficient information of $Nd^{3+}:Y_3Al_5O_{12}$ at 1.4 K.

		Absorption Coefficient (cm^{-1})		
	Energy level (cm^{-1})	0.24% Nd^{3+}:YAG	0.745% Nd^{3+}:YAG	1.247% Nd^{3+}:YAG
$^4F_{9/2}(1)$	14615.7 (B)	0.271	0.592	0.786
	14618.1 (C)	0.127	0.687	1.749
	14620.9 (D)	0.265	0.548	0.643
	14622.5 (E)	0.173	0.294	0.286
	14626.7 (F)	0.312	1.290	2.70
	14629.0 (G)	0.245	0.532	0.70
	Sum of defect α's	1.393	3.943	6.864
$^4F_{3/2}(1)$	11409.3	0.301	0.497	0.685
	11421.4	0.066	0.383	0.93
	11425.0	0.143	0.529	0.932
	11427.2	0.078	0.443	0.842
	11431.5	0.283	0.598	0.532
	Sum of defect α's	0.871	2.45	3.921
$^4G_{7/2}(1)$	18714.8		0.537	0.977
	18716.5		0.659	0.941
	18718.7		0.198	0.517
	18721.9		0.45	0.926
	18722.5		0.786	1.328
	Sum of defect α's		2.63	4.689

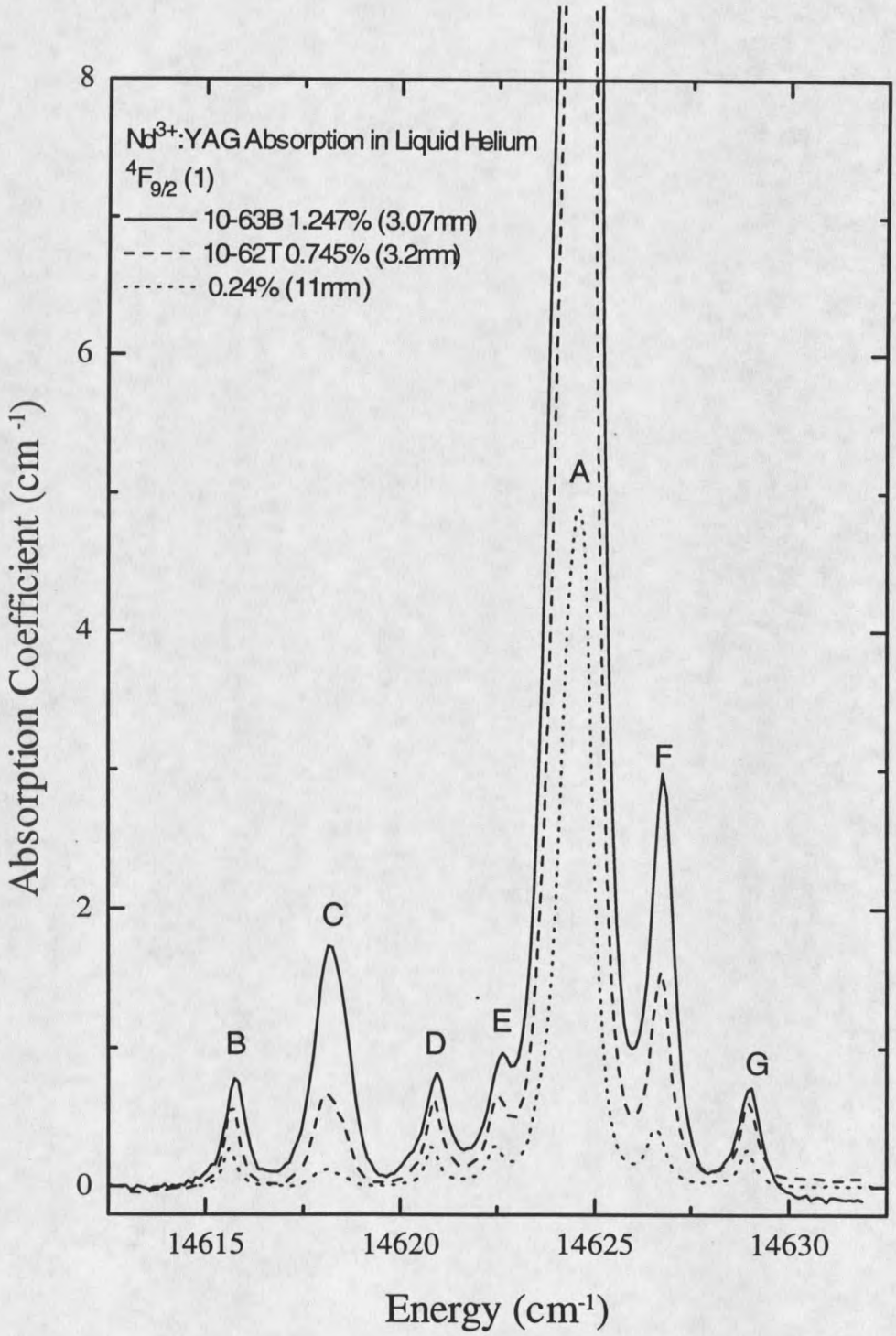

Figure 12. High resolution absorption spectra of $^4F_{9/2}(1)$ for the 1.247%, 0.745% and 0.24% Nd^{3+}:$Y_3Al_5O_{12}$ crystals. The intrinsic lines for the 1.247% and 0.745% samples are saturated. For each curve, there is one intrinsic line (A) and 6 defect lines (B, C, D, E, F, G).

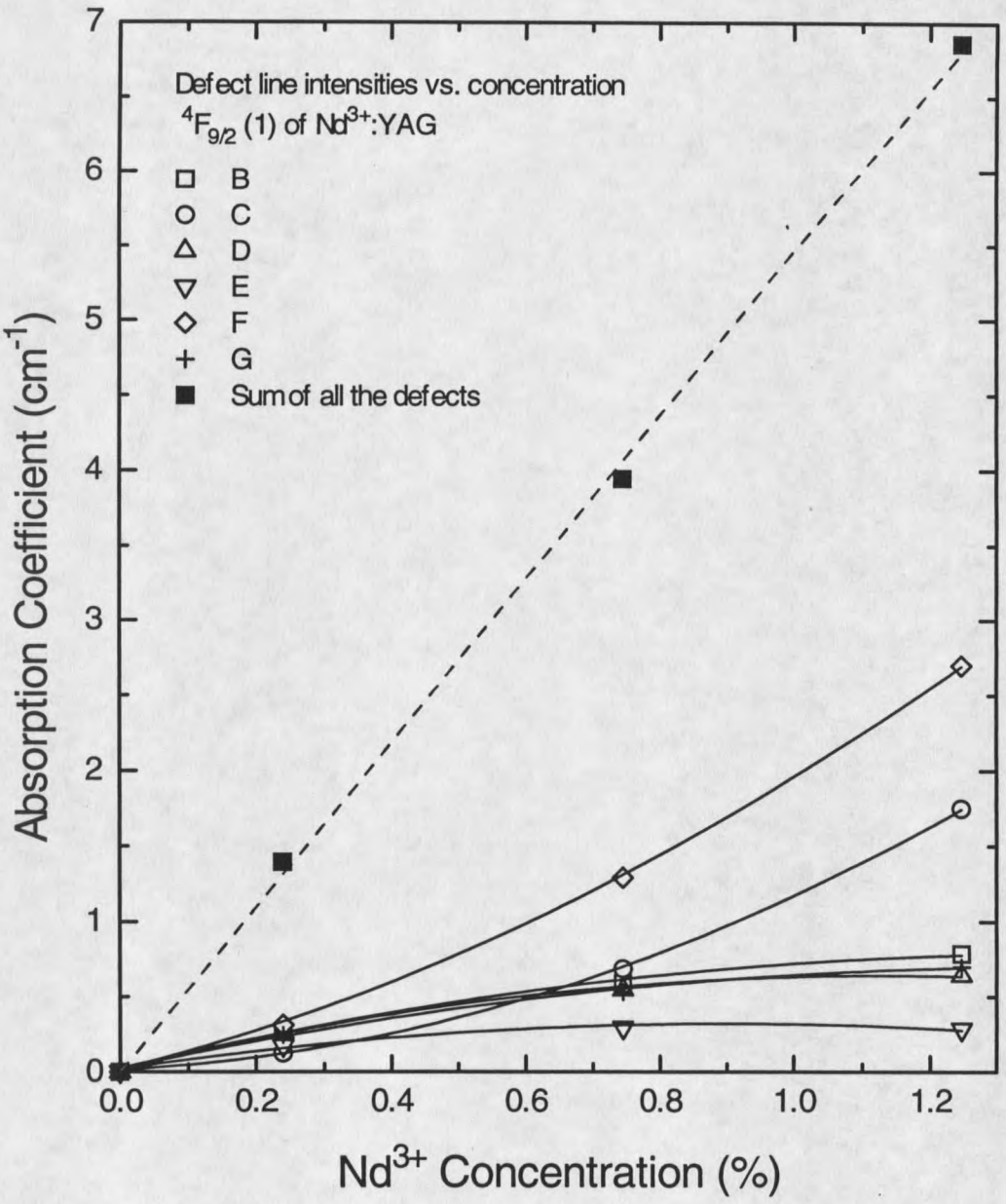

Figure 13. The $^4F_{9/2}(1)$ defect line intensities vs. concentration x. The solid lines are fits with $ax + bx^2$. The dashed line is a linear fit.

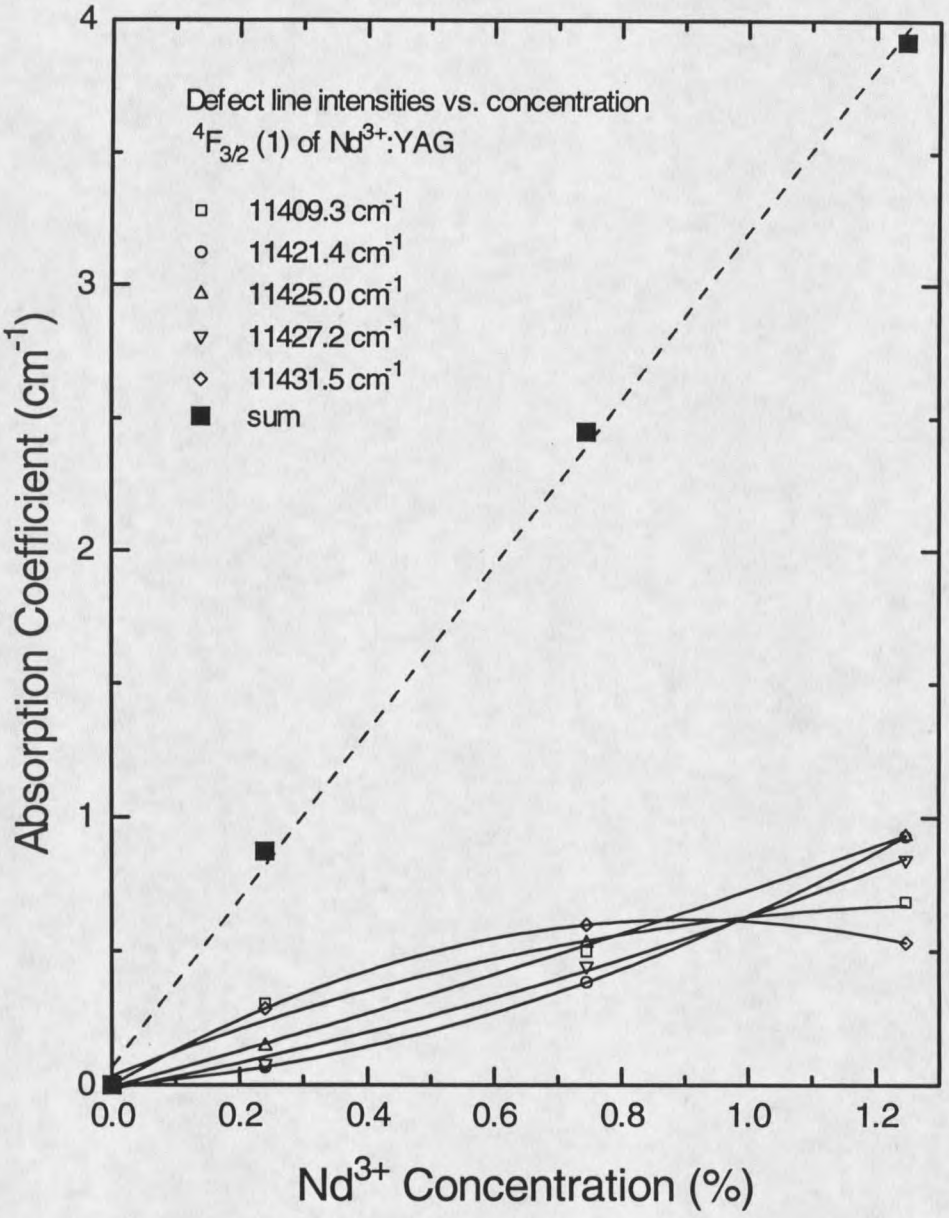

Figure 14. The $^4F_{3/2}(1)$ defect line intensities vs. concentration x. The solid lines are fits with $ax + bx^2$. The dashed line is a linear fit.

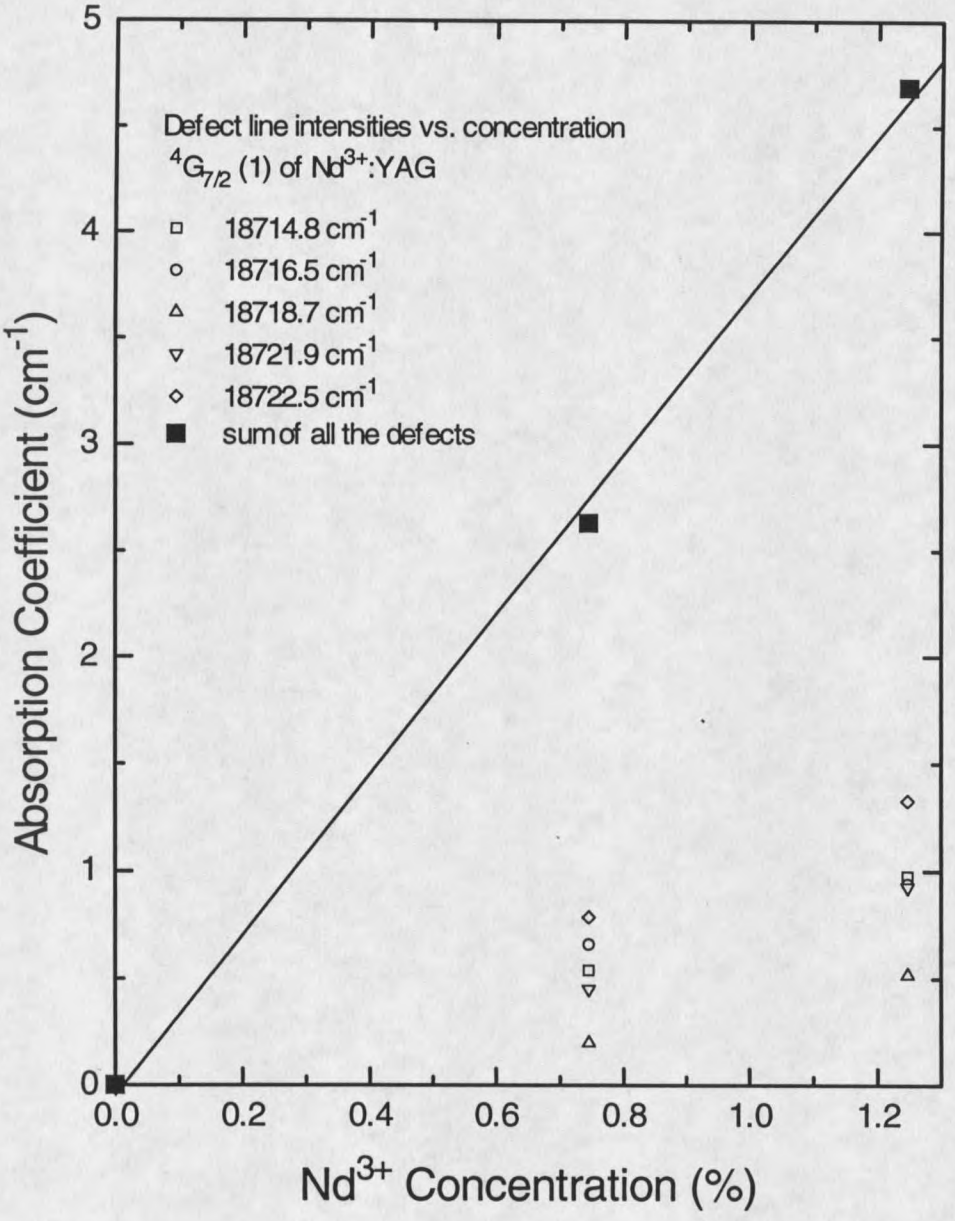

Figure 15. The $^4G_{7/2}(1)$ defect line intensities vs. concentration x. The solid line is a linear fit.

Discussion

From the spectra, we can see that defect lines exist even in the low doping (0.24%) crystal. We can separate defects into two groups. One group includes line C and F whose intensities increase faster than the concentration. The other group includes B, D, E, and G whose intensities increase slower than the concentration. None of them show linear or quadratic dependence on R^{3+} concentration. These defect lines were also observed by V. Lupei et al,[30] who claimed the relative intensities of lines B, D, and G did not depend on R^{3+} content i.e. having a linear relation with the concentration and the relative intensities of line C, E, F showed dopant-concentration dependence. By comparing the defect line intensities with the intrinsic line intensity, the percentage of Nd^{3+} ions in the all defect sites is estimated to be 20-22%. This percentage is independent of the Nd^{3+} concentration as indicated by the linear fits on Figure 13, Figure 14, and Figure 15. The intrinsic line used is the unsaturated *A* line of the 0.24% Nd^{3+}:YAG (11 mm) crystal. Since its intensity is too high, a new measurement on a thinner sample is necessary to verify this value.

Experimental Results for $Sm^{3+}:Y_3Al_5O_{12}$

Introduction

The optical spectroscopic studies on the intrinsic site of $Sm^{3+}:Y_3Al_5O_{12}$ have been published by several authors.[31-34] Recently $Sm^{3+}:Y_3Al_5O_{12}$ was used as an optical high pressure sensor based on its pressure dependent fluorescence.[35,36]

Results

White light absorption spectra were recorded on several $Sm^{3+}:Y_3Al_5O_{12}$ crystals: 1-161 10ppm (5.68 mm), 6-116 0.1% (5.49 mm) and 6-110 0.2% (4.47 mm). Most of the measurements were on the 6-110 0.2% $Sm^{3+}:Y_3Al_5O_{12}$ (4.47 mm) crystal which has strong enough absorption peaks. Several manifolds such as $^4G_{5/2}$, $^4F_{3/2}$, $^4G_{7/2}$, $^4I_{9/2}$, $^4M_{15/2}$, $^4I_{11/2}$, $^4I_{13/2}$, $^4F_{5/2}$, $^4M_{17/2}$, $^4G_{9/2}$, and $^4I_{15/2}$ were studied.

Most of the levels are close together which would make phonon relaxation more probable and spectral lines broader. The only sharp lines are transitions to $^4G_{5/2}(1)$ and $^4G_{7/2}(1)$. The peak absorption was less than 6% for both lines. At this weak absorption, it is very difficult to see the defect lines whose intensities are normally a few percent of the intrinsic line. Higher concentration crystals are needed for detailed defect line study.

When comparing the absorption spectra of different samples, we found that the 0.2% sample has 7 times more absorption than the 0.1% sample which means the concentrations of the crystals are not well determined. When pumping $^4G_{5/2}(1)$ at 17595.1

cm^{-1}, the lifetime of $^4G_{5/2}$ is 2.5 ms. The detailed energy level information for the intrinsic site is summarized in Table 9.

Table 9. Detailed energy level information for intrinsic site of Sm^{3+}:$Y_3Al_5O_{12}$ at 1.4 K.

Level	intrinsic site (cm^{-1})
$^4G_{5/2}$	**17595.1**
	17871.7
$^4F_{3/2}$	**18787.8**
	18820.5
$^4G_{7/2}$	**19821.1**
	19943.5
	19963.9
	20009.2
$^4I_{9/2}$	**20206.1**
	20220.7
	20242.9
	20325.6
	20374.4
	20408.4
$^4M_{15/2}$ & $^4I_{11/2}$	**20547.3**
	20621.7
	20687.0
	20771.6
	20850.0
	21006.2
$^4I_{13/2}$	**21413.7**
	21462.1
	21527.6
	21591.9
	21650.4
	21721.8
	21748.9

$^4F_{5/2}$	**21979.4**
	22034.7
$^4M_{17/2}$	**22227.7**
	22251.1
	22269.5
	22306.8
$^4G_{9/2}$	**22489.1**
$^4I_{15/2}$	**22780.2**
	23119.4

Experimental Results for $Eu^{3+}:Y_3Al_5O_{12}$

The optical spectroscopy of $Eu^{3+}:Y_3Al_5O_{12}$ has been investigated by Asano et al.[37] and Binnemans et al.[38]

In this section, the absorption spectra of a 1% $Eu^{3+}:Y_3Al_5O_{12}$ (3.75 mm) crystal are reported for the $^5D_1$ and $^5D_2$ manifolds. The ground state is $^7F_0$ which necessarily has Γ_1 symmetry. According to the selection rules in Table 3, $^7F_0$ (Γ_1) $\rightarrow$ $^5D_0$ (Γ_1) transition is forbidden, $^7F_0$ (Γ_1) $\rightarrow$ $^5D_1$ (Γ_2, Γ_3, and Γ_4) and $^7F_0$ (Γ_1) $\rightarrow$ $^5D_2$ (Γ_2, Γ_3, and Γ_4) transitions are allowed, and $^7F_0$ (Γ_1) $\rightarrow$ $^5D_2$ ($2\Gamma_1$) transitions are forbidden. This is exactly what we observed in Figure 16 and Figure 17 where the absorption spectra of the $^7F_0$ (Γ_1) $\rightarrow$ $^5D_1$ (Γ_2, Γ_3, and Γ_4) and the $^7F_0$ (Γ_1) $\rightarrow$ $^5D_2$ (Γ_2, Γ_3, and Γ_4) transitions are plotted. The $^7F_0$ (Γ_1) $\rightarrow$ $^5D_0$ (Γ_1) transition was not observed in this study. In the paper by Asano et al. [37],

this weak transition was observed with a thick sample and confirmed with $^5D_0(\Gamma_1) \rightarrow {}^7F_J$ fluorescence.

There are several defect lines in the vicinity of $^5D_1(1)$ and $^5D_1(2)$. An estimated 6% of Eu^{3+} ions are in the defect sites as observed by comparing the defect line intensities with the intrinsic line intensity. The transitions to $^5D_2$ were weaker, and the defect sites were unobservable in the spectrum of Figure 17.

The detailed energy level information for intrinsic and defect sites is summarized in Table 10.

Table 10. Detailed energy level information for intrinsic and defect sites of $Eu^{3+}:Y_3Al_5O_{12}$ at 1.4 K.

Level	intrinsic site (cm^{-1})	linewidth (cm^{-1})	defect sites (cm^{-1})		
$^7F_0$	**0**				
$^5D_0$	**17233**[37]				
$^5D_1$	**18945.0**	**0.5**	18941.1	18943.3	18945.9
	18947.7	**0.5**	18950.4		
	18984.6	**0.6**	18983.2	18985.3	
$^5D_2$	**21357.2**	**0.9**			
	21449.1	**1.0**			
	21472.8	**1.2**			

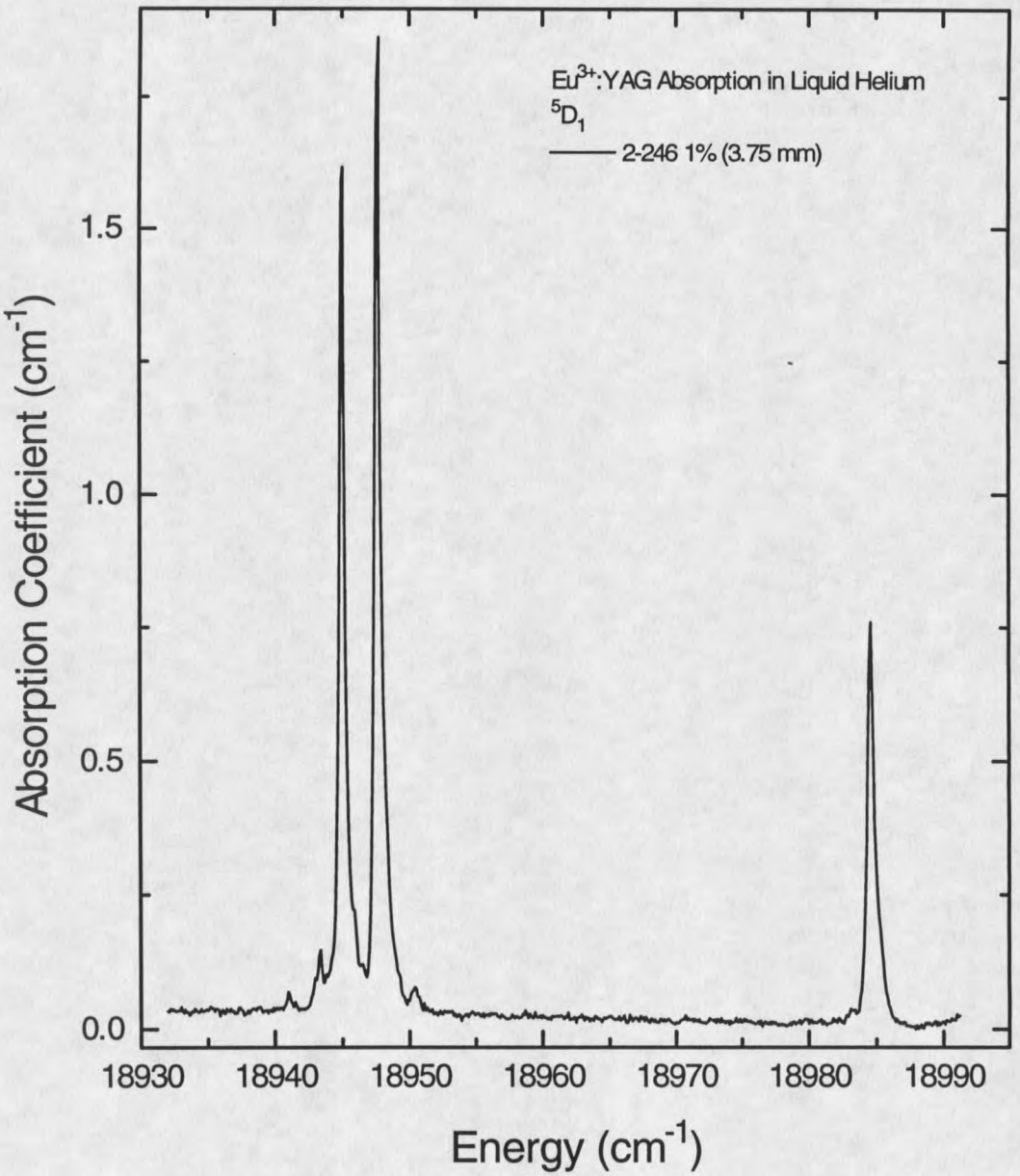

Figure 16. Absorption spectrum of the $^7F_0 \rightarrow {}^5D_1(1,2,3)$ transitions for the 1% Eu^{3+}:$Y_3Al_5O_{12}$ crystal (3.75 mm) in liquid helium. There are several defect lines in the vicinity of $^5D_1(1)$ and $^5D_1(2)$.

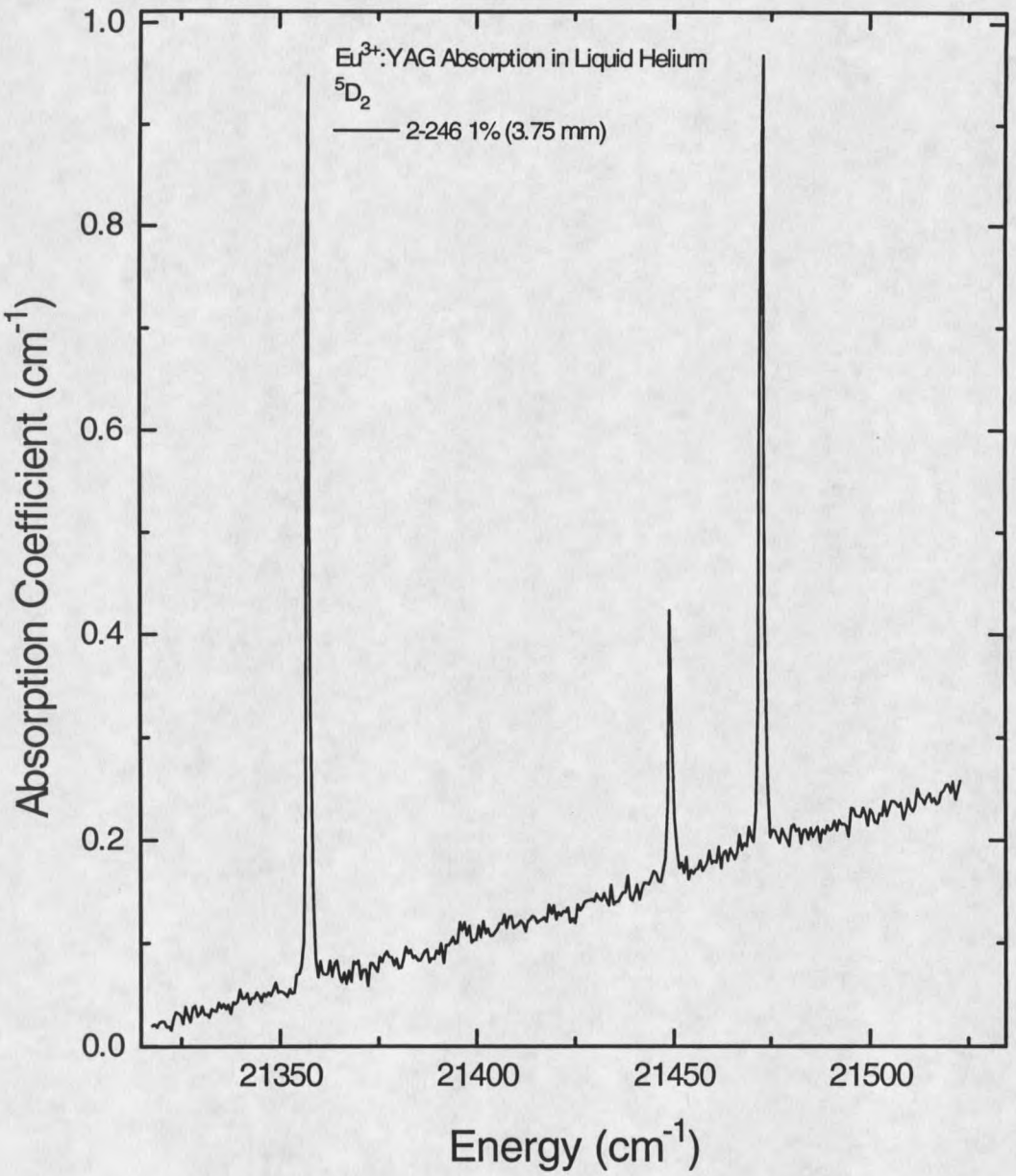

Figure 17. Absorption spectrum of the $^7F_0 \rightarrow {}^5D_2$ transitions for the 1% Eu^{3+}:$Y_3Al_5O_{12}$ crystal (3.75 mm) in liquid helium.

Experimental Results for $Ho^{3+}:Y_3Al_5O_{12}$

The optical spectroscopy of $Ho^{3+}:Y_3Al_5O_{12}$ has been investigated by Zverev et al.,[39] Johnson et al.[40] and Ashurov et al.[41] A great deal of recent scientific activity concerns developing and using new 2 μm lasers based on $Ho^{3+}:Y_3Al_5O_{12}$ crystals, with or without Tm^{3+}, Cr^{3+}, or Er^{3+} codoping.[42-56]

In our work, the absorption spectra of 0.24% $Ho^{3+}:Y_3Al_5O_{12}$ crystals were measured for the $^5F_2$, $^5F_3$, $^5F_4$, $^5S_2$, $^5F_5$, $^5I_4$ and $^5I_5$ manifolds. In the ground state manifold $^5I_8$, the first excited state $^5I_8(2)$ is only 3.9 cm^{-1} above the ground state $^5I_8(1)$. Even at 1.3 K, it still has a relatively large population according to the Boltzmann distribution:

$$p = \frac{e^{-\frac{E}{kT}}}{1 + e^{-\frac{E}{kT}}}$$ where $k = 0.7\ cm^{-1}/K$ is the Boltzmann constant.

The population percentages in $^5I_8(2)$ are 2.1% at 1.44 K and 5.4% at 1.94 K. The transition peaks originating from $^5I_8(2)$ will increase their intensities by a factor of 2.6 when the temperature is raised from 1.44 K to 1.94 K. Figure 18 shows the $^5F_3$ manifold absorption spectra at these two temperatures and three peaks from $^5I_8(2)$ are indicated with arrows. This temperature-dependent effect helped to distinguish the intrinsic lines from the defect lines.

Figure 19 shows the lowest component of the $^5F_3$ manifold. There are three defect lines around the intrinsic line. An estimated 7% of Ho^{3+} ions are in the defect sites.

The $^5S_2$, $^5F_4 \rightarrow {}^5I_8$ fluorescence transitions were observed while pumping the 21206.1 cm^{-1} line of the $^5F_2$ manifold. The fluorescence originates from two levels at

18449.8 and 18458.3 cm^{-1}. From this spectrum, the $^5I_8$ ground state manifold splittings were obtained.

The detailed energy level information for intrinsic and defect sites is summarized in Table 11.

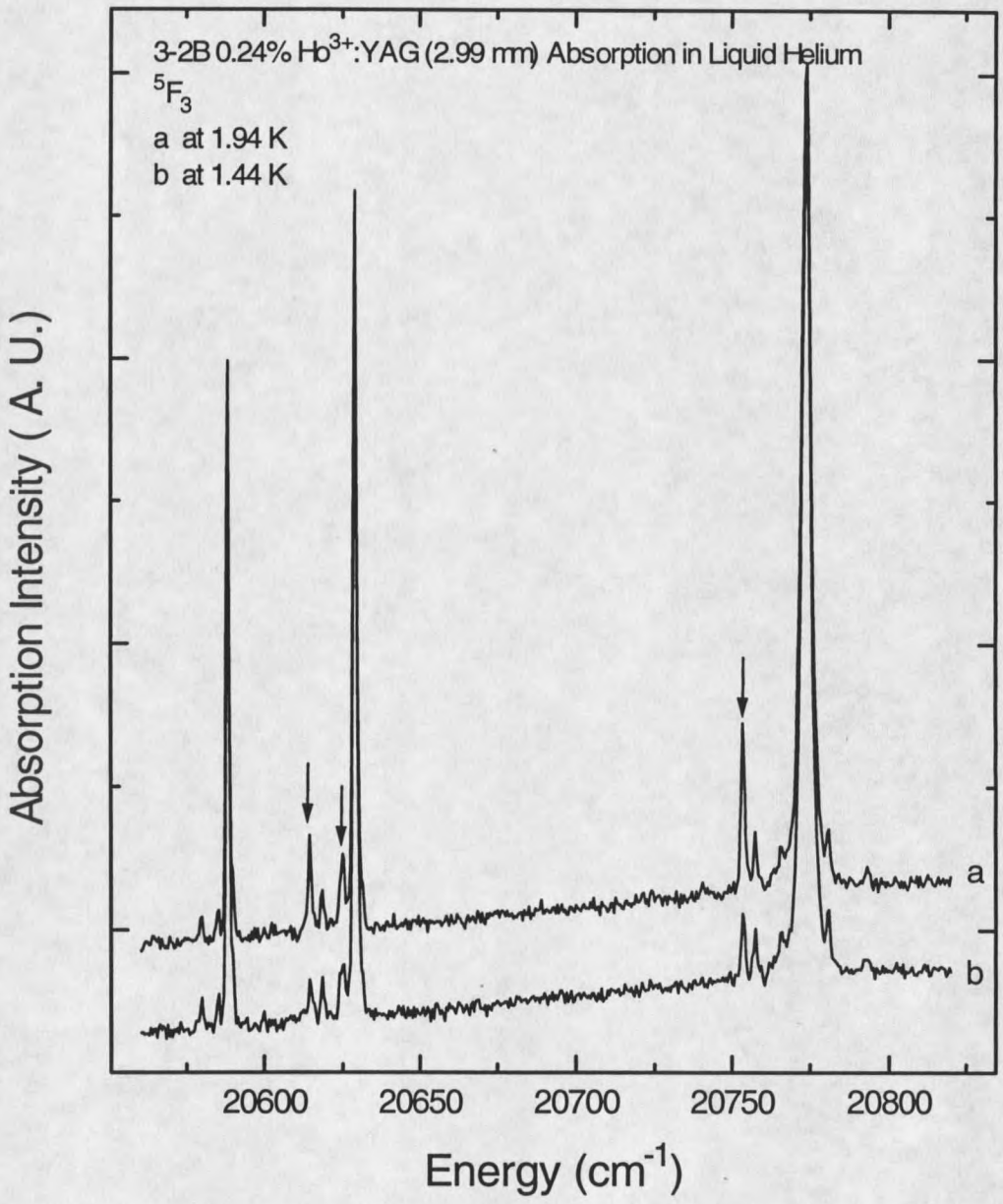

Figure 18. The $^5F_3$ manifold absorption spectra of the 0.24% Ho^{3+}:$Y_3Al_5O_{12}$ crystal(2.99 mm) at 1.94 K and 1.44 K. Three peaks originating from $^5I_8(2)$ are indicated with arrows.

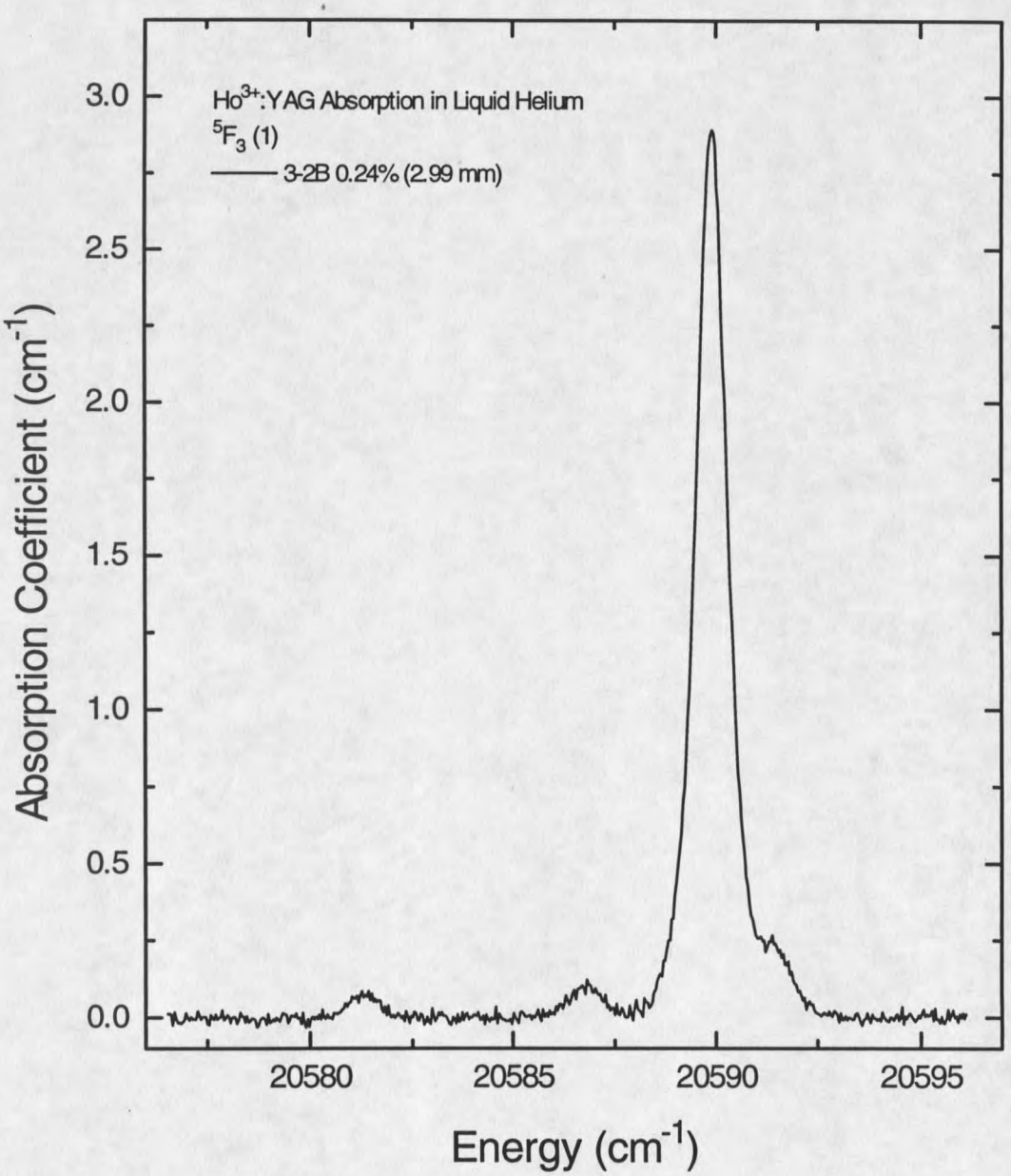

Figure 19. Absorption spectrum of the $^5F_3(1)$ of the 0.24% Ho^{3+}:$Y_3Al_5O_{12}$ crystal (2.99 mm) at 1.4 K. There are three defect lines around the intrinsic line.

Table 11. Detailed energy level information for intrinsic and defect sites of $Ho^{3+}:Y_3Al_5O_{12}$ at 1.4 K.

Level	intrinsic site (cm^{-1})	defect sites (cm^{-1})				
$^5I_8$	**0**					
	3.9					
	41.8					
	53.1					
	143.4					
	152.0					
	162.8					
	416.0					
	454.1					
	498.3					
	505.8					
	519.3					
	528.9					
$^5I_4$	**13388.4**					
$^5F_5$	**15459.2**	15458.5				
	15473.8	15475.7				
	15488.9	15484.6	15486.9	15487.7	15490.0	15491.3
	15653.3					
	15667.4					
	15695.4					
	15736.2					
	15741.4					
$^5S_2$ & $^5F_4$	**18449.8**					
	18458.3					
	18531.5					
	18539.6					
	18545.4					
	18585.5					
	18625.4					
	18664.1					

	19698.7					
	18714.0					
	18729.6					
	18743.8					
$^5F_3$	**20589.9**	20581.3	20586.8	20591.5		
	20620.0					
	20630.5	20625.7	20633.1			
	20759.0					
	20775.3	20767.5	20782.2	20794.7		
$^5F_2$	**21177.6**					
	21206.1					

Experimental Results for $Er^{3+}:Y_3Al_5O_{12}$

Introduction

$Er^{3+}:Y_3Al_5O_{12}$ has been studied extensively.[57-65] This material is used for lasers operating at 3 and 1.5 μm. The $Er^{3+}:Y_3Al_5O_{12}$ laser action in the 3-μm range[66] has received special attention, and is already being used in medical and biological applications. Recently, low concentration $Er^{3+}:Y_3Al_5O_{12}$ was considered as a potential routing material at network communications wavelength near 1.5 μm.[67]

Er^{3+} can substitute for Y^{3+} in $Y_3Al_5O_{12}$ in any percentage, and thus it provides a good system for studying the defects that are dependent on the doping concentration. At low concentration, isolated Er^{3+} ions are expected. When the concentration is high, Er^{3+}-Er^{3+} pairs will become important.

Results

Several $Er^{3+}:Y_3Al_5O_{12}$ crystals with different concentrations and thicknesses were studied. They are 3-12 1.14% (4.04 mm), 93-998 0.11% (5.52 mm), clean out #1 0.107% (10 mm), clean out #2 0.00062% (10 mm) and 100% ErAlG (3.75 mm). The concentrations of the crystals were determined from the room temperature absorption of $^2H_{11/2}$ with reference to the 93-998 0.11% sample (concentration provided by Scientific Materials Corporation). The $^2H_{11/2}$ manifold is around 19000 cm^{-1} where the absorption experimental system (comprising tungsten lamp, SPEX and PMT) has the best signal to noise ratio. The homogeneous broadening was increased to 4 cm^{-1} at room temperature, so the SPEX resolution did not limit the analysis. The absorption spectra are shown in Figure 20 and an expanded vertical scale spectrum for clean out #2 is shown in Figure 21. The integrated areas under the absorption curves were used to determine the crystal concentrations, except for the clean out #2 where signal to noise ratio was low and a peak absorption coefficient of 0.0077 cm^{-1} for the strongest component was used.

Absorption spectra of 3-12 1.14% $Er^{3+}:Y_3Al_5O_{12}$ (4.04 mm) is shown in Figure 22. The $^4S_{3/2}$ manifold absorption was measured at room temperature and 1.4 K. Line broadening and shifting due to the temperature change were obvious. The $^4S_{3/2}(1)$ was at 18384.7 cm^{-1} (linewidth 5.1 cm^{-1}) at room temperature (300 K) and at 18392.2 cm^{-1} (linewidth 1.2 cm^{-1}) at liquid helium temperature (1.4 K). This temperature dependence of energy levels is an important factor when the $^4I_{13/2}$ manifold of $Er^{3+}:Y_3Al_5O_{12}$ is used as a calibration source for the 1.5 μ wavelength region (i.e. as a potential reference source for wavelength division multiplexing).

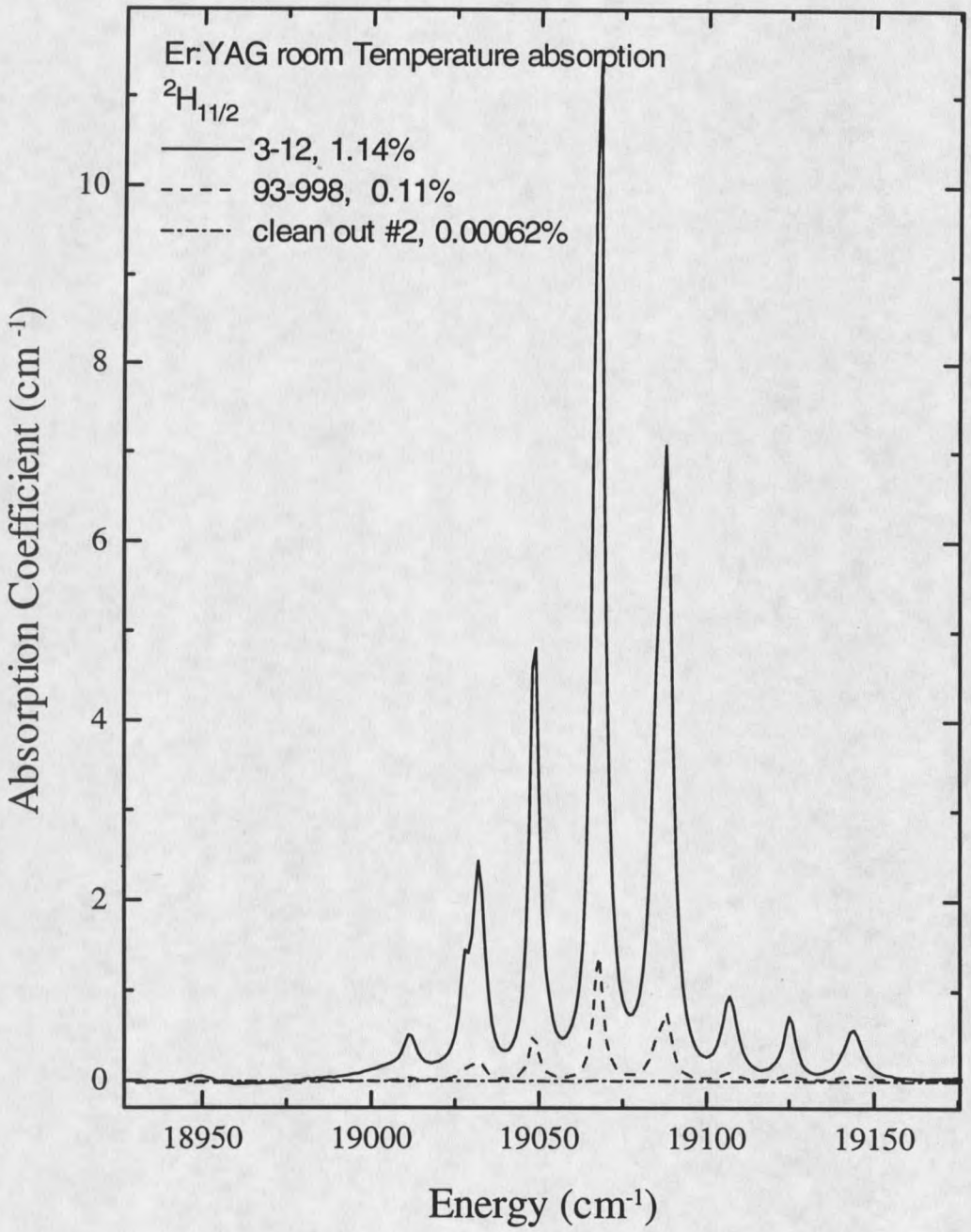

Figure 20. The room temperature absorption spectra of several Er^{3+}:$Y_3Al_5O_{12}$ samples. The $^2H_{11/2}$ manifold is shown.

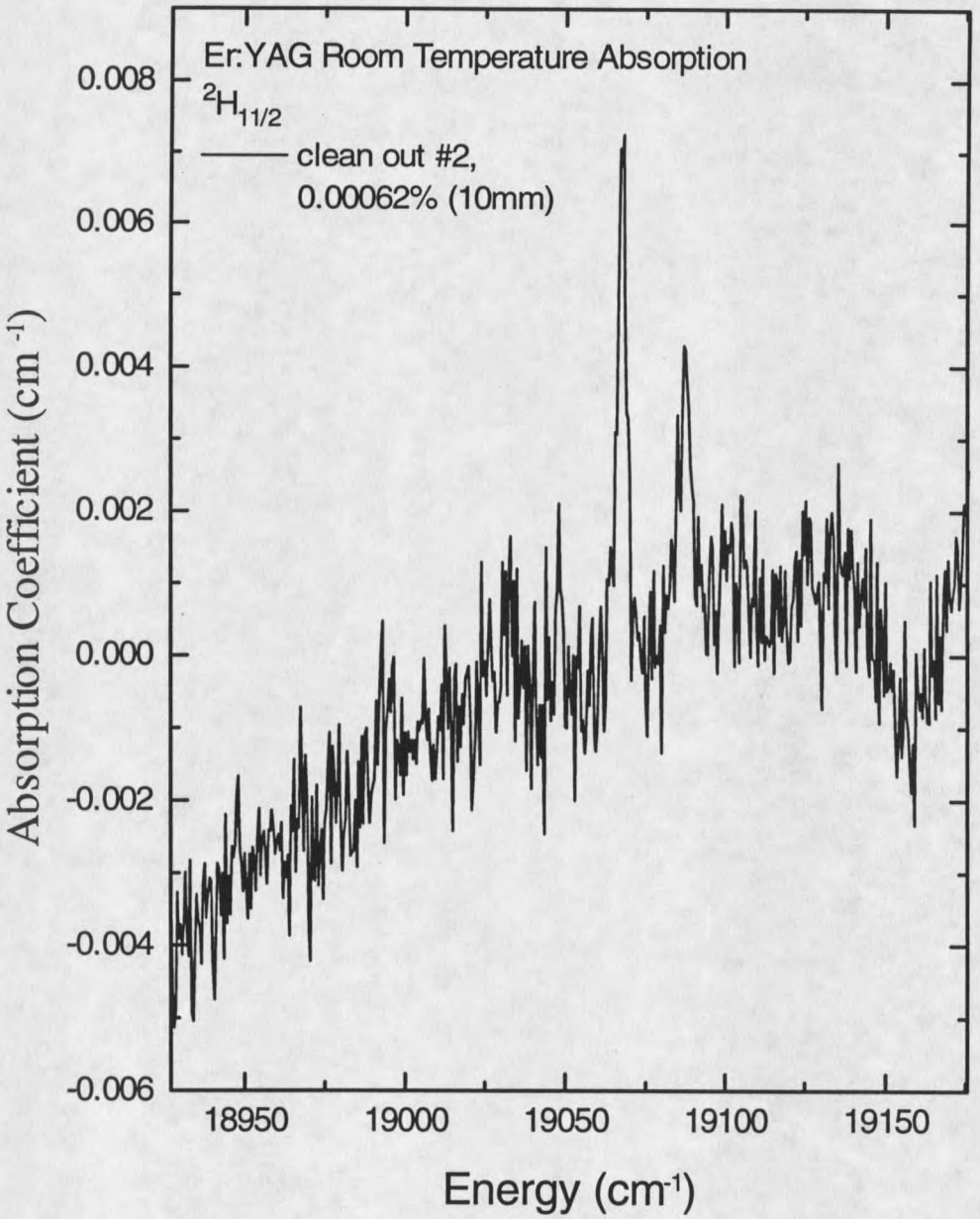

Figure 21. The room temperature absorption spectrum on the clean out #2 0.00062% Er^{3+}:$Y_3Al_5O_{12}$ (10 mm) sample. The $^2H_{11/2}$ manifold is shown. The peak absorption coefficient is used for concentration calibration.

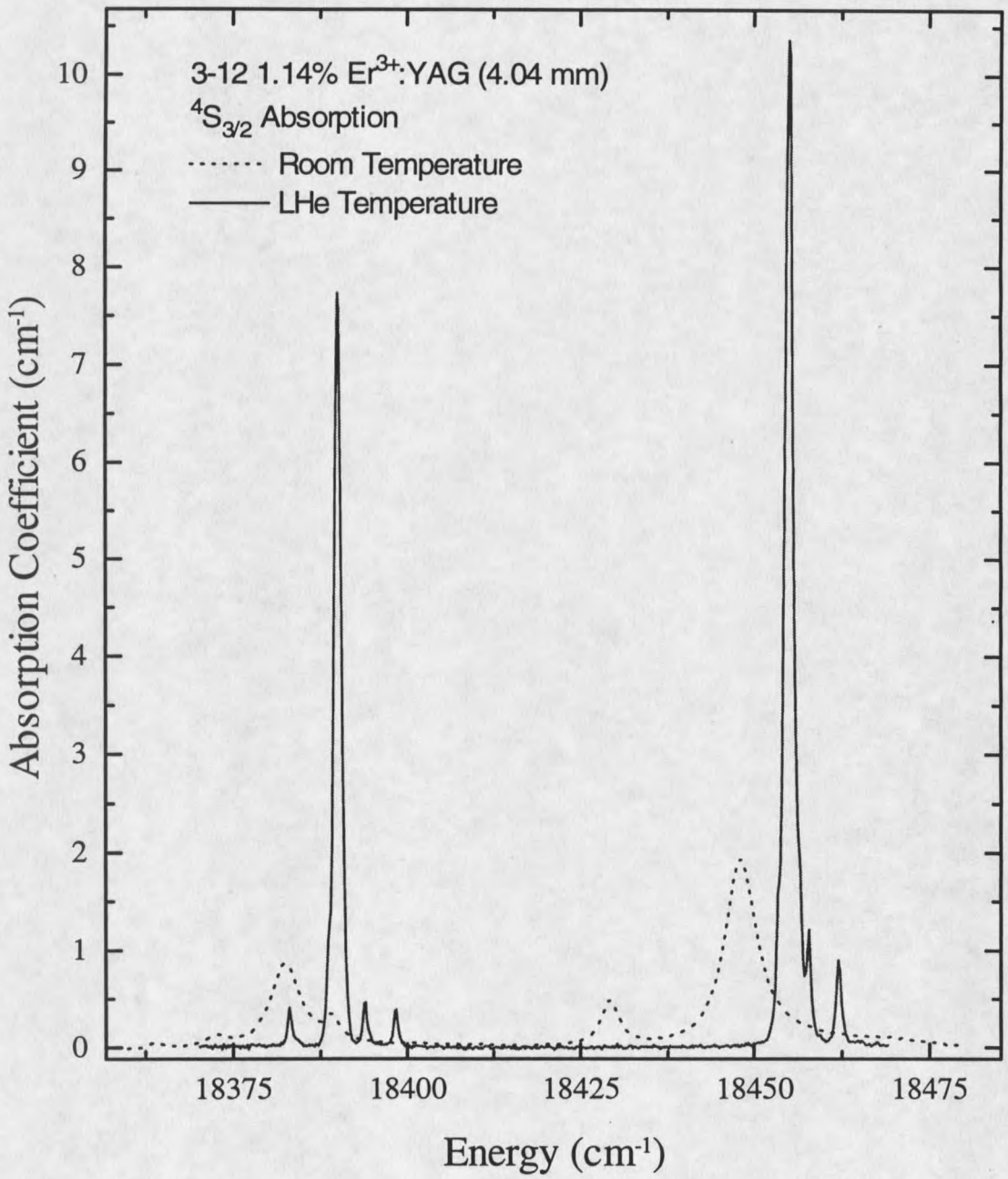

Figure 22. Absorption spectra of the 3-12 1.14% Er^{3+}:$Y_3Al_5O_{12}$ crystal (4.04 mm). The $^4S_{3/2}$ manifold absorption was measured both at room temperature and at 1.4 K. Some of the lines in the room temperature spectrum are hot absorption transitions.

Absorption spectra of several manifolds were studied. There are 4 satellite peaks surrounding each intrinsic peak as shown in Figure 22. These satellite peaks are distinguished around the lowest component of the manifolds where the homogeneous broadening is the smallest. The detailed energy level information for intrinsic and defect sites is summarized in Table 12.

Table 12. Detailed energy level information for intrinsic and defect sites with linewidth in parenthesis obtained with the 3-12 1.14% Er^{3+}:$Y_3Al_5O_{12}$ (4.04 mm) crystal at 1.4 K. The levels in the same column for defect sites do not necessarily belong to the same site except when in bold type. The number of intrinsic levels is J+1/2 for each manifold.

Level	intrinsic site (cm^{-1})	linewidth (cm^{-1})	defect sites (cm^{-1})			
$^4I_{15/2}$	**0**		**0**	**0**	**0**	
	22.6		**27.4**	**26.2**	**29.2**	
	60.6		**61.4**	**59.2**	**60.2**	
	79.6		**81.4**	**79.2**	**96.2**	
	416.9		**425.4**	**418.2**	**407.2**	
	430.7		**450.4**	**452.2**	**439.2**	
	573.6		**576.4**	**571.2**	**552.2**	
	(miss one level)				**589.2**	
$^4I_{13/2}$	N/A					
$^4I_{11/2}$	N/A					
$^4I_{9/2}$	**12301.5**	0.5				
	12526.3	1.0				
	12575.9					
	12717.7	7.5				
	12762.9	3.0				
$^4F_{9/2}$	**15286.8**	2.4	**15295.7**	**15292.8**	**15270.3**	15285.1
	15311.8	1.2	15310.0	15313.8	15318.4	15322.4
	15355.7	2.2	15352.8	15354.6	15359.4	15363.5
	15471.6	7.5				
	15517.2	4.8				

$^4S_{3/2}$	**18392.2**	1.2	**18400.1**	**18395.7**	**18384.8**	18390.6
	18456.7	2.5	**18458.3**	**18455.4**	**18463.8**	18459.5
$^2H_{11/2}$	**19091.0**	3.6	19094.8			
	19112.0	2.8	19116.6			
	19149.1	4.0				
	19344.8	4.5	19352.7			
	19362.6	4.1	19367.8			
	(miss one level)					
$^4F_{7/2}$	**20511.1**	2.2	20501.7	20509.5	20515.9	20520.2
	20567.3	1.0	20565.7			
	20646.0	2.2				
	20697.7	3.2				
$^4F_{5/2}$	**22215.4**	2.0	22210.7	22213.6	22218.0	22222.4
	22235.0	1.0				
	22282.8	1.2	22288.4			
$^4F_{3/2}$	**22584.3**	17.6				
	22659.5	27.0				
$^2H_{9/2}$	**24417.3**	1.9				
	24571.7	2.1	24563.1	24575.8		
	24587.0	2.7	24592.5	24597.9		
	24759.8	3.4				
	24779.9	5.3				
$^4G_{11/2}$	**26207.2**	4.8				
	26269.5	3.9				
	26315.5	2.5				
	26559.3	5.4				
	26566.5	7.4				
	26597.5	10.1				

Since $^4S_{3/2}$ has only two intrinsic lines, the defect lines are easily distinguished from the intrinsic lines. Most fluorescence experiments were done on this manifold. The energy levels for the $^4I_{15/2}$ manifold were obtained by selectively pumping individual $^4S_{3/2}$ lines including the intrinsic site and three defect sites. The fluorescence spectra for the $^4S_{3/2} \rightarrow {}^4I_{15/2}$ transitions are shown in Figure 23. The $^4S_{3/2}$ lifetimes of these sites are very similar, i.e. 17.9 μs for intrinsic site, 17.3, 17.1 and 17.0 μs for the other three. The

fluorescence excitation spectrum of $^4S_{3/2}$ was recorded for each site as shown in Figure 24, as an aid to distinguishing the excited state energy levels.

Discussion

From the spectra, it is noticed that there were defect lines present even with low doping concentration such as 0.1%. When 3-12 1.14% Er^{3+}:$Y_3Al_5O_{12}$ (4.04 mm) and 93-998 Er^{3+}:$Y_3Al_5O_{12}$ 0.11% (5.52 mm) are compared with each other, the absorption coefficients of the intrinsic lines and defect lines all scale as the concentration. An estimated 6.5-8% of Er^{3+} ions are in the defect sites. The defect lines are normally found within ± 60 cm^{-1} of the intrinsic line.

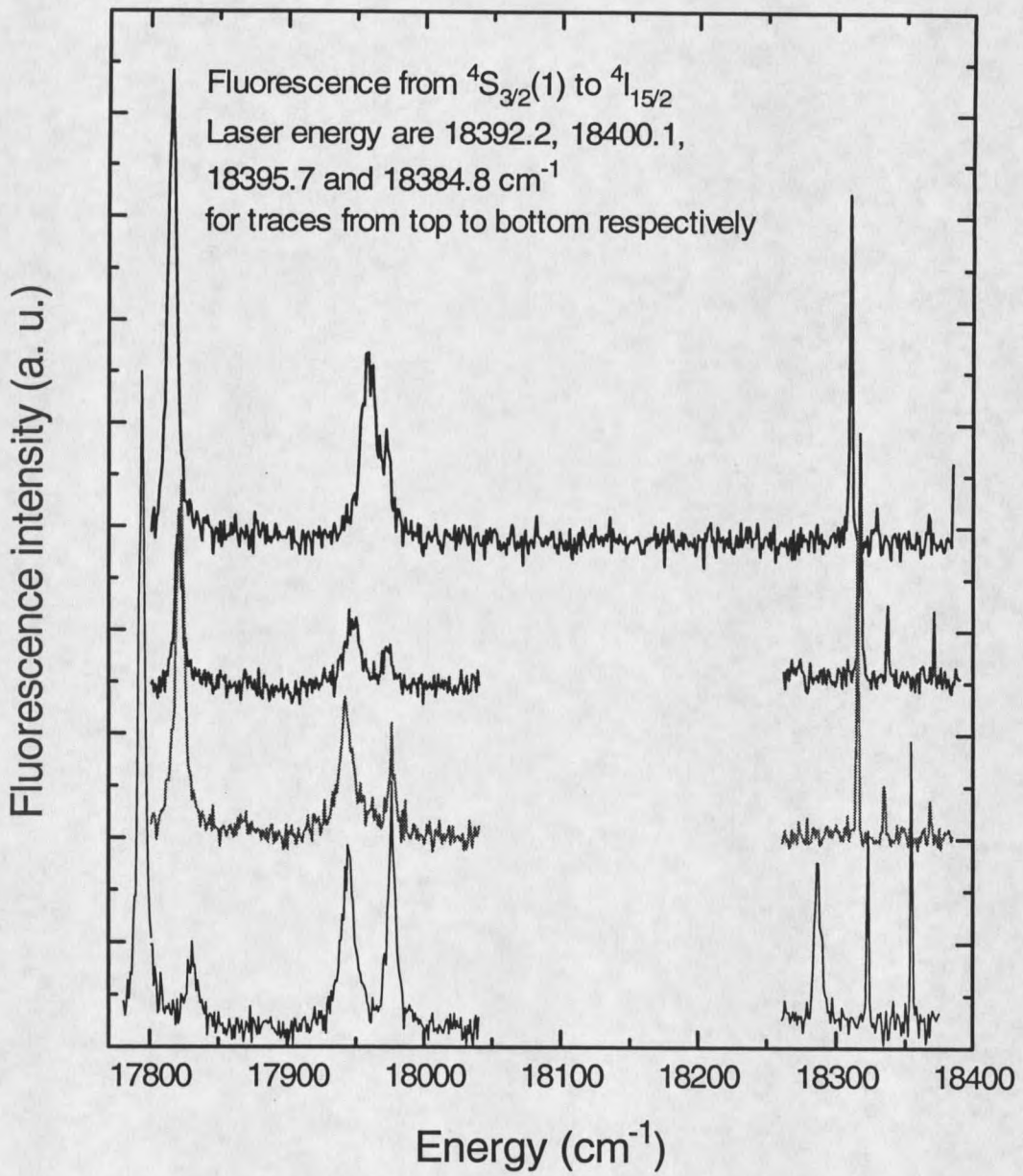

Figure 23. The fluorescence spectra of $^4S_{3/2} \rightarrow {}^4I_{15/2}$ for the 3-12 1.14% Er^{3+}:$Y_3Al_5O_{12}$ crystal (4.04 mm) at 1.4 K. The top trace is for the intrinsic site. The other traces are for three defect sites.

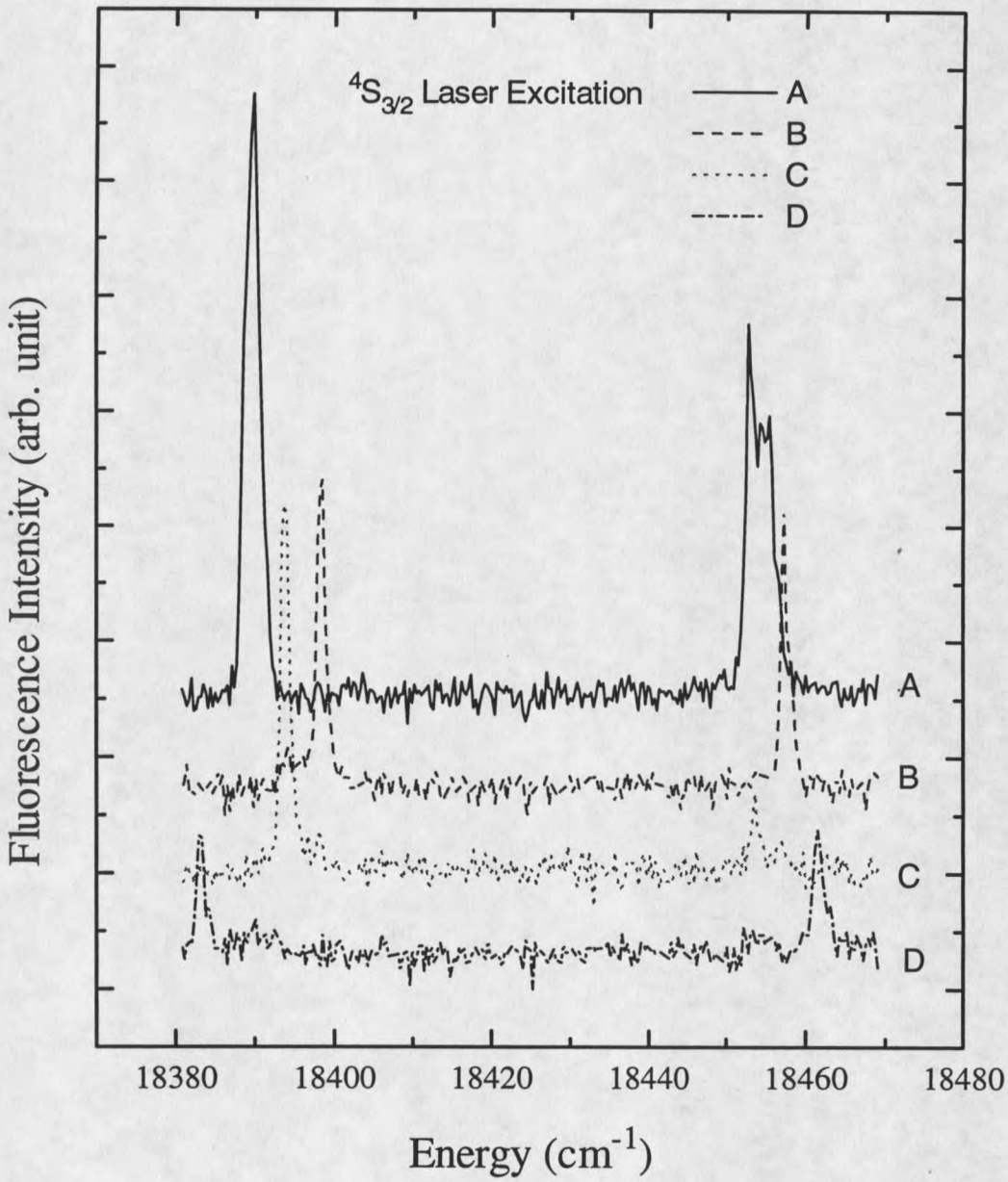

Figure 24. The fluorescence excitation spectrum was recorded for each site by monitoring its $^4S_{3/2}(1) \rightarrow {}^4I_{15/2}$ (3) transition. A is for the intrinsic site; B, C, and D are for the three defect sites.

Experimental Results for $Tm^{3+}:Y_3Al_5O_{12}$

Introduction

$Tm^{3+}:Y_3Al_5O_{12}$ has proved to be particularly successful in solid-state laser systems for emission in the 2 μm range[68-70] which is of great practical interest. The detailed investigations performed by Gruber *et al.*[71] and Lupei *et al.*[72] on $Tm^{3+}:Y_3Al_5O_{12}$ spectra indicated that the Tm^{3+} ions preferentially occupy dodecahedral D_2 (Y^{3+}) positions as the other R^{3+} ions do, although several weak satellites attributed to perturbed sites were noticed. The most intense lines were analyzed using the selection rules for D_2 symmetry, while the other weak peaks whose relative intensity was independent of Tm^{3+} content were recorded but not analyzed.

In this section, we try to elucidate the satellite structure of the spectral lines with high resolution absorption spectroscopy.

Results

The absorption spectra for 3-8 1% $Tm^{3+}:Y_3Al_5O_{12}$ (5.48 mm) and 6-231 0.1% $Tm^{3+}:Y_3Al_5O_{12}$ (5.52mm) crystals were measured for the $^3H_4$, $^3F_3$, $^3F_2$, and $^1G_4$ manifolds. A characteristic of the spectra is that, for each multiplet, the lines at higher energies are broadened due to phonon interaction. For the lowest component, where inhomogeneous broadening dominates, several small peaks can be seen around the main intrinsic peak. Figure 25 shows the full spectrum of the $^1G_4$ manifold. Figure 26 and Figure 27 show the

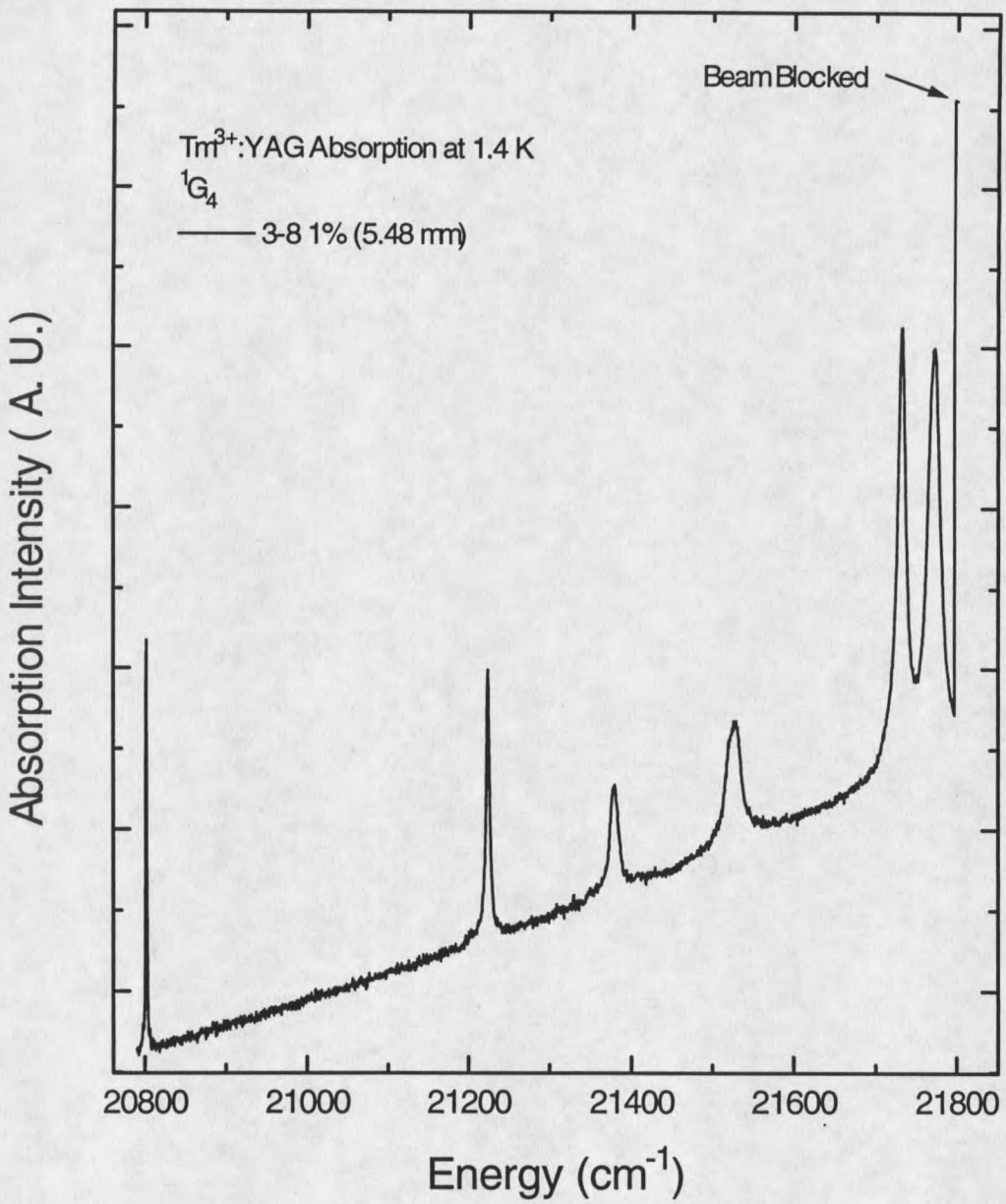

Figure 25. Absorption spectrum of the full multiplet of $^1G_4$ for the 1% Tm^{3+}:$Y_3Al_5O_{12}$ crystal at 1.4 K.

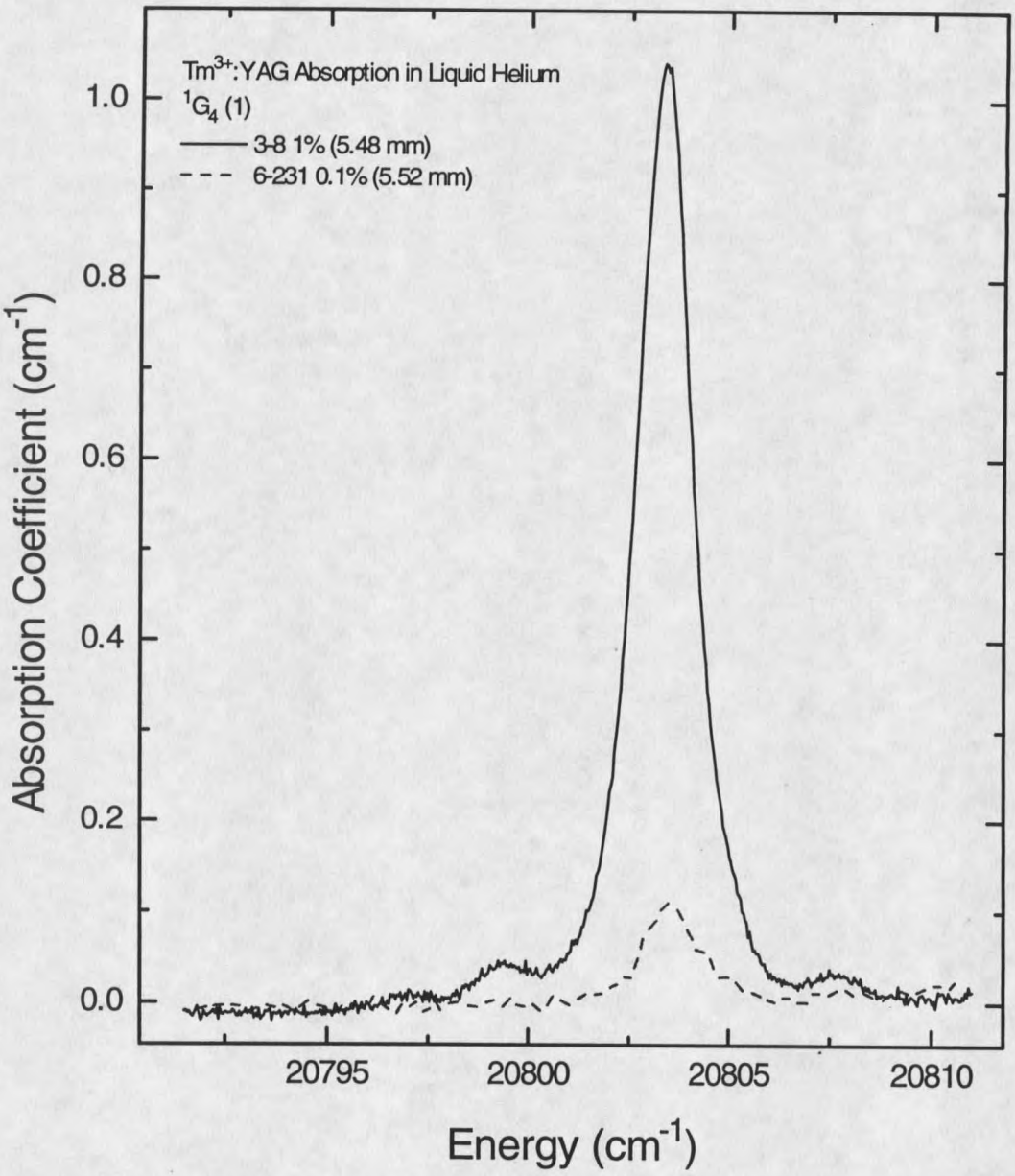

Figure 26. Absorption spectra of the lowest components of $^1G_4$ for the 1% and the 0.1% Tm^{3+}:$Y_3Al_5O_{12}$ crystals at 1.4 K.

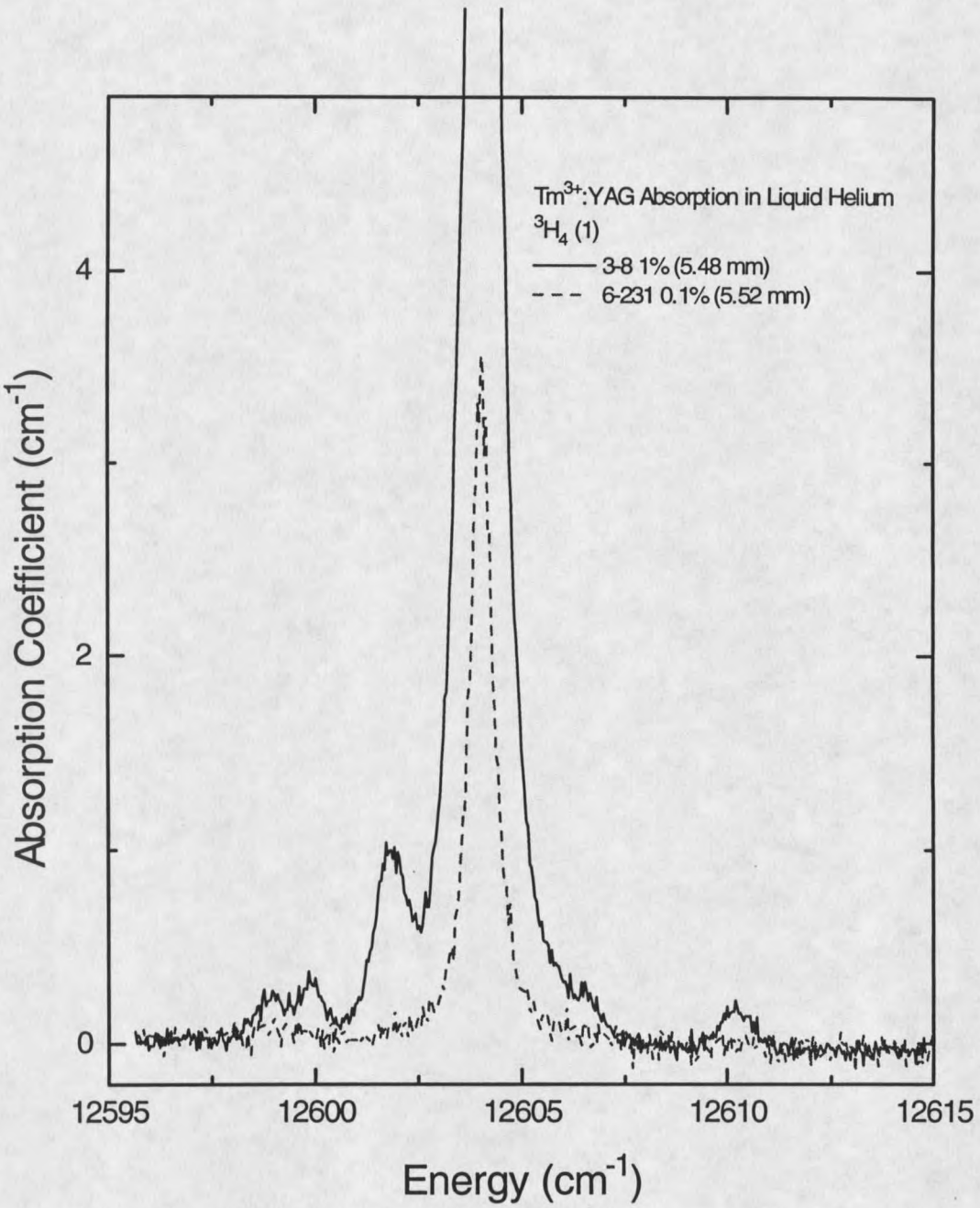

Figure 27. Absorption spectra of the lowest components of $^3H_4$ for the 1% and the 0.1% $Tm^{3+}:Y_3Al_5O_{12}$ crystals. The intrinsic line of the 3-8 1% $Tm^{3+}:Y_3Al_5O_{12}$ (5.48 mm) crystal is saturated. A thinner crystal needs to be used to obtain the intrinsic line absorption coefficient.

absorption coefficient of the lowest components of $^1G_4$ and $^3H_4$ respectively. The detailed energy level information for intrinsic and defect sites is summarized in Table 13.

Table 13. Detailed energy level information for intrinsic and defect sites of Tm^{3+}:$Y_3Al_5O_{12}$ at 1.4 K.

Level	intrinsic site (cm^{-1})	defect sites (cm^{-1})					
$^3H_6$	**0**						
	27.0						
	218.6						
	240.0						
	247.4						
	452.8						
	591.3						
$^3F_4$	**5759.0**						
	5832.1						
	5900.6						
	6170.8						
$^3H_5$	**8339.3**						
	8344.9						
	8515.3						
	8538.2						
	8555.8						
$^3H_4$	**12604.1**	12598.9	12599.9	12601.8	12606.5	12610.2	
	12745.2						
	12821.0						
	13068.9						
$^3F_3$	**14656.1**						
	14677.7						
	14703.8						
	14719.1						
	14737.3						
$^3F_2$	**15239.1**						

	15259.1						
	15432.2						
$^1G_4$	**20803.4**	20788.6	20797.1	20799.4	20807.7	20810.6	20817.1
	21225.4						
	21380.4						
	21527.6						
	21734.5						
	21774.0						
$^1D_2$	**27874**						

An estimated 4-5% of Tm^{3+} ions are in the defect sites by comparing the defect line intensities with the intrinsic line intensities for $^3H_4(1)$ and $^1G_4(1)$.

For higher sensitivity, the laser excitation spectra were recorded around the $^1G_4(1)$ region, revealing additional defect lines at 20788.6, 20810.6 and 20817.1 cm^{-1} not observed in the white light absorption spectra. The laser excitation spectra clearly showed that both 3-8 1% Tm^{3+}:$Y_3Al_5O_{12}$ (5.48 mm) and 6-231 0.1% Tm^{3+}:$Y_3Al_5O_{12}$ (5.52mm) crystals had the same defect lines.

Conclusions

In this chapter, we have investigated the defect lines in several R^{3+}:$Y_3Al_5O_{12}$ systems. For each R^{3+}:$Y_3Al_5O_{12}$ system, there are 3-6 defect lines within ± 60 cm^{-1} of some intrinsic lines. One possible explanation for this is that the mismatch of the R^{3+} radii with the Y^{3+} radius causes some of these defects. The R^{3+} radii and Y^{3+} radius are plotted in Figure 28.[73] Since the Ho^{3+} radius is very close to the Y^{3+} radius, we expect that the defect site concentration in Ho^{3+}:$Y_3Al_5O_{12}$ should be very small. At the other end,

Pr^{3+} and Nd^{3+} have very large radii compared to Y^{3+}, and we would expect correspondingly more defects for Pr^{3+} and Nd^{3+} doped $Y_3Al_5O_{12}$ crystals.

The relative absorption intensities of the intrinsic and defect sites were used to determined the defect site concentrations. In each rare earth ion doped YAG system, un-saturated intrinsic peaks were found for use in the calculation. The calculation is based on the approximation that the oscillator strength is independent of the rare earth site. Because the site distortion tends to increase the level mixing which in turn might change the oscillator strength, these percentages should be considered as rough estimates to establish the upper limits of the defect concentration.

The percentages of R^{3+} ions in defect sites are plotted vs. radii of the R^{3+} ions in Figure 29. Several kinds of evidence show that the origin of the defects comes from the host $Y_3Al_5O_{12}$ crystal itself rather than the mismatch of the ionic radii. They are listed below:

(1) Even for Ho^{3+} whose radius is the closest to the Y^{3+} radius within the lanthanide group, 7% of Ho^{3+} ions still reside in defect sites.

(2) The percentages of Tm^{3+}, Er^{3+}, Ho^{3+} and Eu^{3+} in defect sites are around 4-8%. There is not a strong correlation between the defect percentages and the radii.

(3) The total defect percentages showed a linear relation with dopant concentration in both the Nd^{3+}:$Y_3Al_5O_{12}$ and Er^{3+}:$Y_3Al_5O_{12}$ systems.

(4) Even for 0.018% Pr^{3+}:$Y_3Al_5O_{12}$ 15% of Pr^{3+} ions reside in defect sites. Pair concentration is expected to be negligible at this low dopant according to Eq. (1.2).

By measuring crystal lattice constants, the compositions of garnet crystals were found to be different for Czochralski and flux growths.[74] $Y_3Al_5O_{12}$ crystals grown from the melt at 1970 °C have the estimated formula $Y_3(Al_{0.985}Y_{0.015})_2Al_3O_{12}$ which indicates that 1% of all the Y^{3+} ions substitute for Al^{3+} in *a* sites (C_{3i} symmetry). These special *a* sites occupied by Y^{3+} perturb their neighboring *c* sites (D_2 symmetry). From Table 4, six *c* sites lie within sphere I of an *a* site. When the R^{3+} ions randomly substitute for the Y^{3+} ions, 6% of the R^{3+} ions will go into the perturbed *c* sites according to Eq. (1.2) with n'=1 and m'=6. This percentage agrees with what has been measured.

For Nd^{3+} and Pr^{3+}, the defect percentages are around 15-20%. This may due to the large radii of these two ions compared to Tm^{3+}, Er^{3+}, Ho^{3+} and Eu^{3+}. It is well known that the large mismatch between Nd^{3+} and Y^{3+} radii makes it impossible to grow Nd^{3+}:$Y_3Al_5O_{12}$ crystals with concentrations higher than 2.5%. When Y^{3+} ions substitute for Al^{3+} ions, the radius mismatch between Y^{3+} and Al^{3+} ions causes distortion for the neighboring perturbed sites. The large radius of the Nd^{3+} and Pr^{3+} ions may cause them to have a preferred distribution toward these perturbed sites, hence the defect percentages are larger.

More arguments for the defect forming mechanisms will be provided in Chapter 3 when the defects of Pr^{3+}:$Y_3Al_5O_{12}$ are studied using ODNMR techniques.

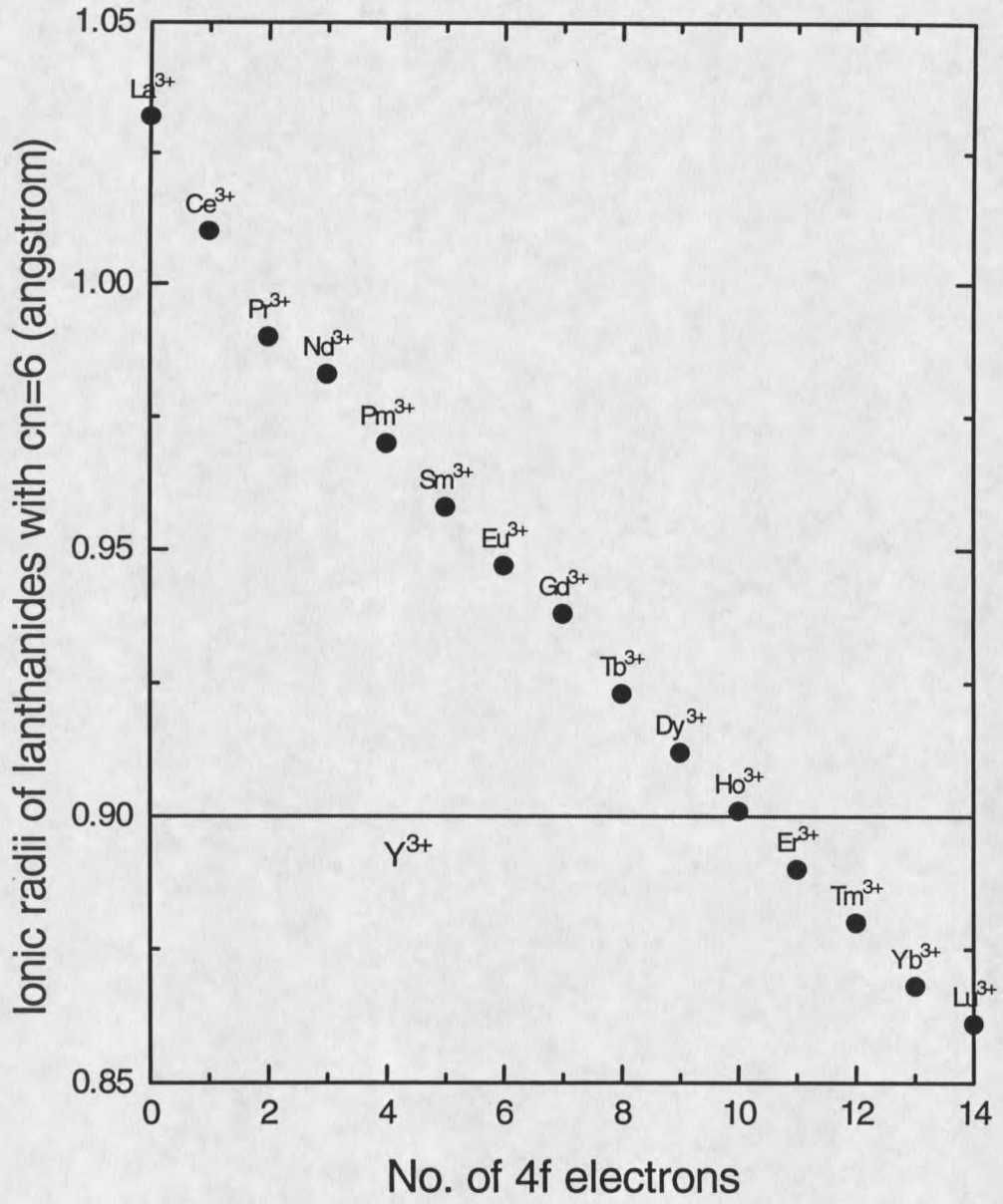

Figure 28. Ionic radii of the lanthanides with coordination number = 6.

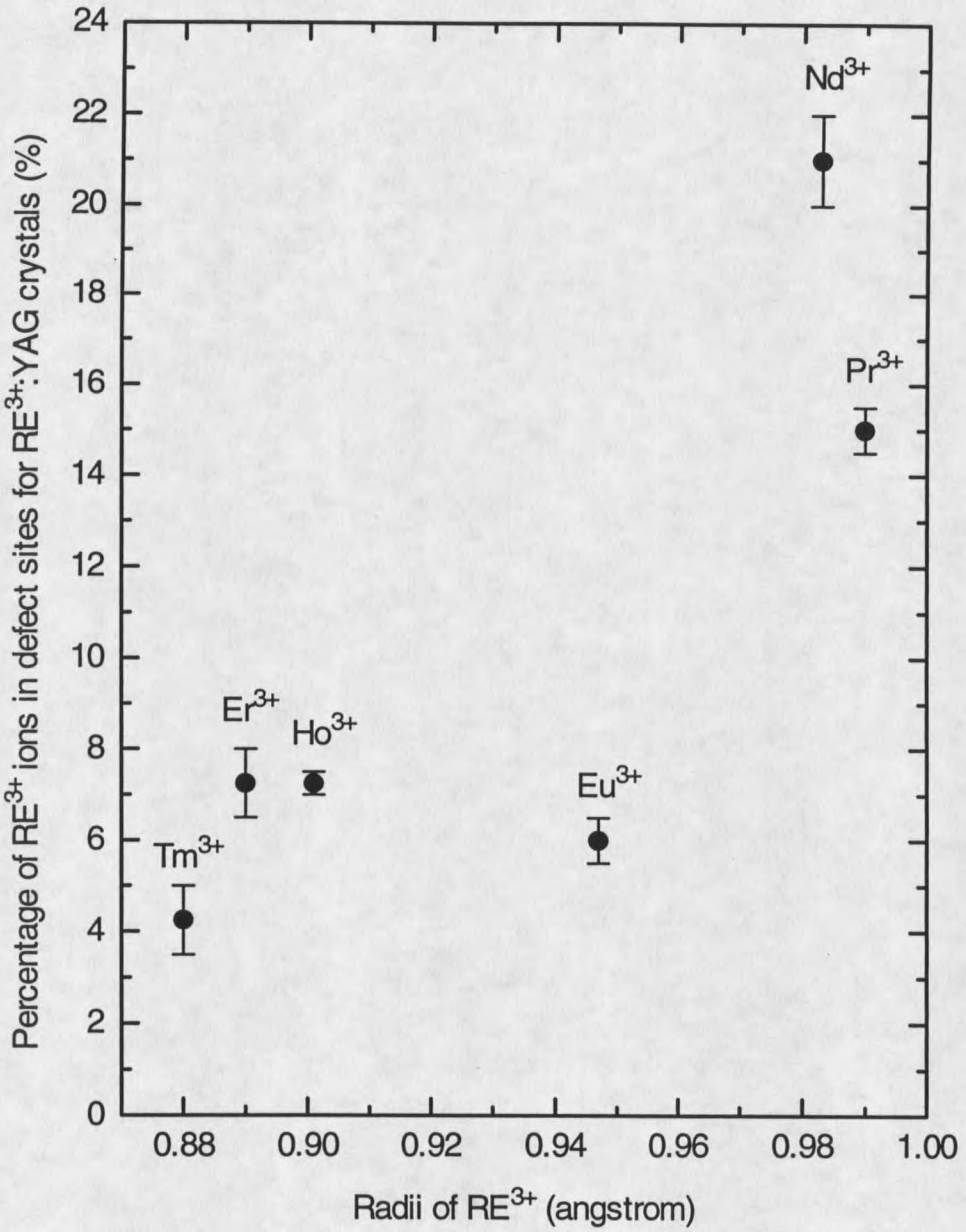

Figure 29. Percentage of R^{3+} ions in defect sites for R^{3+}:$Y_3Al_5O_{12}$ crystals.

References for Chapter 2

1. Y. Sun, Ph. D Thesis (Montana State University, Bozeman, 1993).

2. F. N. Hooge, J. Chem. Phys. **45**, 4504 (1966).

3. J. P. van der Ziel, M. D. Sturge and L. G. van Uitert, Phys. Rev. Letters **27**, 508 (1971).

4. R. M. Shelby., A. C. Tropper, R. T. Harley and R. M. Macfarlane, Opt. Lett. **8**, 304 (1983).

5. O. L. Malta, E. Antic-Fidancev, M. Lemaitre-Blaise, J. Dexpert-Ghys and B. Piriow, Chem. Phys. Letters **129**, 557 (1986).

6. E. Antic-Fidancev, M. Lemaitre-Blaise and P. Caro, Inorg. Chim. Acta **139**, 281 (1987).

7. V. V. Ryabchenkow, Soviet Phys. Cryst. **32**, 855 (1987).

8. J. B. Gruber, M. E. Hills, R. M. Macfarlane, C. A. Morrison and G. A. Turner, Chem. Phys. **134**, 241 (1989).

9. W. Wolinski, R. Wolski, M. Malinowski and Z. Mierczyk 1992 Proc. 10th Int. Congr. On Laser Optoelectronics (Munich, June 1991) ed. W. Waidelich (Berlin: Springer) p 611.

10. J. Ganem, W. M. Dennis and W. M. Yen, J. Lumin. **54**, 79 (1992).

11. S. K. Gayen, B. Q. Xie, and Y. M Cheung, Phys. Rev. B **45**, 20 (1992).

12. E. Antic-Fidancev, M. Lemaitre-Blaise, P. Porcher and J. C. Krupa, Eur. J. Solid State Inorg. Chem. **28**, 81 (1991).

13. E. Antic-Fidancev, M. Lemaitre-Blaise, J. C. Krupa and P. Caro, Czech. J. Phys. B **38**, 1268 (1988).

14. E. Antic-Fidancev, M. Lemaitre-Blaise, and P. Porcher, J. Alloys and Compounds, **207 & 208**, 90 (1994).

15. M. Malinowski, P. Szczepanski, W. Wolinski, R. Wolski and Z. Frukacz, J. Phys.: Condens. Matter **5**, 6469 (1993).

16. J. A. Koningstein and J. E. Geusic, Phys. Rev. **136**, A 711 (1964).

17. L. A. Riseberg and W. C. Holton, J. Appl. Phys., **43** 1876 (1972).

18. R. K. Watts and W. C. Holton, Journal of Applied Physics, **45**, 873 (1974).

19. Larry D. Merkle and Richard C, Powell, Phys. Rev. B. **20**, 75 (1979).

20. D. P. Devor and L. G. DeShazer, Opt. Commun. **46**, 97 (1983).

21. D. P. Devor, R. C. Pastor, and L. G. DeShazer, J. Chem. Phys. **81**, 4104 (1984).

22. V. Lupei, A. Lupei, S. Georgescu and C. Ionescu, Opt. Commun. **60**, 59 (1986).

23. Dao-hong Hua, Zeng-fu Song, Shu-kun Wang, and Zu-xiu Rong, J. Chem. Phys. **89**, 5398 (1988).

24. Zeng-fu Song, Dao-hong Hua, Shu-kun Wang, and You-xi gui, J. Chem. Phys. **89**, 5404 (1988).

25. V. Lupei, A. Lupei, S. Georgescu and W. M. Yen, J. Appl. Phys. **66**, 3792 (1989).

26. D. P. Devor, L. G. DeShazer, Member, IEEE, and R. C. Pastor. IEEE J. Quantum Electron. **25**, 1863 (1989).

27. Stanley R. Rotman, Appl. Phys. Lett. **54**, 2053 (1989).

28. Toomas H. Allik, Clyde A. Morrison, John B. Gruber and Milan R. Kokta, Phys. Rev. B **41**, 21 (1990).

29. V. Lupei, A. Lupei, S. Georgescu, and I. Ursu, Appl. Phys. Lett. **59** (8), 905 (1991).

30. V. Lupei, A. Lupei, C. Tiseanu, S. Georgescu, C. Stoicescu, and P. M. Nanau, Phys. Rev. B **51**, 8 (1995).

31. P. Grunberg, Z. Physik, **225**, 376 (1969).

32. J. B. Gruber, M. E. Hills, M. P. Nadler, M. R. Kokta, and C. A. Morrison, Chem. Phys. **113**, 175 (1987).

33. S. B. Stevens, C. A. Morrison, and M. C. Seltzer, J. Appl. Phys. **70**, 948 (1991).

34. M. Malinowski, R. Wolski, and Z. Luczynski, J. Appl. Spectros. **62**, 840 (1995).

35. H. Yusa, T. Yagi, and H. Arashi, J. Appl. Phys. **75**, 1463 (1994).

36. J. Liu, and Y. K. Vohra, Appl. Phys. Lett. **64**, 3386 (1994).

37. M. Asano, and J. A. Koningstein, Chem. Phys. **42**, 369 (1979).

38. K. Binnemans and C. Gorller-Walrand, J. Chem. Soc. **92**, 2487 (1996).

39. G. M. Zverev, G. Ya. Kolodnyi and A. M. Onischenko, Sov. Phys. JETP **30**, 435 (1970).

40. L. F. Johnson, J. E. Geusic and L. G. Van Uitert, Appl. Phys. Lett. **8**, 200 (1966).

41. M. Kh. Ashurov, Yu. K. Voron'ko, E. V. Zharikov, A. A. Kaminskii, V. V. Osiko, A. A. Sobol',M. I. Timoshechkin, V. A. Federov and A. A. Shabaltal, Inorg. Mater. (USSR) **15**, 979 (1979).

42. N.P. Barnes, and D.J. Gettemy, Appl. Opt. **29**, 404 (1990).

43. S.W. Henderson, and C.P. Hale, Appl. Opt. 29, 1716 (1990).

44. Y. Shimony, Y. Kalisky, and H. Lotem, J. Appl. Opt. **68**, 2966 (1990).

45. G. Armagan, A.M. Buoncristiani, and B. Di Bartolo, J. Lumin. **48/49**, 171 (1991).

46. V. A. French, and R. C. Powell, Opt. Lett. **16**, 666 (1991).

47. S.R. Bowman, M.J. Winnings, and S. Searles, IEEE J. Quantum Electron. **27**, 1129 (1991).

48. S.R. Bowman, M.J. Winings, and R.C.Y. Auyeung, IEEE J. Quantum Electron. **27**, 2142 (1991).

49. R.C. Stoneman, and L. Esterowitz, Opt. Lett. **17**, 736 (1992).

50. K. H. Kim, Y. S. Choi, and N. P. Barnes, Appl. Opt. **32**, 2066 (1993).

51. P. J. Morris, W. Luthy, and H. P. Weber, Opt. Commun. **104**, 97 (1993).

52. H. Nakajima, T. Yokozawa, and N. Djeu, Japanese J. Appl. Phys. **33**, L1010 (1994).

53. T. Yokozawa, H. Nakajima, and H. Hara, Rev. Scientific Instrum. **66**, 1153 (1995),

54. C.D. Nabors, J. Ochoa, and G.W. Turner, IEEE J. Quantum Electron. **31**, 1603 (1995).

55. M. Falconieri, A. Lanzi, and G. Salvetti, Appl. Phys. B **62**, 537 (1996).

56. M. Tonelli, M. Falconieri, and A. Toncelli, Opt. Commun. **129**, 62 (1996).

57. J. A. Koningstein and J. E. Geusic, Phys. Rev. **136**, A726 (1964).

58. Yu. K. Voronko and A. A. Sobol, Phys. Stat. Sol. **27**, 257 (1975).

59. T. T. Basiev, E. V. Kharikov, V. I. Zhekov, T. M. Murina, V. V. Osiko, A. M. Prokhorov, B. P. Starikov, M. I. Timoshechkin, and I. A. Shcherbakov, Sov. J. Quantum Electron. **6**, 796 (1976).

60. A. A. Kaminskii, T. I. Butaeva, V. a. Fedorov, Kh. S. Bagdasarov and A. G. Petrosyan, Phys. Stat. Sol. (a) **39**, 541 (1977).

61. N. I. Agladze, M. N. Popova, E. A. Vinogradov, T. M. Murina and V. I. Zhekov, Opt. Commun. **65**, 351 (1988).

62. I. Ursu, A. Lupei, S. Georgescu, V. Lupei, A. M. Prokhorov, V. I. Zhekov, T. M. Murina and M. I. Studenikin, Opt. Commun. **72**, 209 (1989).

63. V. I. Zhekov, T. M. Murina, A. V. Popov, and A. M. Prokhorov, Sov. Tech. Phys. Lett. **16**, 625 (1990).

64. A. Lupei, V. Lupei, S. Georgescu, and I. Ursu, V. I. Zhekov, T. M. Murina, and A. M. Prokhorov, Phys. Rev. B. **41**, 10923 (1990).

65. S. Georgescu, V. Lupei, A. Lupei, V. I. Zhekov, T. M. Murina, and M. I. Studenikin, Opt. Commun. **81**, 186 (1991).

66. R. Spring and W. Lüthy, J. Appl. Phys. **69**, 581 (1991).

67. R. M. Macfarlane, T. L. Harris, Y. Sun, R. L. Cone, and R. W. Equall, Opt. Lett. to be published. (1997).

68. P. J. M. Suni, and S. W. Henderson, Opt. Lett. **16**, 817 (1991).

69. J. F. Pinto, L. Esterowitz, and G. H. Rosenblatt, Opt. Lett. **17**, 731 (1992).

70. P. Peterson, A. Gavrielides, and M. P. Sharma, Appl. Phys. B **61**, 195 (1995).

71. J. B. Gruber, M. E. Hills, R. M. Macfarlane, C. A. Morrison, G. A. Turner, C. J. Quarles, C. J. Kintz, and L. Esterowitx, Phys. Rev. B **40**, 9464 (1989).

72. A. Lupei, C. Tiseanu, and V. Lupei, Phys. Rev. B **47**, 14084 (1993).

73. R. D. Shannon, Acta. Crystallogr. **32**, 751 (1976).

74. S. Geller, G. P. Espinosa, L. D. Fullmer, and P. B. Crandall, Mater. Res. Bull. **7**, 1219 (1972).

CHAPTER 3

HYPERFINE INTERACTIONS AND NONLINEAR SPECTROSCOPY

Introduction

Many techniques with increased spectral resolution have been introduced with the goal of providing a much better understanding of the hyperfine interaction. Techniques such as spectral holeburning, optically detected nuclear magnetic resonance (ODNMR), Raman heterodyne detection of NMR, optical free induction decay (FID), photon echo, and photon echo nuclear double resonance (PENDOR) can overcome the resolution limit imposed by inhomogeneous broadening. The various methods have provided complementary pieces of information, allowing a relatively detailed picture of the hyperfine structure and dynamics of the Pr^{3+}:$Y_3Al_5O_{12}$ system to be put together. For details, readers are referred to the review article by Macfarlane and Shelby.[1]

Nonlinear spectroscopy can be used to determine the nuclear quadrupole hyperfine interaction parameters and principal axis orientations. It provides symmetry information for defects in the rare earth doped garnet crystals, and that helps in characterizing the structure of these defect sites.

We start this chapter with the study of the intrinsic site of Pr^{3+}:$Y_3Al_5O_{12}$. Several nonlinear spectroscopic techniques were applied to the intrinsic site first and then to one

of the defect sites. The Pr^{3+} ion is easier to study than Nd^{3+} but the similarity of its ionic radius and defect behavior make any results relevant to the popular Nd^{3+}:$Y_3Al_5O_{12}$ laser system.

Experimental Results for Pr^{3+} in the Intrinsic Site of $Y_3Al_5O_{12}$

Introduction

Considerable attention has been given to the study of the hyperfine interaction of Pr^{3+} ions in single crystals.[1] Because the $^3H_4 \leftrightarrow {}^1D_2$ transition of Pr^{3+} ion lies within the tuning range of Rhodamine 6G dye lasers, it has been studied in great detail. In addition, the Pr^{3+} ion in the intrinsic site of $Y_3Al_5O_{12}$ has an enhanced ground state nuclear magnetic moment due to the coupling of the ground state singlet with other low-lying electronic states (within tens of wavenumbers), so it is very sensitive to the magnetic field. A low-field Helmholtz coil (<500 G) can be used to observe the Zeeman splittings of the hyperfine levels. Zeeman experiments with full angular rotation have been carried out previously on Pr^{3+}:$YAlO_3$[7,4] and Pr^{3+}:LaF_3[9,10,4] These studies yielded information on the principal axis direction of the pseudo quadrupole interaction. Most of the interest in the $Y_3Al_5O_{12}$ crystal has been in its application as a host material for rare-earth ion lasers and more recently for optical memory. Despite all of the technological applications and investigations of rare-earth-doped $Y_3Al_5O_{12}$, only a few papers have been published about the pseudo quadrupole interaction.[11-13] This is probably due to the complexity of the crystal structure of $Y_3Al_5O_{12}$, where the Y ions of interest occupy six magnetically

inequivalent sites with D_2 symmetry. When rare earth ions are substituted into these sites, the Zeeman spectrum can be very difficult to resolve. Nevertheless, due to the importance of $Y_3Al_5O_{12}$, it is still worth investigating the Zeeman spectrum of rare earth ion doped $Y_3Al_5O_{12}$ crystals.

Various double-resonance techniques have proved to be powerful probes of hyperfine structure. These include electron-nuclear double resonance (ENDOR),[14] photon-echo-nuclear double resonance (PENDOR),[15,16] and optically detected nuclear magnetic resonance (ODNMR).[17,7] Mlynek et al.[2] introduced Raman heterodyne spectroscopy to the study of the hyperfine interaction of Pr^{3+}:$YAlO_3$. Raman heterodyne spectroscopy is a sensitive optical-RF double-resonance technique and has wide applicability.[5] Because of its high sensitivity, it can be used to obtain a large amount of data in a short period of time. In this work, we used Raman heterodyne detection of NMR and ODNMR in the investigation of the hyperfine interaction of the ground $^3H_4(1)$ state and the excited $^1D_2(1)$ state of Pr^{3+} in $Y_3Al_5O_{12}$.

We start with a brief review of the theory of the Pr^{3+} hyperfine interaction and of Raman heterodyne detection of NMR. The experimental apparatus and experimental results will then be presented. The results are analyzed and the hyperfine parameters and principal axes of Pr^{3+} hyperfine interaction are determined from the angle-dependent Raman heterodyne data.

Theory

The ^{141}Pr nucleus, the only natural isotope, has spin I = 5/2. For all singlet states of a non-Kramers ion, the average electronic angular momentum is zero and the first-order magnetic hyperfine interaction $\vec{I} \circ \vec{J}$ vanishes. The pseudo-quadruple hyperfine interaction expressed in terms of an effective spin 5/2 contains two contributions: (1) the interaction between the electric field gradient and the quadrupole moment of the nucleus; (2) the second-order hyperfine interaction between the nuclear magnetic moment and the magnetic field produced by the electrons of the ion. The latter is called the pseudo-quadrupole interaction because its effective-spin Hamiltonian has the same form as the electric quadrupole interaction. Thus the effective-spin Hamiltonian in zero applied magnetic field can be written with respect to the principal axes of the ground state as,

$$H = P\left[I_z^{\,2} - \frac{1}{3}I(I+1) + \frac{1}{3}\eta\left(I_x^{\,2} - I_y^{\,2}\right)\right] \tag{3.1}$$

where P is the pseudo-quadrupole interaction constant and η is the asymmetry factor. The principal axes (x, y, z) are determined by the crystal field and electronic charge distribution and are therefore dependent on the electronic state and may be constrained by the symmetry of the ion site. Since the hyperfine Hamiltonian is quadratic in the I_i's (i=x,y,z), the (2I + 1)-fold degeneracy is partially lifted for half-integral spin I, giving a series of doublets. For I=5/2, there are three doubly degenerate hyperfine levels described by linear combinations of $m_I = \pm 5/2, \pm 3/2$, and $\pm 1/2$ at zero magnetic field. The mixing between the levels depends on the asymmetry factor η.

In a magnetic field H_0, the effective spin Hamiltonian is:[18]

$$H = P\left[I_z^2 - \frac{1}{3}I(I+1) + \frac{1}{3}\eta\left(I_x^2 - I_y^2\right)\right] - \hbar H_0\left(\gamma_x I_x \sin\theta\cos\varphi + \gamma_y I_y \sin\theta\sin\varphi + \gamma_z I_z \cos\theta\right) \tag{3.2}$$

The enhanced nuclear gyromagnetic ratio is given by

$$\gamma_i = \left(g_N\beta_N + 2g\beta\Lambda_{ii}\right)/\hbar, i = x, y, z \tag{3.3}$$

$$\text{with } \Lambda_{ii} = \sum_{n\neq 0}\frac{A_j\left|\langle 0|J_i|n\rangle\right|^2}{\varepsilon_n - \varepsilon_0}, \tag{3.4}$$

where ε_n is the energy of electronic level $|n\rangle$ and A_j is the hyperfine constant for the given J state. The static external magnetic field H_0 is along (θ,φ) in spherical coordinates with respect to the principal axes of the psudoquadrupole tensor.

Raman Heterodyne Detection of NMR

Raman heterodyne detection involves the simultaneous excitation of a three-level quantum system by two coherent fields, as shown in Figure 30. An RF field of frequency ω excites a NMR transition $|1\rangle \rightarrow |2\rangle$, and an optical field of frequency Ω resonantly excites an electronic transition $|2\rangle \rightarrow |3\rangle$. The resonant Raman process generates a coherent anti-Stokes optical field at the sum frequency $\Omega' = \Omega + \omega$. This in turn beats with the driving field Ω, producing a difference frequency $\omega = |\Omega' - \Omega|$ in the light field. By observing this beating signal, nuclear magnetic resonances, and spin coherent-transients or continuous-wave signals, can be monitored with great sensitivity.

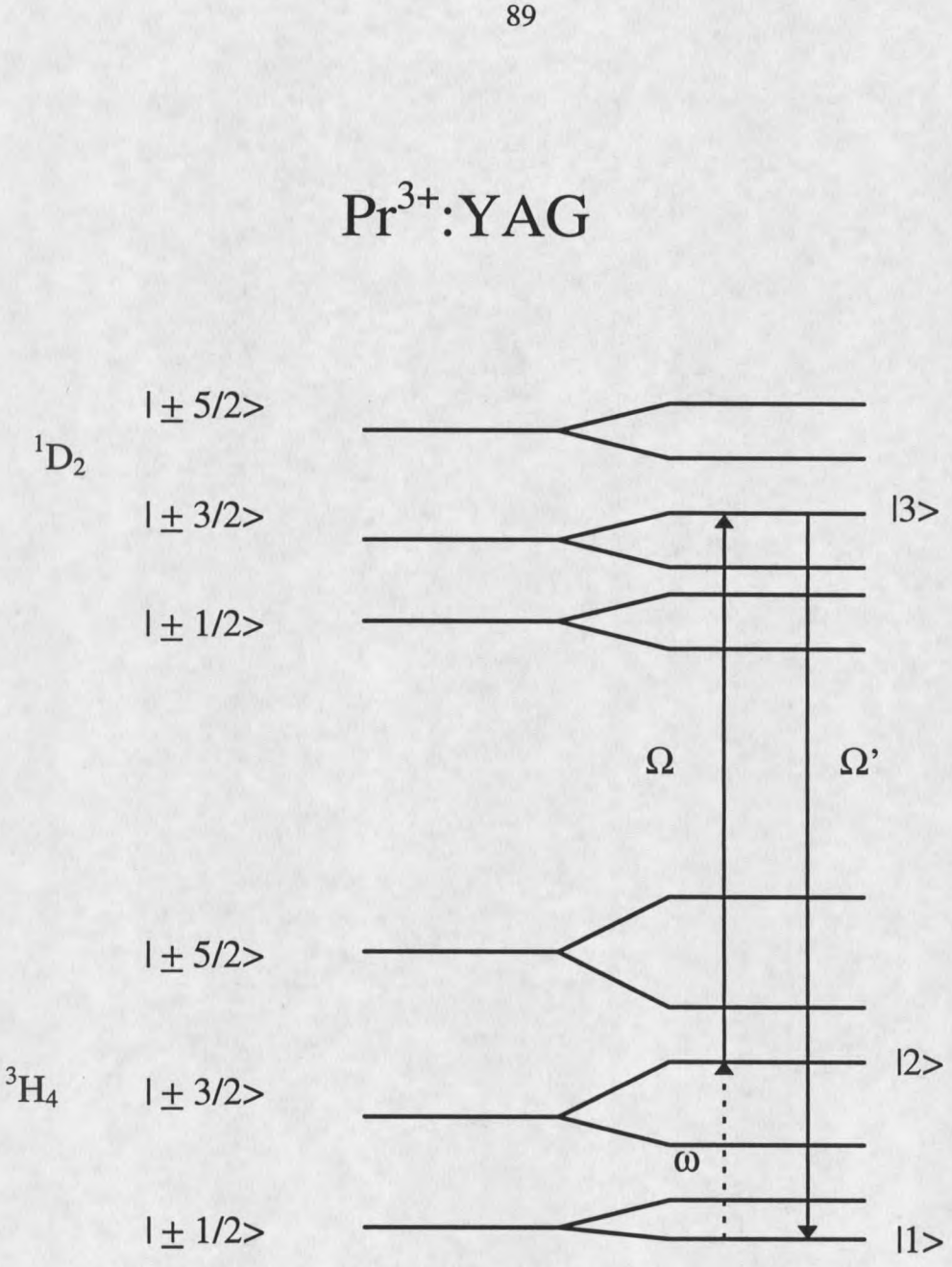

Figure 30. Zeeman-split hyperfine level diagram for the Pr^{3+} $^3H_4(1) \leftrightarrow {}^1D_2(1)$ transition of $Pr^{3+}:Y_3Al_5O_{12}$, showing the coherent Raman process (not to scale). The dashed line shows the RF field ω for driving the $|1\rangle \rightarrow |2\rangle$ transition. The solid line Ω represents the optical driving field for the $|2\rangle \rightarrow |3\rangle$ transition. The solid line Ω′ is the anti-Stokes field.

The Raman heterodyne signal[2, 19]

$$S \propto \mu_{12}\mu_{23}\mu_{31} \tag{3.5}$$

depends on the triple product of the three matrix elements μ_{ij} connecting these states. Since each matrix element is phase dependent and appears linearly, interference can occur between different sites.[3-6]

Assuming the quantum system of Figure 30, appropriate for the Pr^{3+} ion, the Raman heterodyne beat signal S for the three states indicated obeys the relationship,[19]

$$S = a|E_0|^2|H_{RF}|\left(\rho_{22}^0 - \rho_{11}^0\right) \mathrm{Re}\left[w\left[\frac{\overline{\Delta}_E}{\sigma_E}\right]\right] \times \mathrm{Im}\left[w\left[\frac{\overline{\Delta}_H + i\gamma_{12}}{\sigma_H}\right] e^{i\omega_H t}\right] \tag{3.6}$$

with $a = \dfrac{\pi^2 k_E L N}{\sigma_E \sigma_H \hbar^2}\mu_{12}\mu_{23}\mu_{31}$.

Here, ω_H is the RF or heterodyne beat frequency,

$\mu_{12}\mu_{23}\mu_{31}$ is the transition-matrix product,

E_0 and H_{rf} are the optical and RF field amplitudes,

k_E is the optical wave vector,

L is the sample length, N is the impurity-ion number density,

$\rho_{22}^0 - \rho_{11}^0$ is the ground-state population difference,

$\overline{\Delta}_E$ and $\overline{\Delta}_H$ are the laser frequency and RF offsets from the center frequencies of the inhomogeneously broadened transitions $|2\rangle \rightarrow |3\rangle$ and $|1\rangle \rightarrow |2\rangle$, respectively,

σ_E and σ_H are the corresponding inhomogeneous linewidths, and γ_{12} is the RF homogeneous linewidth,

and the line-shape function is

$$w(z) = \frac{i}{\pi}\int_{-\infty}^{+\infty}\frac{e^{-t^2}dt}{z-t}, \quad Imz > 0.$$

When Raman heterodyne detection of NMR had insufficient intensity, such as in a zero field measurement, ODNMR was applied as a complementary method. The detection scheme used the change of fluorescence signal to monitor RF resonances. When the laser (linewidth of ~ 2 MHz) was resonant with the transition, only one of the three doubly degenerate ground-state hyperfine levels was pumped. The upper level might relax back to the other two unpumped ground hyperfine levels. Due to slow spin-lattice relaxation (several seconds), excess population builds up for the two unpumped ground hyperfine levels, causing fewer ions to participate in the pumping cycle and hence produce less fluorescence i.e. a spectral hole. When a RF field was tuned to resonance with a hyperfine splitting, it tended to equalize the population between hyperfine levels, causing the fluorescence intensity to increase.

Apparatus and Experiment

The top portion of Figure 31 shows a schematic diagram of the apparatus for Raman heterodyne detection of the hyperfine transitions as a function of magnetic field amplitude and direction.

A 0.018% Pr^{3+}:$Y_3Al_5O_{12}$ crystal was cut to 1 x 3 x 5 mm with (111), $(1\bar{1}0)$ and $(11\bar{2})$ faces, and was mounted on a holder that could rotate the crystal around a horizontal axis. In this work, the rotation axis was chosen to be the $(1\bar{1}0)$ direction. The static magnetic field was arranged to be perpendicular to this axis. Consequently, as the

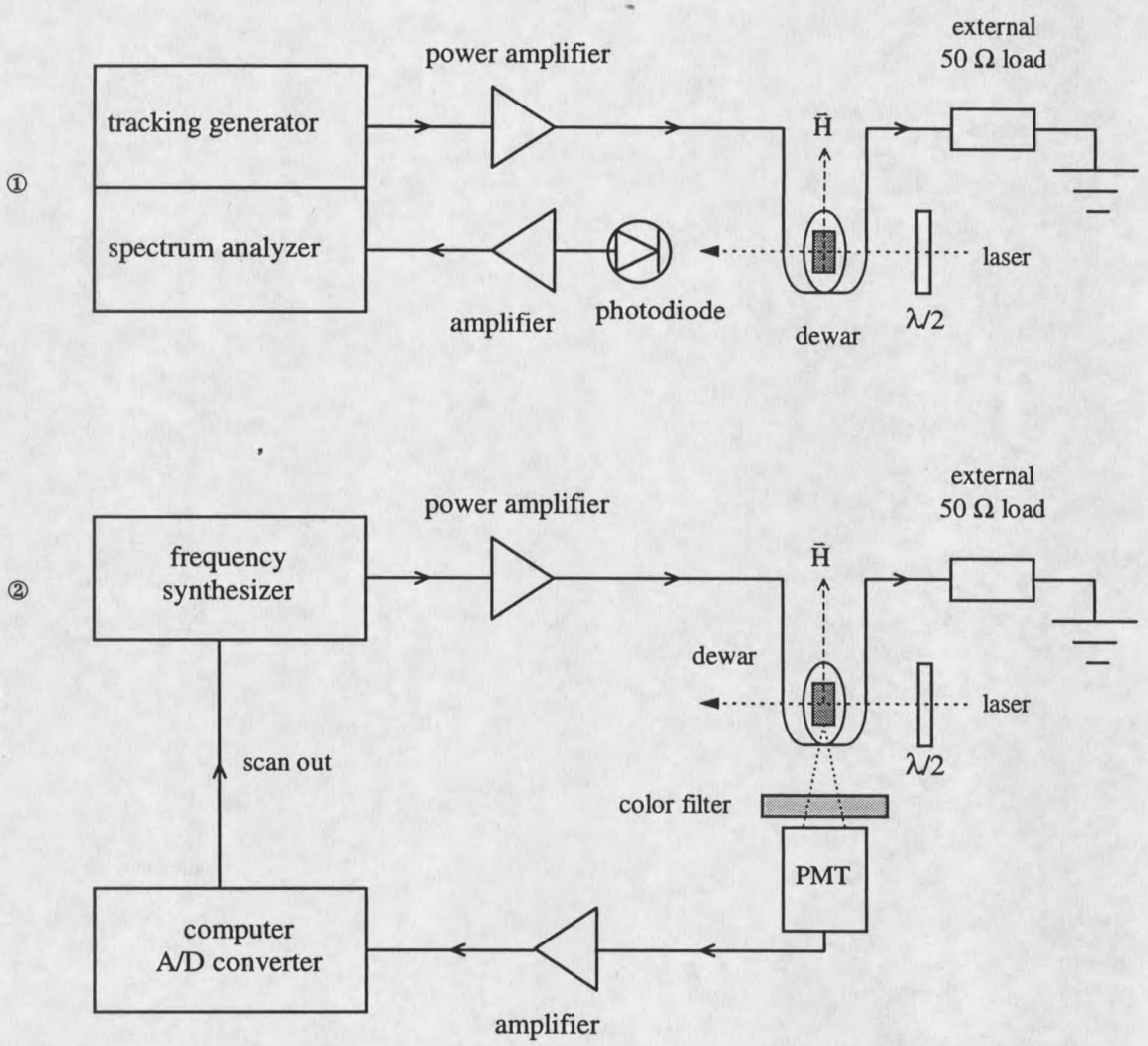

Figure 31. Schematic of apparatus ① is for the Raman heterodyne detection of NMR and ② is for the ODNMR.

crystal rotated, the magnetic field rotated in a plane containing the (001), (111) and (110) directions.

The sample rotating system included a protractor, a long rod, a vertical axis gear, a 90 degree gear to translate the vertical rotation to horizontal rotation, and a shaft to hold the sample. To test the precision of the angle reading, a sheet polarizer was mounted vertically on the shaft. A laser beam was sent through a Glan-laser polarizing prism to purify its polarization. It was then sent through the polarizer mounted on the shaft and detected by a photo diode. The laser intensity was plotted via the rotation angle read from the protractor on top of the sample holder. The data shown in Figure 32 were fit to a sine squared function. The angular resetting accuracy and the backlash of the rotating system were determined to be 0.5 and 1.1 degree, respectively.

The **H** vector of the RF field was along $(1\,\bar{1}\,0)$ and was produced by a 5-mm radius, 8-turn solenoid of magnet wire around the crystal. Four capacitors of 20 pF were used between alternating turns of the solenoid and the ground of the coax to produce a reasonably uniform transmission line for the frequency range 0-100 MHz.

The Coherent 599-21 dye laser had a ~2 MHz linewidth and ~ 20 mW output power. The laser beam passed through the crystal along the $(1\,\bar{1}\,0)$ direction which was perpendicular to the static magnetic field and parallel to the **H** vector of the RF field. A $\lambda/2$ waveplate was used to rotate the polarization of the laser to enhance signals for specific sites.

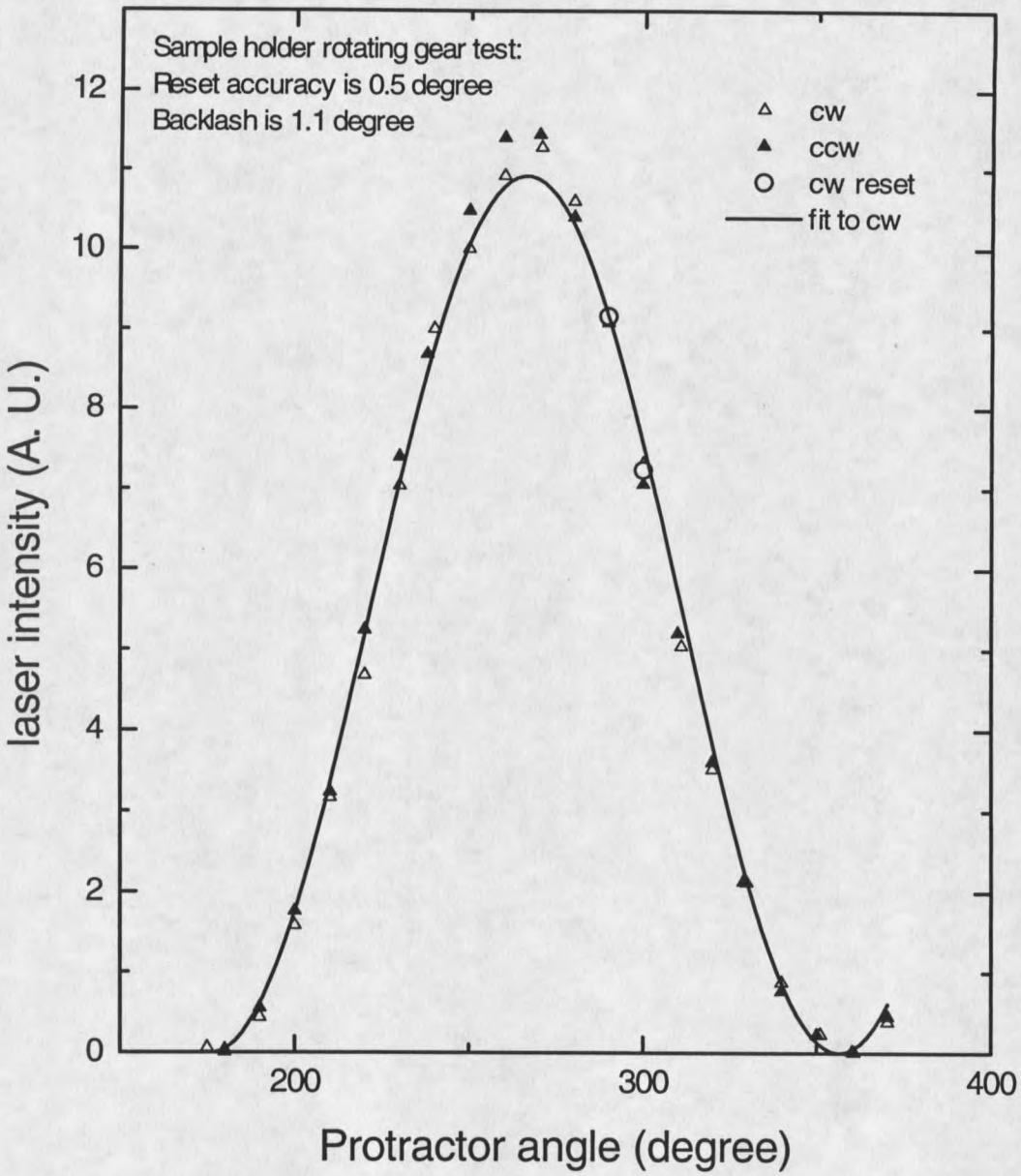

Figure 32. The transmitted laser beam intensity versus the protractor angle θ. The open triangles mark the data when the protractor was rotated clockwise. The solid triangles mark the data when the protractor was rotated counter-clockwise. The circles were data when the protractor was reset clockwise. The clockwise data was fit to $a*\sin^2(\theta-b)$.

The laser beam was focused on the crystal with a 33 cm lens, and the beam transmitted through the crystal was focused on an EG&G FND-100 photodiode. The RF field was generated by a Hewlett-Packard 8444A tracking generator. The ac component of the detected laser transmission signal was amplified and processed by a Hewlett-Packard 8554B spectrum analyzer set to a bandwidth of 10 kHz and swept synchronously with the tracking generator. A suitable sweep speed (10MHz/second) was chosen, as too fast a speed tended to broaden the lines.

The apparatus for the conventional ODNMR experiment is shown at the bottom of Figure 31 ②. The RF signal was generated with a computer-controlled PTS500 synthesizer. As the RF frequency was scanned, the fluorescence signal of the $^1D_2 \rightarrow {}^3H_5$ and $^1D_2 \rightarrow {}^3H_6$ transitions was detected by a PMT. A color filter was used to block the scattered laser light. The fluorescence signal was sent to an analog-to-digital converter and averaged.

The 0.018% Pr^{3+}:$Y_3Al_5O_{12}$ crystal was immersed in liquid helium at temperatures down to 1.4K. The laser was tuned to 609.587 nm, corresponding to the transition between the lowest Stark levels of the $^1D_2(1)$ and $^3H_4(1)$ electronic states of Pr^{3+}:$Y_3Al_5O_{12}$. The inhomogeneous linewidth was determined from absorption measurements to be 1.7 cm^{-1}. At 1.4 K the population is initially all in the lowest Stark level $^3H_4(1)$, the nearest excited Stark level $^3H_4(2)$ being 18 cm^{-1} away.

For the measurement of hyperfine structure versus the direction of an applied magnetic field, Raman heterodyne detection of NMR was used. Since the $|\pm 1/2\rangle \leftrightarrow |\pm 3/2\rangle$ transitions are narrower than other transitions, the majority of the

spectra were taken in this region for better resolution. The $|-3/2\rangle \leftrightarrow |+3/2\rangle$ transitions were also observed, but in a much lower frequency region (0-10 MHz).

Analysis

At zero magnetic field, since the interference between different sites caused the Raman heterodyne signal to vanish, the ODNMR technique was used. The ODNMR spectrum of Figure 33 shows ground state hyperfine splittings of 33.33 (FWHM = 0.37), 41.86(0.71), and 75.22(0.72) MHz, where the sum of the first two equals the third as expected. When the RF field resonates with the splittings, the fluorescence intensity increases by a factor of 1.3 to 2.5. The hyperfine parameters P and η are determined by substituting trial values of these parameters in the ground-state Hamiltonians of Eq. (3.1) for the splittings measured. The values P = 11.36 MHz and η = 0.733 agree with Shelby et al.[11]

From Eq. (3.1), the composition of the eigenstates $|\pm m\rangle = \Sigma\, a_{im}\, \psi_i$ with i and m = $\pm$1/2, $\pm$3/2, $\pm$5/2 could be calculated, where ψ_i's are the pure nuclear spin projection states. The $|\pm m\rangle$ eigenstates are not pure but labeled by dominant pure component. The results are shown in Table 14.

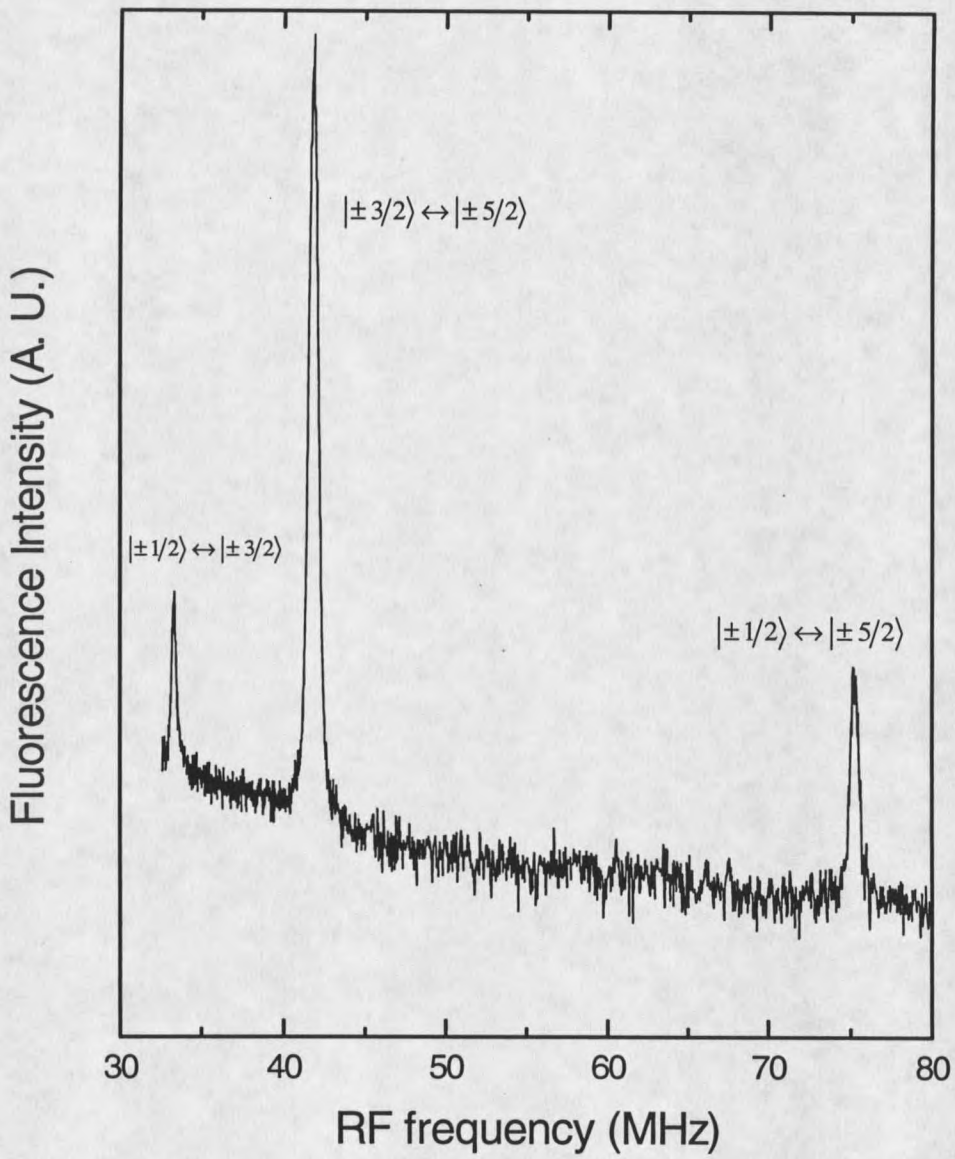

Figure 33. Optically-detected NMR spectrum of the $^3H_4(1) \leftrightarrow {}^1D_2(1)$ transition in a $Pr^{3+}:Y_3Al_5O_{12}$ crystal showing the $|\pm 1/2\rangle \leftrightarrow |\pm 3/2\rangle$, $|\pm 3/2\rangle \leftrightarrow |\pm 5/2\rangle$ and $|\pm 1/2\rangle \leftrightarrow |\pm 5/2\rangle$ resonances at zero magnetic field.

The crystal structure of yttrium aluminum garnet ($Y_3Al_5O_{12}$) has been described in Chapter 1. The Pr^{3+} ions that substitute for Y^{3+} ions on the dodecahedral sites experience a crystal field of D_2 symmetry, and the coordinates of local sites are shown in Figure 2. There are six magnetically inequivalent orientations of these sites in the crystal. For one of the Pr^{3+} ion sites, the local x, y, and z axes are oriented along the (110), $(1\bar{1}0)$, and (001) crystal axes with the z axis coinciding with the (001) axis by convention. The axes for other sites are obtained by using (Ia3d) space group symmetry appropriate to the garnet structure.

Table 14. Compositions of eigenstates $|\pm m\rangle = \Sigma\, a_{im}\, \psi_i$ with i and m = $\pm 1/2$, $\pm 3/2$, $\pm 5/2$

eigenstates	$\|+5/2\rangle$	$\|+3/2\rangle$	$\|+1/2\rangle$	$\|-1/2\rangle$	$\|-3/2\rangle$	$\|-5/2\rangle$
eigenvalues(MHz)	38.86	-2.72	-36.14	-36.14	-2.72	38.86
$\psi_{\|+5/2\rangle}$	0.99054	0	-0.11009	0	-0.0819	0
$\psi_{\|+3/2\rangle}$	0	0.92387	0	-0.38119	0	0.03402
$\psi_{\|+1/2\rangle}$	0.13293	0	0.91792	0	0.37384	0
$\psi_{\|-1/2\rangle}$	0	0.37384	0	0.91792	0	0.13293
$\psi_{\|-3/2\rangle}$	0.03402	0	-0.38119	0	0.92387	0
$\psi_{\|-5/2\rangle}$	0	-0.0819	0	-0.11009	0	0.99054

In general, the nuclear axes for ground ($^3H_4$) and excited ($^1D_2$) electronic states may be incongruent and the gyromagnetic ratios $\gamma_{x,y,z}$ and the quadrupole parameters P and η for these two electronic states may differ also. For the intrinsic site, however, the

local D_2 symmetry should constrain the three principal nuclear axes to the three C_2 symmetry axes (110), $(1\bar{1}0)$, and (001).

For Pr^{3+} (I = 5/2), the matrices of the nuclear spin projection operators in the basis of the pure ψ_i basis states are

$$I_x = \frac{1}{2}\begin{bmatrix} 0 & \sqrt{5} & 0 & 0 & 0 & 0 \\ \sqrt{5} & 0 & \sqrt{8} & 0 & 0 & 0 \\ 0 & \sqrt{8} & 0 & 3 & 0 & 0 \\ 0 & 0 & 3 & 0 & \sqrt{8} & 0 \\ 0 & 0 & 0 & \sqrt{8} & 0 & \sqrt{5} \\ 0 & 0 & 0 & 0 & \sqrt{5} & 0 \end{bmatrix},$$

$$I_y = \frac{1}{2i}\begin{bmatrix} 0 & -\sqrt{5} & 0 & 0 & 0 & 0 \\ \sqrt{5} & 0 & -\sqrt{8} & 0 & 0 & 0 \\ 0 & \sqrt{8} & 0 & -3 & 0 & 0 \\ 0 & 0 & 3 & 0 & -\sqrt{8} & 0 \\ 0 & 0 & 0 & \sqrt{8} & 0 & -\sqrt{5} \\ 0 & 0 & 0 & 0 & \sqrt{5} & 0 \end{bmatrix},$$

$$I_z = \frac{1}{2}\begin{bmatrix} 5 & 0 & 0 & 0 & 0 & 0 \\ 0 & 3 & 0 & 0 & 0 & 0 \\ 0 & 0 & 1 & 0 & 0 & 0 \\ 0 & 0 & 0 & -1 & 0 & 0 \\ 0 & 0 & 0 & 0 & -3 & 0 \\ 0 & 0 & 0 & 0 & 0 & -5 \end{bmatrix}$$

Introducing a variable $k = -1/2\ \hbar H_0$, and $k_x = k\gamma_x \sin\theta\cos\varphi$, $k_y = k\gamma_y \sin\theta\sin\varphi$, and $k_z = k\gamma_z \cos\theta$, the hyperfine and Zeeman Hamiltonian of Eq. (3.2) could be written in the matrix form:[20, 21]

$$\mathrm{Re}\,H=\begin{bmatrix} \frac{10}{3}P+5k_z & \sqrt{5}k_x & \frac{\sqrt{10}}{3}P\eta & 0 & 0 & 0 \\ \sqrt{5}k_x & -\frac{2}{3}P+3k_z & 2\sqrt{2}k_x & \sqrt{2}P\eta & 0 & 0 \\ \frac{\sqrt{10}}{3}P\eta & 2\sqrt{2}k_x & -\frac{8}{3}P+k_z & 3k_x & \sqrt{2}P\eta & 0 \\ 0 & \sqrt{2}P\eta & 3k_x & -\frac{8}{3}P-k_z & 2\sqrt{2}k_x & \frac{\sqrt{10}}{3}P\eta \\ 0 & 0 & \sqrt{2}P\eta & 2\sqrt{2}k_x & -\frac{2}{3}P-3k_z & \sqrt{5}k_x \\ 0 & 0 & 0 & \frac{\sqrt{10}}{3}P\eta & \sqrt{5}k_x & \frac{10}{3}P-5k_z \end{bmatrix},$$

and

$$\mathrm{Im}\,H=\begin{bmatrix} 0 & \sqrt{5}k_y & 0 & 0 & 0 & 0 \\ -\sqrt{5}k_y & 0 & 2\sqrt{2}k_y & 0 & 0 & 0 \\ 0 & -2\sqrt{2}k_y & 0 & 3k_y & 0 & 0 \\ 0 & 0 & -3k_y & 0 & 2\sqrt{2}k_y & 0 \\ 0 & 0 & 0 & -2\sqrt{2}k_y & 0 & \sqrt{5}k_y \\ 0 & 0 & 0 & 0 & -\sqrt{5}k_y & 0 \end{bmatrix} \tag{3.7}$$

From Figure 2, if the static magnetic field is constrained to the plane containing (001) and (111), the number of inequivalent sites are reduced from 6 to 4. Sites 3 and 4 are equivalent to sites 5 and 6 respectively. Figure 34 shows the angle dependent Raman heterodyne NMR spectra of $|\pm 1/2\rangle \leftrightarrow |\pm 3/2\rangle$ transitions in a 190 G magnetic field. Generally there are 16 lines because each site has 4 lines for the $|\pm 1/2\rangle \leftrightarrow |\pm 3/2\rangle$ transitions. There are some extra weak lines that are due to the upper $|\pm 3/2\rangle \leftrightarrow |\pm 5/2\rangle$ transitions. When the magnetic field is in the (111) direction,

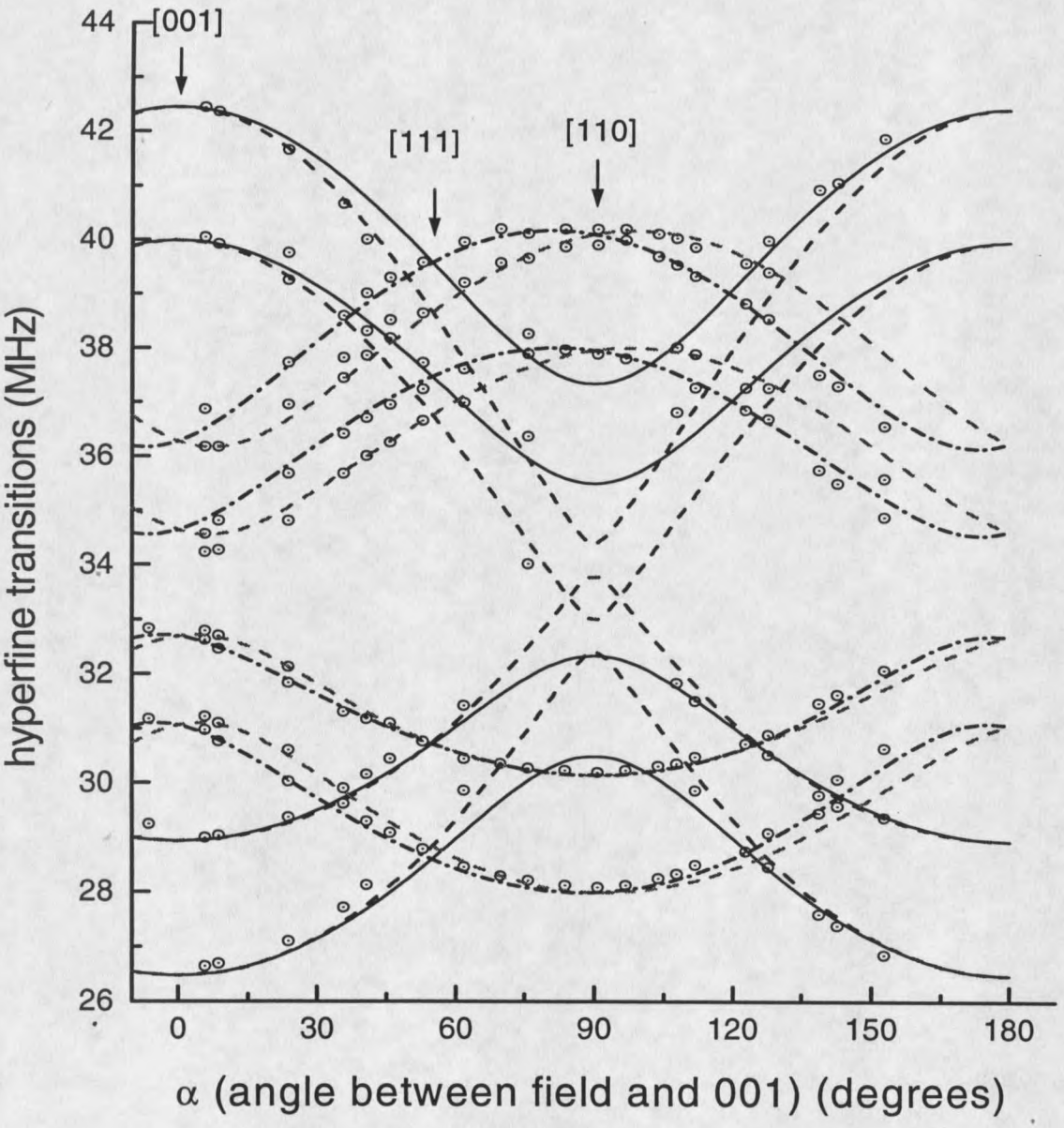

Figure 34. Zeeman splittings are mapped for the $|\pm 1/2\rangle \leftrightarrow |\pm 3/2\rangle$ transitions in a 190-G magnetic field rotating in a plane perpendicular to $(1\,\bar{1}\,0)$. α is the angle between the magnetic field and (001).

the number of inequivalent sites is further reduced to two, resulting in eight lines total. A nonlinear fitting program was used to diagonalize the Hamiltonian of Eq. (3.7) and search for the least-squares fit to the data. The fitting results for the gyromagnetic ratios are $\hbar\gamma_x$ = 13±0.3, $\hbar\gamma_y$ = 1.6±0.2, and $\hbar\gamma_z$ = 30.3±0.6 kHz/Gauss. The data were also fitted with a program that determines the directions of the principal axes. The fitted results for these directions are within ± 2 degrees of the expected directions constrained by D_2 symmetry.

Comparing values of the gyromagnetic ratio with those of Pr^{3+} ions in other hosts ($YAlO_3$, LaF_3), these values are relatively large. Table 15 shows the comparison between these three crystals. Authors in Ref. 4 did not measure the energy of the $^3H_4(2)$ electronic state.

Table 15. The gyromagnetic ratios for Pr^{3+} doped crystals.

	$Y_3Al_5O_{12}$	$YAlO_3$[7,8]	$YAlO_3$[4]	LaF_3[10]
$\hbar\gamma_x$ (kHz/G)	13	3.881	2.43	4.98
$\hbar\gamma_y$ (kHz/G)	1.6	2.50	2.43	2.53
$\hbar\gamma_z$ (kHz/G)	30.3	11.648	11.785	10.16
$^3H_4(2)$ cm^{-1}	19	51[7,8]		57[22]

We also observed some transitions in the 2 - 10 MHz region with a 140-Gauss field. Figure 35 shows the angle dependent NMR spectra using Raman heterodyne detection. These transitions converge to 0 MHz as the magnetic field decreases to zero. They are assigned to the $|-3/2\rangle \leftrightarrow |+3/2\rangle$ transitions. From the zero field eigenfunction composition of Table 14, we know these transitions are allowed by the selection rules

$\Delta m=0, \pm 1$. There are four lines due to the four inequivalent sites. The $|-1/2\rangle \leftrightarrow |+1/2\rangle$ transitions are also possible and are calculated to be < 1 MHz for the 140-Gauss field. Due to the laser frequency jitter (~ 2 MHz), they were not observed.

For these $|-3/2\rangle \leftrightarrow |+3/2\rangle$ transitions, a simple perturbation analysis could be used provided that the magnetic field was not too large. It provided a preliminary method to obtain an insight into the experimental data before complex matrix fitting was used to obtain a more precise solution. Treating the Zeeman interaction as a perturbation on the zero field quadrupoler eigenstates, the $|\pm 3/2\rangle$ levels were considered as isolated degenerate states. The Zeeman-induced frequency shift of these two levels was

$$\omega_{\pm 3/2} = \pm (\hbar H_0/2)[(\gamma_z A\cos\theta)^2 + (\gamma_y B\sin\theta\sin\varphi)^2 + (\gamma_x C\sin\theta\cos\varphi)^2]^{1/2} \qquad (3.8)$$

where $A = 5a_{5/2}^2 + a_{1/2}^2 - 3a_{3/2}^2$,

$B = 2(5)^{1/2} a_{5/2} a_{3/2} - 4(2)^{1/2} a_{1/2} a_{3/2} + 3 a_{1/2}^2$, and

$C = 2(5)^{1/2} a_{5/2} a_{3/2} + 4(2)^{1/2} a_{1/2} a_{3/2} + 3 a_{1/2}^2$

The a_i coefficients were calculated in Table 14, with $a_{5/2} = -0.0819$, $a_{3/2} = 0.92387$, $a_{-1/2} = 0.37384$, for $|\pm 3/2\rangle$ levels, giving

$A = -2.3873$, $B = -1.8729$, $C = 2.0347$

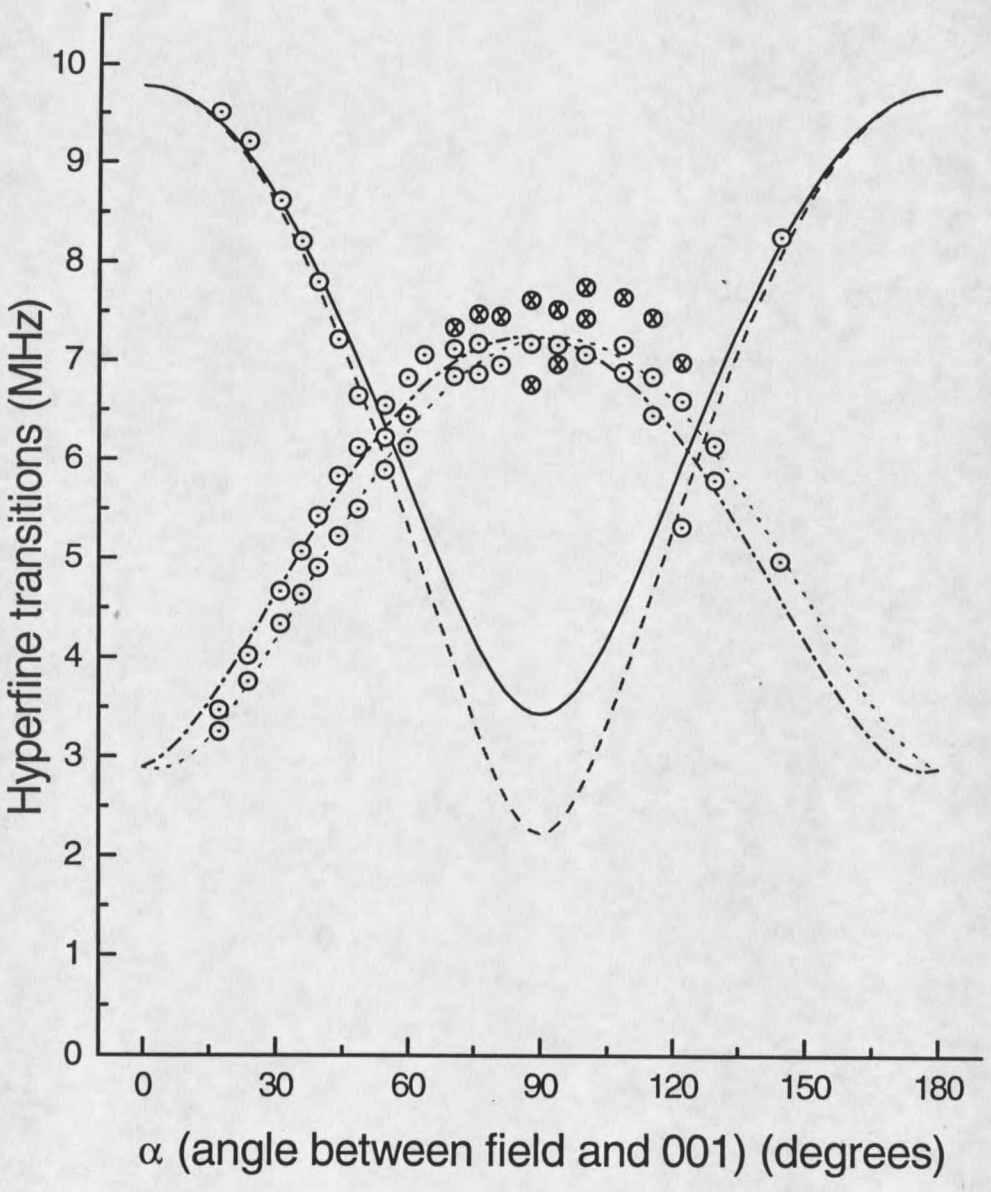

Figure 35. Zeeman splittings are mapped for the $|-3/2\rangle \leftrightarrow |+3/2\rangle$ transitions in a 140-G magnetic field rotating in a plane perpendicular to $(1\,\bar{1}\,0)$. α is the angle between the magnetic field and (001). The data points with crossed centers for angles between 60° and 120° are assigned to excited state hyperfine splittings.

Fitting Eq. (3.8) to detail in Figure 35, we have $\hbar\gamma_x$ = 11.5 kHz/G; $\hbar\gamma_y$ = 3.3 kHz/G; $\hbar\gamma_z$ = 30.0 kHz/G. Due to the vanishing signal for site 1 and 2 when the magnetic field is near perpendicular to the (001) axis, the $\hbar\gamma_x$ and $\hbar\gamma_y$ are not well determined. The value $\hbar\gamma_z$ is consistent with the experimental result for the $|\pm 1/2\rangle \leftrightarrow |\pm 3/2\rangle$ transitions.

As discussed earlier, the axes for these fits are very close to the expected directions constrained by D_2 symmetry. In Figure 35, there are some extra points with crossed centers for angles between 60° and 120° whose intensities are much weaker than the |-3/2>↔|+3/2> transitions. These transitions converge to nonzero energy values as the magnetic field decreases to zero so they could not arise from the transition considered here; they were assigned to an excited state hyperfine splitting as discussed in the next section. Raman heterodyne ODNMR signal intensities also showed very strong dependence on the laser polarization and RF field direcion. This can be attributed to the fact that the Raman heterodyne signal expressed in Eq. (3.5) depends on the triple product of the three polarization dependent matrix elements connecting the ground state hyperfine states and the $^1D_2$ excited state.

Excited State

The hyperfine splittings of $^1D_2(1)$ in a magnetic field were observed with Raman heterodyne ODNMR. When the magnetic field was along (110) and the laser polarization was perpendicular to (110), the signal was the strongest. There was no signal at zero field due to site interference. The zero field hyperfine splittings were obtained by extrapolating the Zeeman spectrum to zero magnetic field. The splittings of 6.41 and 8.32 MHz agree

with the values 6.49 and 8.29 MHz reported by Shelby et al.[11] However these values do not agree with the 3.42 and 5.96 MHz reported by Kim et al.[13] obtained from their measured photon echo modulation pattern. That photon echo modulation data[13] indicated that the site symmetry of the Pr^{3+} ions was lowered to C_2 from the D_2 symmetry of Y^{3+} ions. The excited state hyperfine splittings they measured are also different from the values measured here using Raman heterodyne ODNMR and by Shelby et al.[11] using holeburning and Quantum beat FID (Free Induction Decay). The result obtained here do not support the suggested lowering of symmetry to C_2, but rather are consistent with D_2 symmetry.

The fluorescence lifetime of the $^1D_2(1)$ level was found to be $T_1 = 230$ μs. The dephasing time $T_2 = 20$ μs was measured from photon echo decay with 1 μs laser pulses. This value agrees with the value measured by Shelby et al.[11] Some important optical and hyperfine parameters of the $^3H_4(1) \leftrightarrow {}^1D_2(1)$ transition of $Pr^{3+}:Y_3Al_5O_{12}$ at 1.4 K are listed in Table 16.

Conclusion

The hyperfine interaction of the intrinsic site of Pr^{3+} ($4f^2$) in $Y_3Al_5O_{12}$ crystals was studied using optically-detected nuclear-magnetic-resonance (ODNMR) in both fluorescence and Raman heterodyne detection schemes. The hyperfine interaction parameters and principal axes of the ground quadrupole tensor for the $^3H_4(1)$ state were determined from measurements in a 190 G magnetic field. Six magnetically inequivalent sites were observed for magnetic fields constrained to the (110) plane. The measured

NMR frequencies are functions of the angles between the principal axes and magnetic field. The frequency vs. angle spectra show that the principal axes of the quadrupole interaction are parallel to the axes of local D_2 symmetry of the Y^{3+} ions which confirms with high precision that Pr^{3+} ions substitute for Y^{3+} ions and preserve the D_2 symmetry. Using a pseudoquadrupole spin Hamiltonian, a satisfactory fit was obtained with gyromagnetic ratios $\hbar\,\gamma_x = 13$, $\hbar\,\gamma_y = 1.6$, and $\hbar\,\gamma_z = 30.3$ kHz/G.

Table 16. Optical and hyperfine parameters of the $^3H_4(1) \leftrightarrow {}^1D_2(1)$ transition of Pr^{3+}:$Y_3Al_5O_{12}$ at 1.4 K. Parameters noted by * were also measured by Shelby et al.[11]

λ_0	609.587 nanometer in air (16400.0 cm^{-1})	
Γ_{inh}	1.3 cm^{-1}	
T_1	230 μs	
T_2	20 μs*	
osc. str. (f)	$\approx 10^{-6}$	
	$^3H_4$	$^1D_2$
(±1/2 ↔ ±3/2) (MHz)	33.33*	6.41*
(±3/2 ↔ ±5/2) (MHz)	41.86*	8.32*
P (MHz)	11.36	2.24
η	0.733	0.696
γ_x (kHz/gauss)	13	—
γ_y (kHz/gauss)	1.6	—
γ_z (kHz/gauss)	30.3	—

The expected Raman heterodyne signal interference between different sites was observed as a variation in the signal intensity with the laser polarization direction. This interference is closely related to the site orientation. Full improvement of the fitting program should include the signal intensity as a variable.

Experimental Results for Pr^{3+} in Defect Sites of $Y_3Al_5O_{12}$

Introduction

The full angle-dependent ODNMR data can be exploited to extract information on the hyperfine interaction parameters. The local D_2 symmetry of the intrinsic site was confirmed in the analysis of the previous section. In this section, one defect site will be studied with the same method except that there is no predetermined structural information for these defect sites. We want to find the directions of the defect principal axes in the crystal coordinates. From this information and other results, a hypothesis for the origin of these defects will be presented.

In conventional spectroscopy, the selection rules and group theory have been used to extract structural information on the crystal from the polarized absorption and fluorescence data. In the $Y_3Al_5O_{12}$ system, because of its isotropic structure, only a few papers have been published on polarized spectroscopy of the intrinsic site for $Tb:Y_3Al_5O_{12}$[23] $Ho:Y_3Al_5O_{12}$[24] and $Eu:Y_3Al_5O_{12}$[25,26]. From the polarized spectroscopy, R^{3+} ions in the intrinsic site were found to have a local D_2 symmetry as expected. For the defects, due to their lower local symmetry, normally C_1, it becomes almost impossible to obtain a polarized spectrum.

Full angle-dependent ODNMR directly probes the local structural information of the defect sites with high sensitivity and resolution. This method was introduced in this laboratory by Sun[20] for the $EuVO_4$ system. This thesis will study the $Y_3Al_5O_{12}$ system, which has a different crystal symmetry and more magnetically inequivalent sites than

$EuVO_4$. We will start by describing the defect structure and its relation with the $Y_3Al_5O_{12}$ structure.

Symmetry Considerations

$Y_3Al_5O_{12}$ has cubic symmetry O_h^{10} (Ia3d) as explained in Chapter 1. When Pr^{3+} ions are doped into the crystal, the majority of Pr^{3+} ions go to the intrinsic Y^{3+} site which has D_2 local symmetry. Some of them go to defect sites which most probably have C_1 local symmetry. In order to describe the orientation of the defect site coordinates relative to the crystal coordinates, Euler angles α, β, and γ are used. The quantum mechanical convention for defining these angles was used previously[20] and is followed here. Starting from a defect coordinate system overlapped with the crystal coordinates (x, y, z), the defect site axis is rotated by angle α around the z-axis. After that, the defect site axis is rotated by angle β around its new (intermediate) y-axis to orient its z-axis pointing at the final direction. Finally, the defect axis is rotated by angle γ around the defect z-axis to reach the final position. All the angles are measured counter-clockwise while looking down the axes towards the origin.

For a C_1 symmetry local site, the O_h^{10} transformations of the host lattice generate 48 sites with different orientations as illustrated by the stereographic projection[28] in Figure 36. The stereographic diagram projects the z directions of these 48 defect sites onto a sphere. The dots represent 24 of these sites projected onto the top hemisphere, and the circles are the other 24 sites projected onto the bottom hemisphere. Two faces of a cube are shown in Figure 37 and Figure 38 with 8 sites per face. Figure 37 and Figure 38

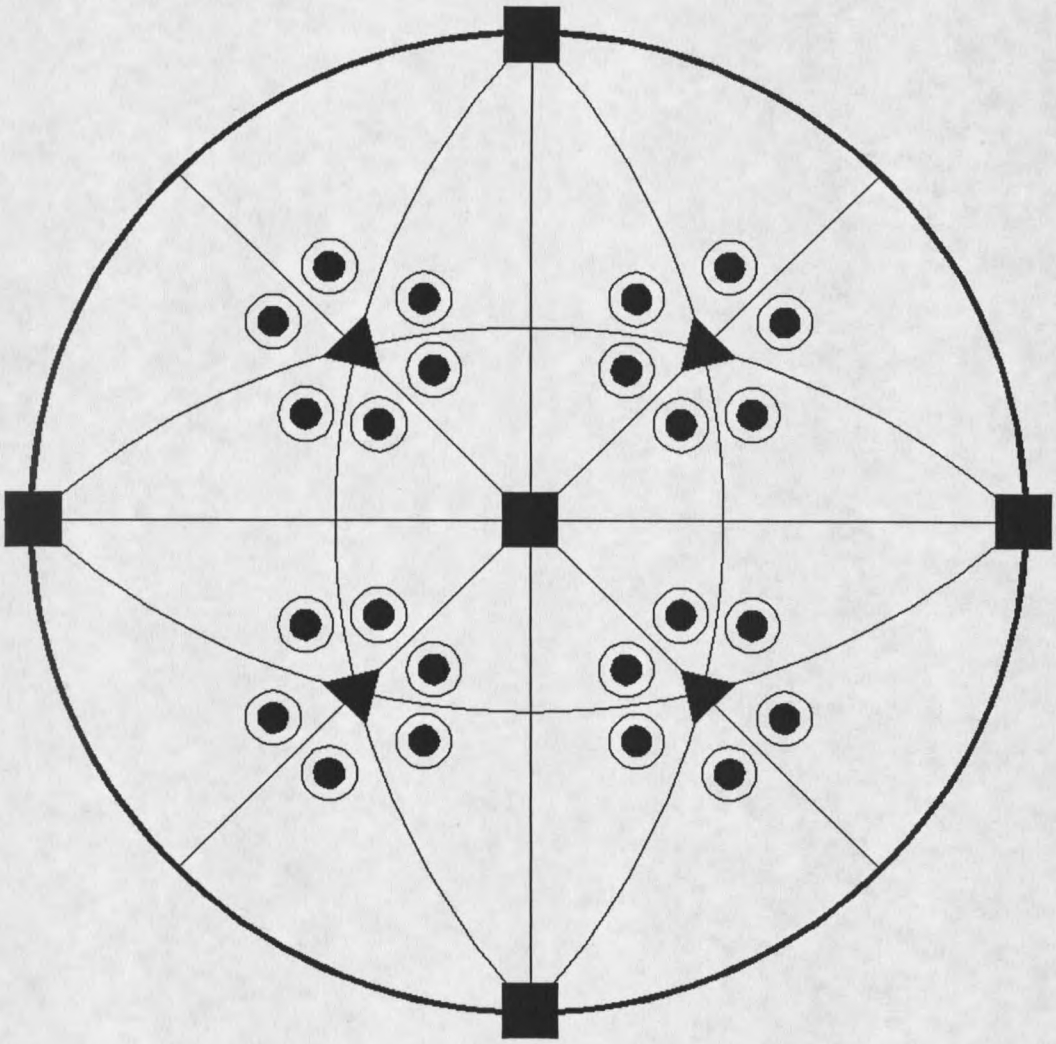

Figure 36. Stereographic projection[28] of the O_h[10] group. There are 48 elements in this group. They include C_4, C_3, and C_2 rotations and mirror reflections. Twenty-four elements are projected onto the top hemisphere as the dots, and the other 24 elements are projected onto the bottom hemisphere as the circles.

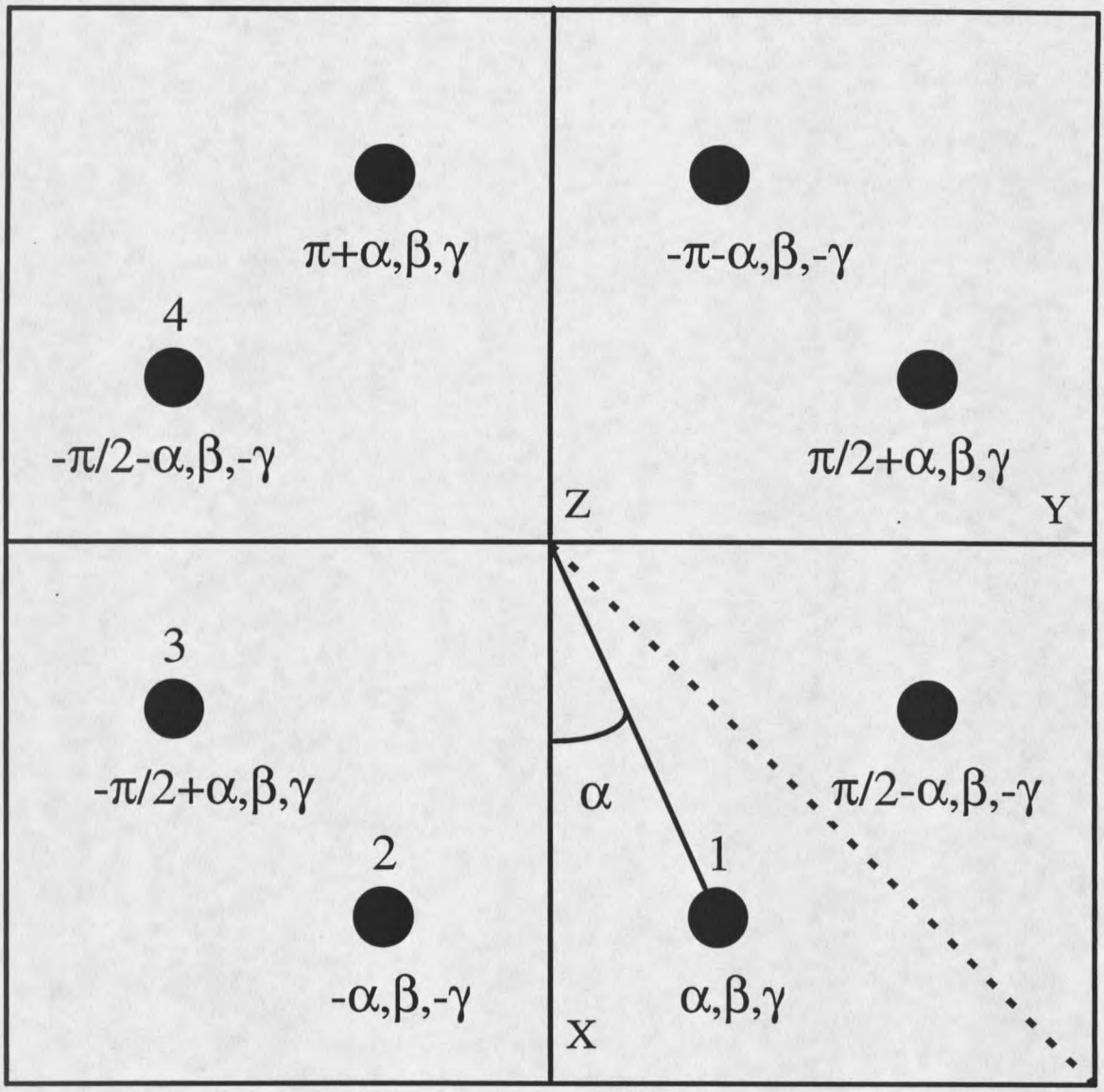

Figure 37. The site orientations of defect sites on surface Z (001). The magnetic field rotates from (001) to (111) to (110) as indicated by the dash line. The un-numbered sites are mirror images of the numbered ones relative the mirror plane (1-10). They are equivalent in our experimental geometry.

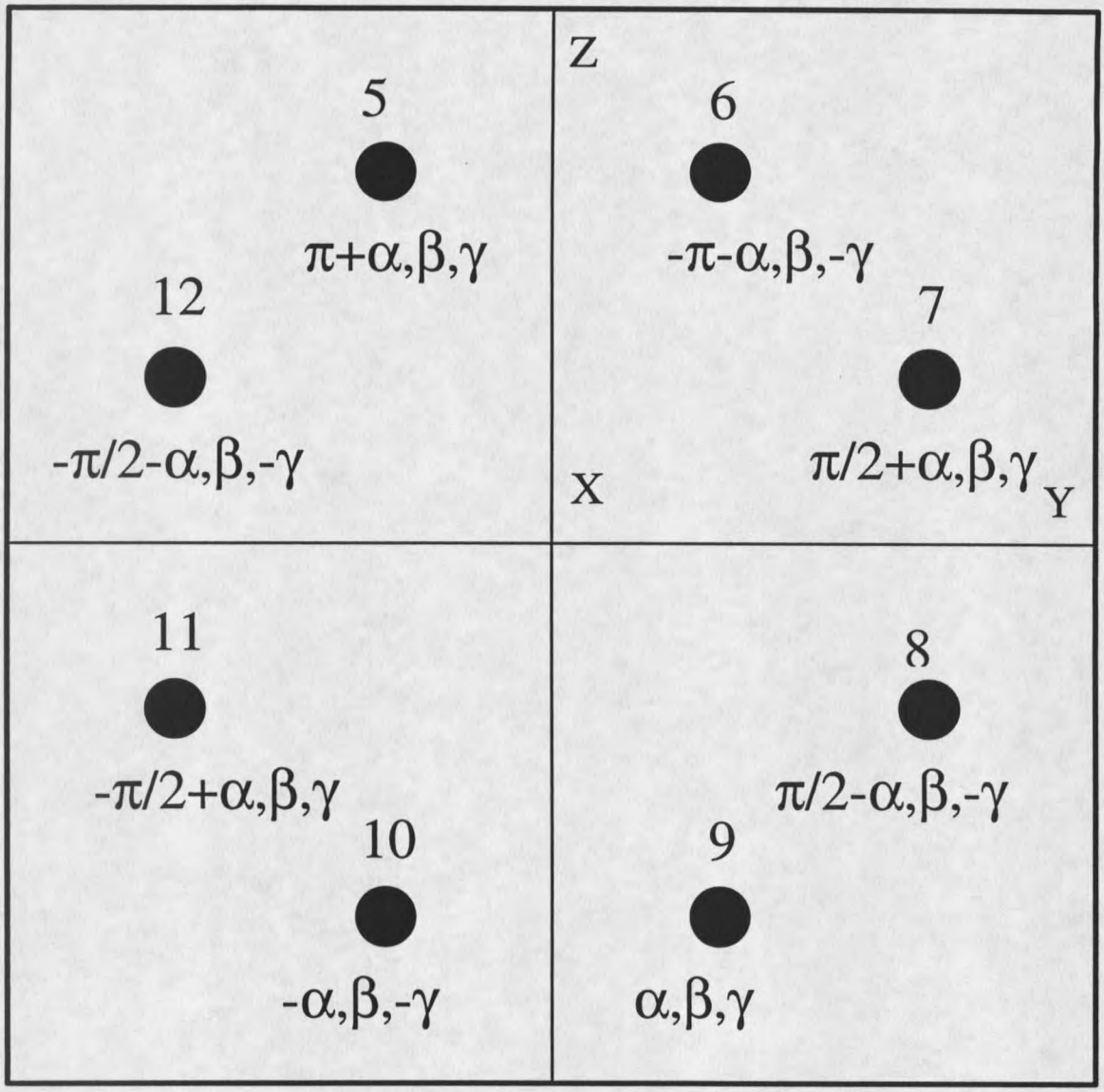

Figure 38. The site orientations of defect sites on surface X (100). The orientations on X (100) are expressed relative to a new coordinate system which is formed by rotating the original coordinates 90° counter-clockwise about the Y (010) axis.

do not represent the physical locations of the defect sites but their relative orientations. There is an inversion symmetry in the crystal so only 24 magnetically-inequivalent sites exist in an arbitrary magnetic field.

A magnetic field applied in an arbitrary direction in the crystal will have a different orientation in each of the magnetically-inequivalent sites, but the orientations are related by simple transformations. A cube has 6 faces i.e. X (100), Y (010), Z (001), X′ ($\bar{1}$00), Y′ (0$\bar{1}$0), and Z′ (00$\bar{1}$). X, Y, and Z are equivalent to X′ ,Y′, and Z′ by inversion symmetry. X, Y, and Z are related by a 3-fold rotation about (111) direction.

The arbitrary defect site orientations on Z (001) shown in Figure 37 are: (α,β,γ), $(-\alpha,\beta,-\gamma)$, $(-\pi/2+\alpha,\beta,\gamma)$, $(-\pi/2-\alpha,\beta,-\gamma)$, $(\pi+\alpha,\beta,\gamma)$, $(-\pi-\alpha,\beta,-\gamma)$, $(\pi/2+\alpha,\beta,\gamma)$, and $(\pi/2-\alpha,\beta,-\gamma)$, which are connected by C_4 and vertical mirror reflections. The orientations containing $-\gamma$ are obtained by mirror reflections.

The site orientations on the X (100) face shown in Figure 38 can be obtained from the Z (001) face by a 3-fold rotation around the (111) direction. But the expressions for the site orientation relative to the original crystal coordinates are very complex. The orientations on X (100) can be re-expressed relative to a new coordinate system which is formed by rotating the original coordinates 90° counter-clockwise along the Y (010) axis. The expressions in this new coordinate system are then the same as those on the Z (001) face in the old coordinate system.

The experiments were carried out with the magnetic field rotating from (001) to (111) to (110). Since this is a mirror plane, the 24 magnetically-inequivalent sites are

reduced to 12 sites as labeled on Figure 37 and Figure 38. If the experiments were done so that the magnetic field rotated from (001) to (101) to (100), which is another mirror plane, the number of magnetically-inequivalent sites would also be 12.

When the magnetic field is along (001), only three inequivalent sites will be seen; namely (1, 2, 3, and 4), (5, 6, 9, and 10), and (7, 8, 11, and 12). With the magnetic field rotated to be along (111), four inequivalent sites will be seen, namely (1, 6, and 7), (2, 5, and 8), (3, 9, and 12) and (4, 10, and 11). When the magnetic field is along (110), six inequivalent sites will be seen, they are (1 and 4), (2 and 3), (5 and 12), (6 and 9), (7 and 8), and (11 and 12).

The nonlinear fitting program written by Sun[20] for a D_{4h} crystal was modified for the $Y_3Al_5O_{12}$ crystal with cubic symmetry with assistance from Sun. This program will fit the angle-dependent ODNMR data as a function of magnetic field angles. There are six fitting parameters, namely, three gyromagnetic ratios γ_x, γ_y, γ_z and three angles (α,β,γ) for local site principal axis orientation.

To use the fitting program, we have to assign the measured frequencies to the correct sites and to the correct transitions. It is not always obvious how to assign the data to particular sites and if the assignment is wrong the fitting result is wrong too. This is trial and error. A fitting program was written to automatically make every possible curve assignment in turn for the fitting. Generally one or two curves were selected to start with. Good fits may be found for some of the assignments after 8 hours of continuous fitting for pairs of curves. A personal computer with a 200 MHz Pentium processor was used in the computation. The assignments related by the O_h[10] transformations are equivalent and

give the same fit. Because there are crossings between those curves and there are sections where signal intensity decreases to zero, it is difficult to identify a whole curve without doubt. Portions of curves were used in the fitting when necessary.

A plotting program was written for a PC to plot the angle dependent spectra generated with a drawing program. The drawing program uses the parameters from the fitting program to generate the spectra. All these programs are joined together with a batch file. The generated spectra are compared with the real data to see how good the fit is.

Zero Field ODNMR Results

The zero field ODNMR spectra for defect sites are shown in Figure 39. Figure 40 shows zero field ODNMR spectrum on an expanded scale for the defect site whose $^1D_2(1)$ transition occurs at 16342.2 cm^{-1}. The zero field hyperfine frequencies of intrinsic and perturbed sites are summarized in Table 17. The corresponding optical absorption lines are shown in Figure 4.

Table 17. Optical and hyperfine parameters of the $^1D_2(1) \leftrightarrow {}^3H_4(1)$ transitions for the intrinsic (in bold) and perturbed sites of Pr^{3+}: $Y_3Al_5O_{12}$ at 1.4 K.

$^1D_2(1)$ (cm^{-1})	16342.2	16391.6	16392.4	16395.6	16399.6	**16400.0**	16406.0
$^1D_2(2)$ (cm^{-1})	--	16415.6	16419.4	16404.4	16416.8	**16410.0**	--
$^3H_4(2)$ (cm^{-1})	26.8	25.6	20.8	11.5	20.4	**18.0**	16.8
$^3H_4(3)$ (cm^{-1})	78.2	39.2	49.3	47.4	52.4	**50.8**	52.0
$^3H_4(1)$ (hyperfine)							
$(\pm1/2 \leftrightarrow \pm3/2)$ (MHz)	23.68	22.39	31.33	47.17	33.07	**33.26**	35.11
$(\pm3/2 \leftrightarrow \pm5/2)$ (MHz)	32.97	29.43	35.06	76.09	40.94	**41.46**	47.76
P (MHz)	8.773	7.916	9.725	19.72	11.14	**11.26**	12.76
η	0.6172	0.682	0.8653	0.4457	0.7495	**0.7417**	0.6434

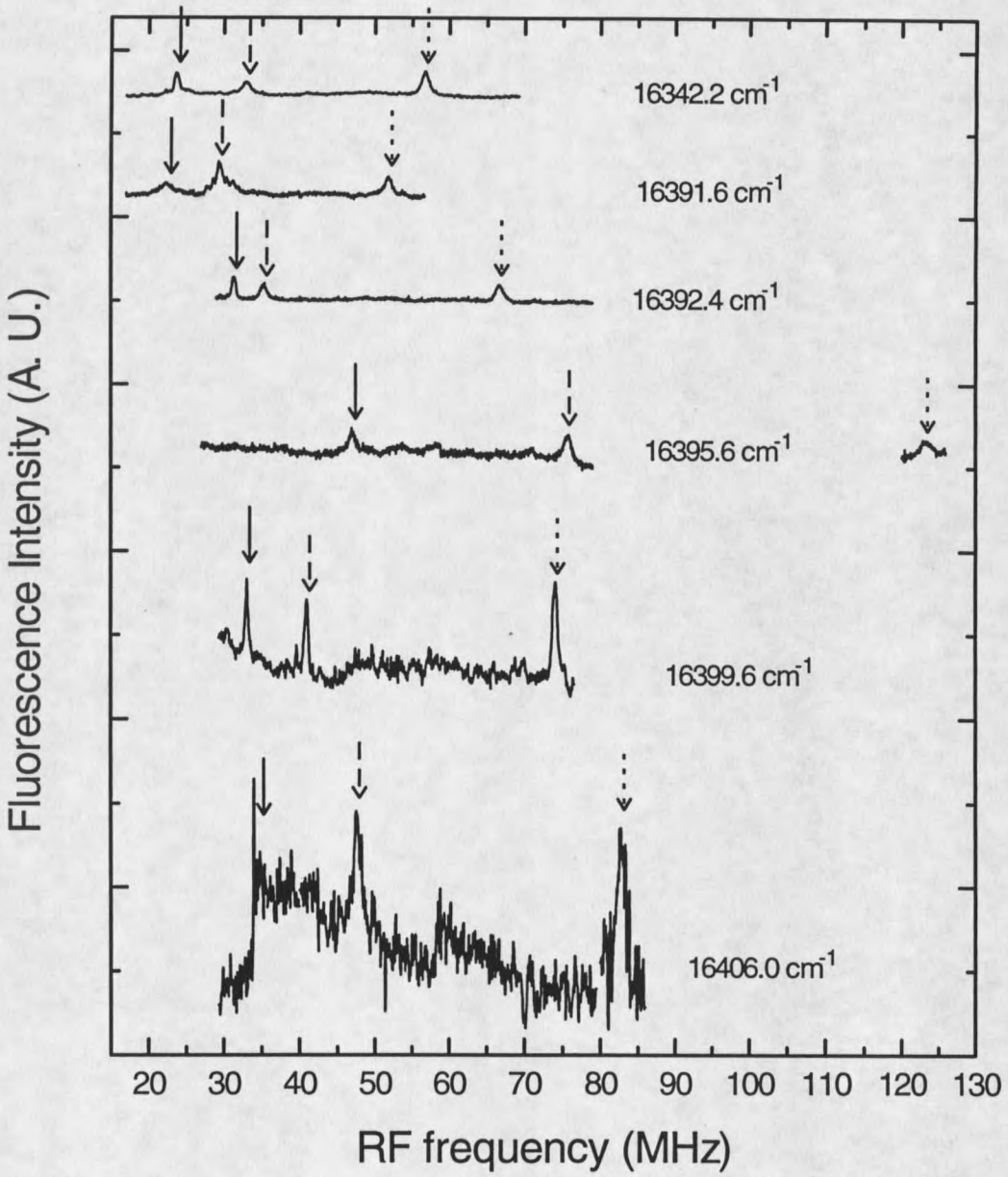

Figure 39. Zero field ODNMR spectra of defect sites in Pr^{3+}:$Y_3Al_5O_{12}$ for different $^1D_2(1)$ energies. Solid arrows mark the $|\pm 1/2\rangle \leftrightarrow |\pm 3/2\rangle$ resonances, dashed arrows mark $|\pm 3/2\rangle \leftrightarrow |\pm 5/2\rangle$ resonances and dotted arrows mark $|\pm 1/2\rangle \leftrightarrow |\pm 5/2\rangle$ resonances.

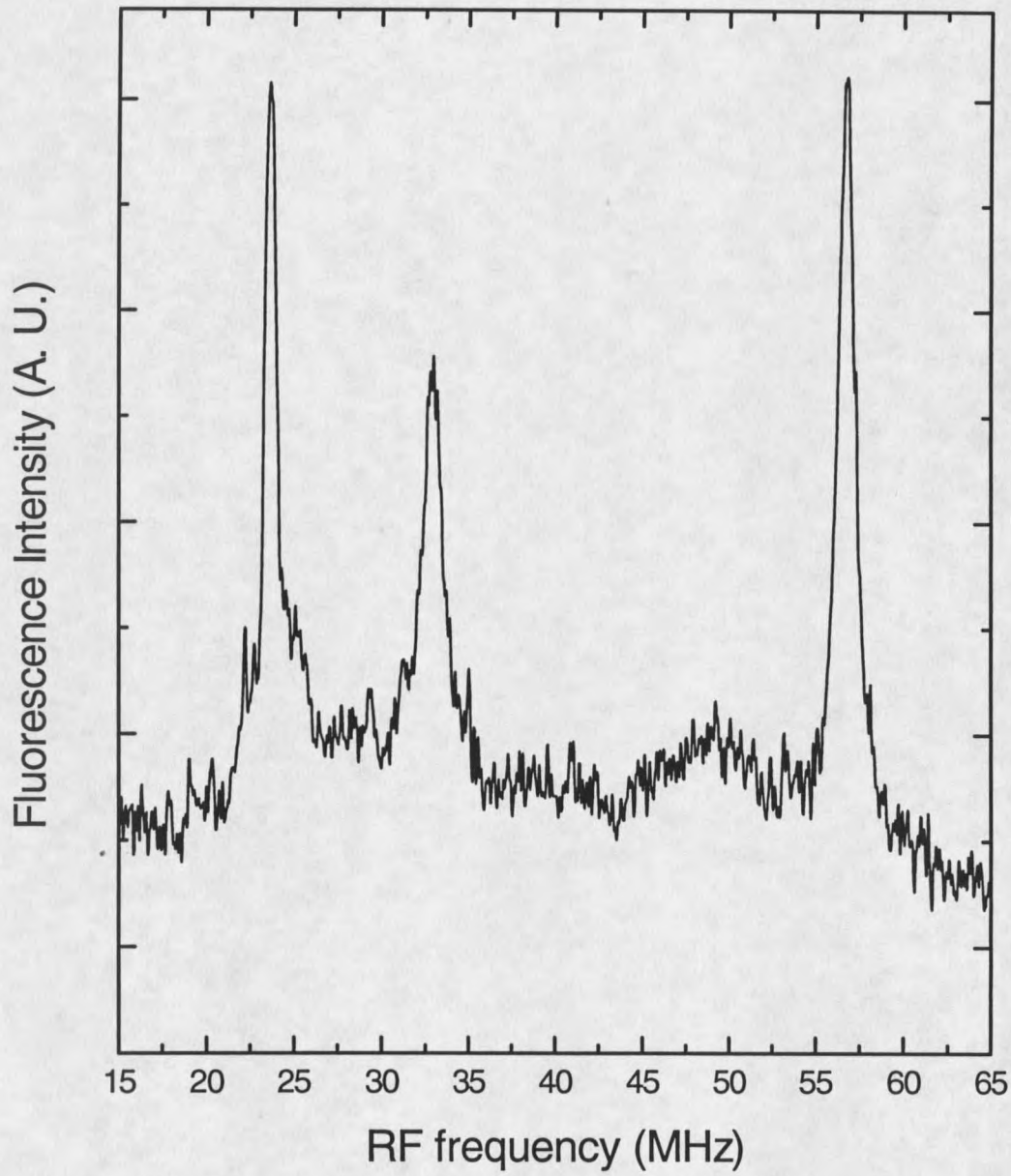

Figure 40. Zero field ODNMR spectrum of a defect site in $Pr^{3+}:Y_3Al_5O_{12}$, with $^1D_2(1)$ at 16342.2cm^{-1}, showing the $|\pm 1/2\rangle \leftrightarrow |\pm 3/2\rangle, |\pm 3/2\rangle \leftrightarrow |\pm 5/2\rangle$ and $|\pm 1/2\rangle \leftrightarrow |\pm 5/2\rangle$ resonances at 23.68, 32.97, and 56.73 MHz.

According to the hyperfine interaction theory reviewed earlier in this chapter from Eq. (3.1) to Eq. (3.4), the pseudoquadrupole Hamiltonian consists of a sum of quadrupole terms and second order magnetic hyperfine coupling. For Pr^{3+}:$Y_3Al_5O_{12}$, the following analysis indicates that the enhanced nuclear Zeeman and second order magnetic hyperfine coupling are much larger than the nuclear Zeeman and electric quadrupole interactions. The second order magnetic hyperfine contribution to the parameter P is proportional to a product of two matrix elements and an energy denominator $1/(E_1-E_0)$ where E_1 is the first excited component's energy. A plot of P vs. $1/(E_1-E_0)$ for each defect site is given in Figure 41. The clear linear relation tells us the second order magnetic hyperfine interaction is a major factor in this system. This is not true for the $EuVO_4$ system,[20] where both real and pseudo quadrupole interactions need to be considered.

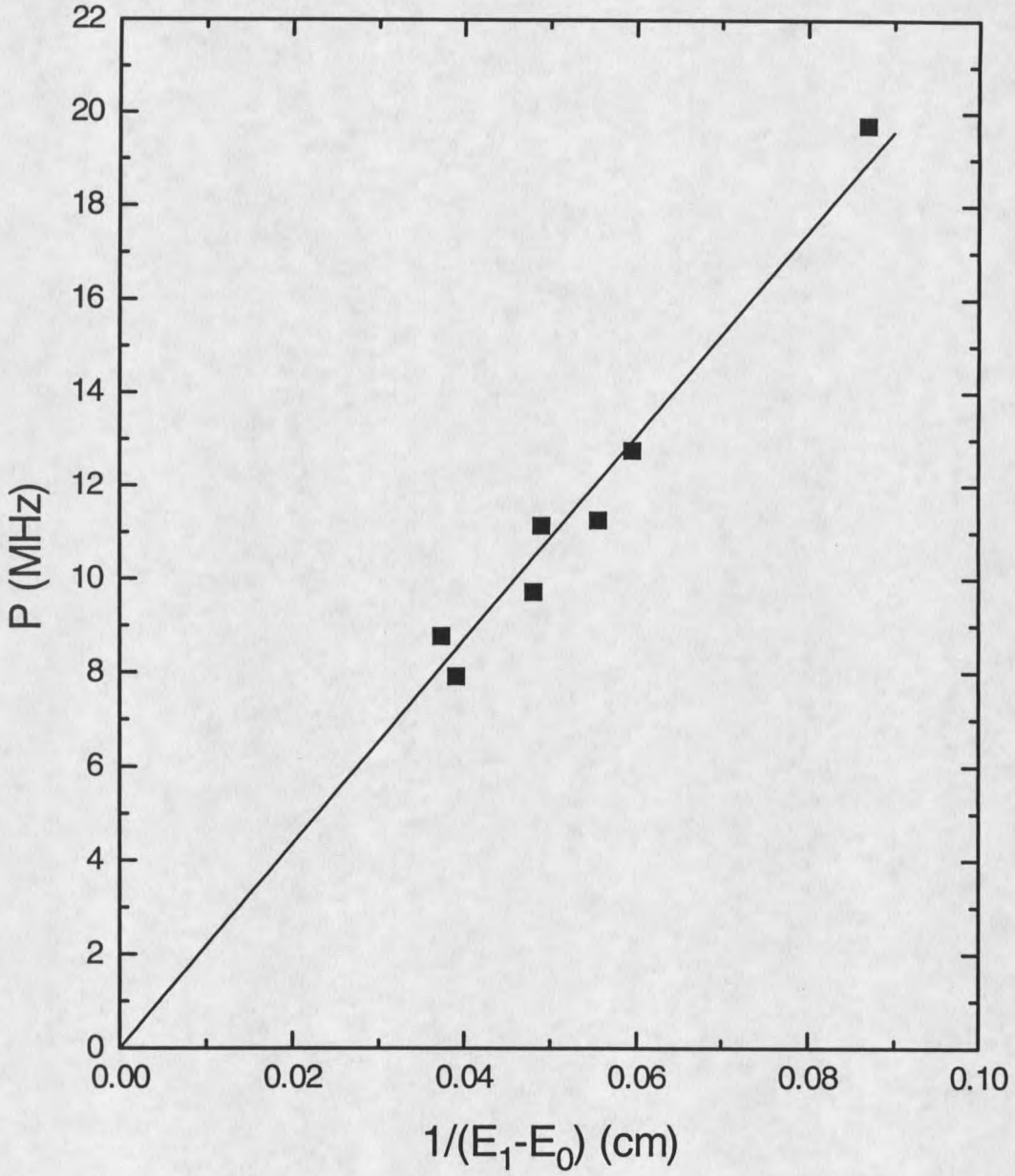

Figure 41. The quadrupole interaction parameter P is plotted vs. $1/(E_1-E_0)$ for each defect site. The straight line is a fit to the function $P = c/(E_1-E_0)$.

Angle-dependent ODNMR Results

As shown in Figure 4, the defect site with $^1D_2(1)$ at 16342.2cm^{-1} is relatively isolated from the intrinsic and other defect lines, hence it was chosen for study by the full angle-dependent ODNMR method. The other defect lines are so close to the intrinsic line that it is difficult to select a single site without exciting the intrinsic site or anothor defect site.

Figure 42 is an example of the 161 Gauss spectra of the Pr^{3+} $|\pm 1/2\rangle \leftrightarrow |\pm 3/2\rangle$ transitions with the field direction 37.4° from (001) in the (110) plane with the laser polarization parallel and perpendicular to the magnetic field direction. Figure 43 and Figure 44 are the 161 Gauss field-split spectra of the Pr^{3+} $|\pm 1/2\rangle \leftrightarrow |\pm 3/2\rangle$ transition with the field direction along (111) and (110) respectively. The RF scanning range was from 18.5 to 28.5 MHz. The magnetic field and RF scanning range were chosen to split the $|\pm 1/2\rangle \leftrightarrow |\pm 3/2\rangle$ transitions as much as possible while avoiding overlap with the $|\pm 3/2\rangle \leftrightarrow |\pm 5/2\rangle$ transitions.

Since there are 12 inequivalent sites and the $|\pm 1/2\rangle \leftrightarrow |\pm 3/2\rangle$ transition of each site splits into 4 transitions in a field, the total number of transitions is 48. In experiments not all of these were seen all the time, presumably due to the variations in transition intensity, overlap of lines, site interference, and noise. Different laser polarizations were used to increase certain transition probabilities, and hence the number of observable transitions.

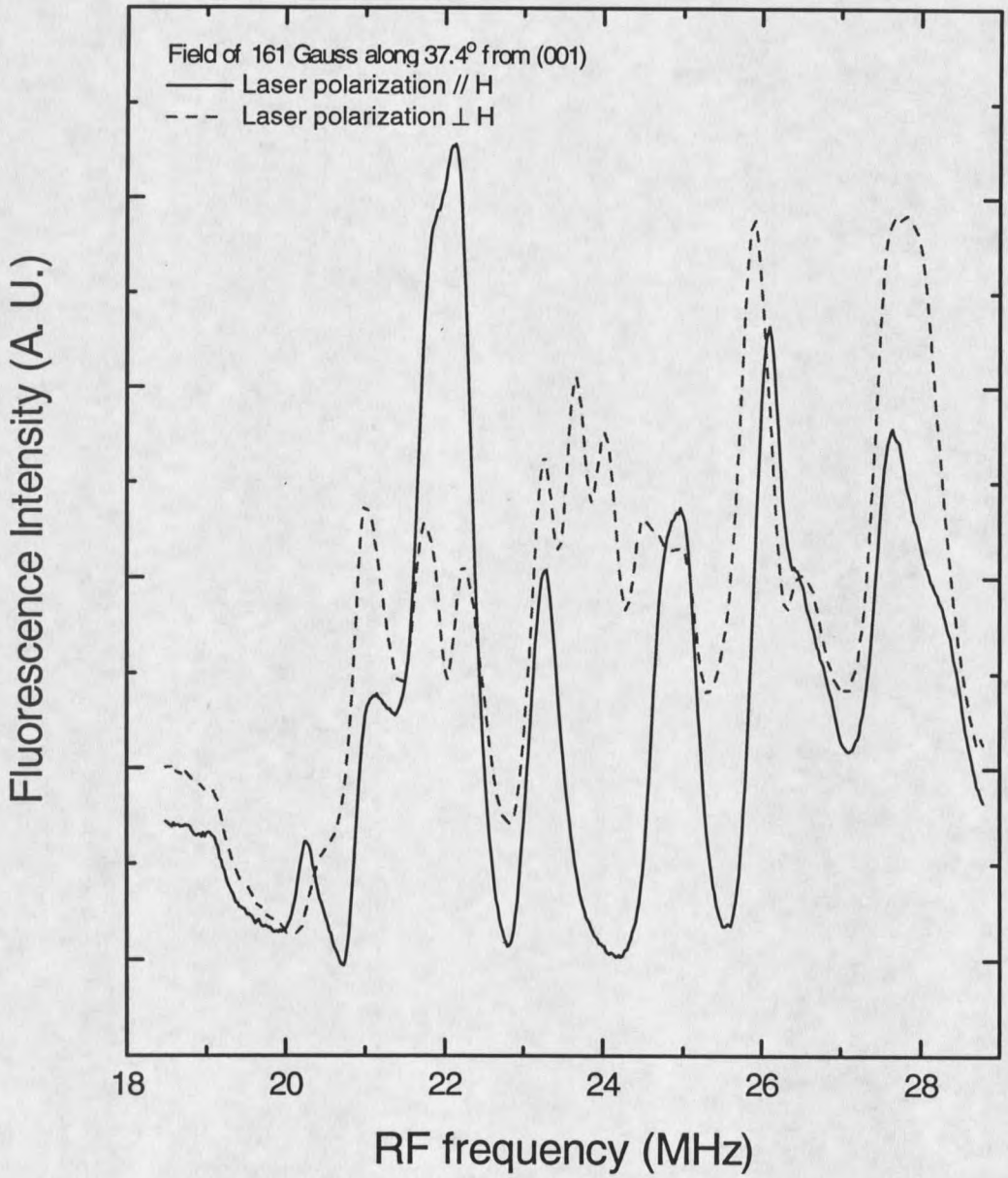

Figure 42. The 161 Gauss field-split spectrum of the Pr^{3+} $|\pm 1/2\rangle \leftrightarrow |\pm 3/2\rangle$ transition with the field direction at 37.4° from (001).

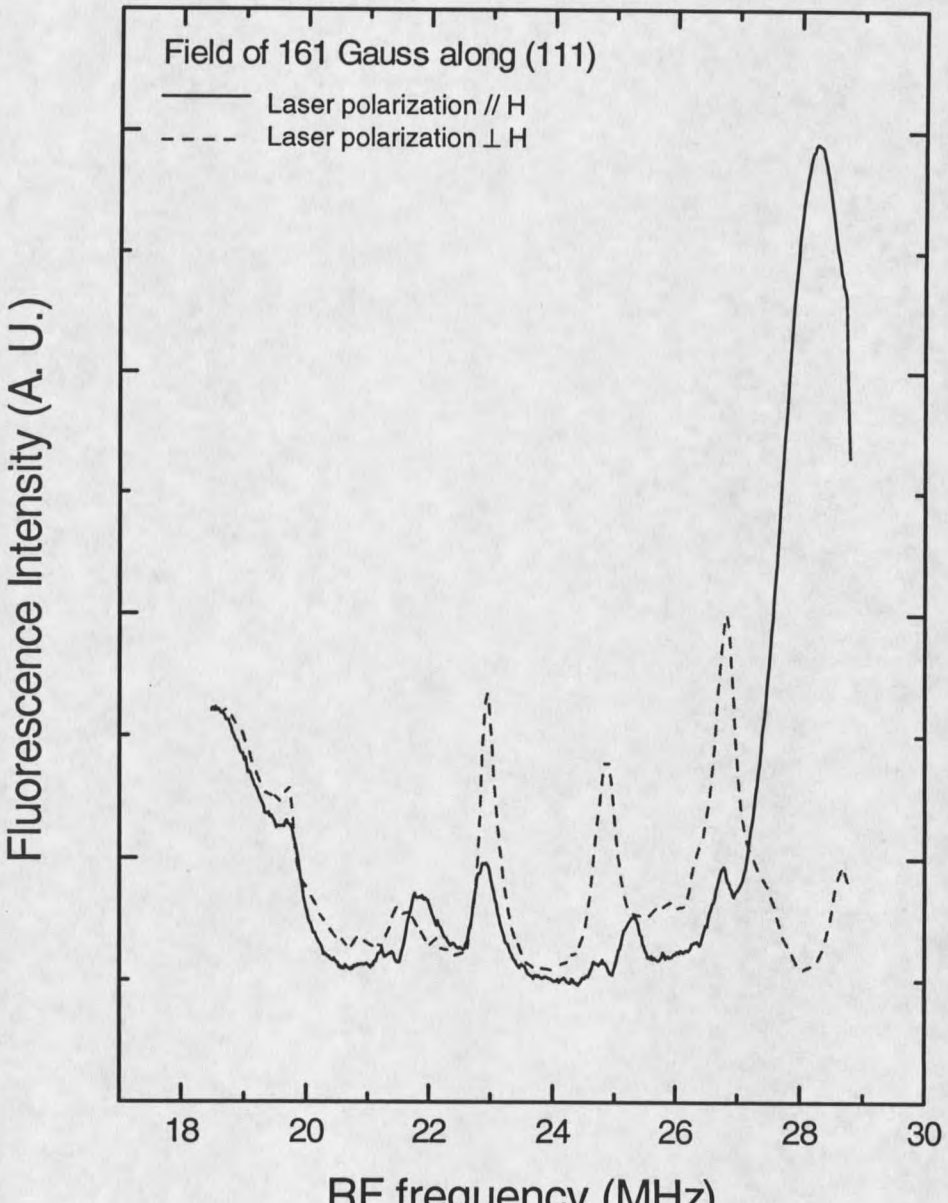

Figure 43. The 161 Gauss field-split spectrum of the Pr^{3+} $|\pm 1/2\rangle \leftrightarrow |\pm 3/2\rangle$ transition with the field direction along (111).

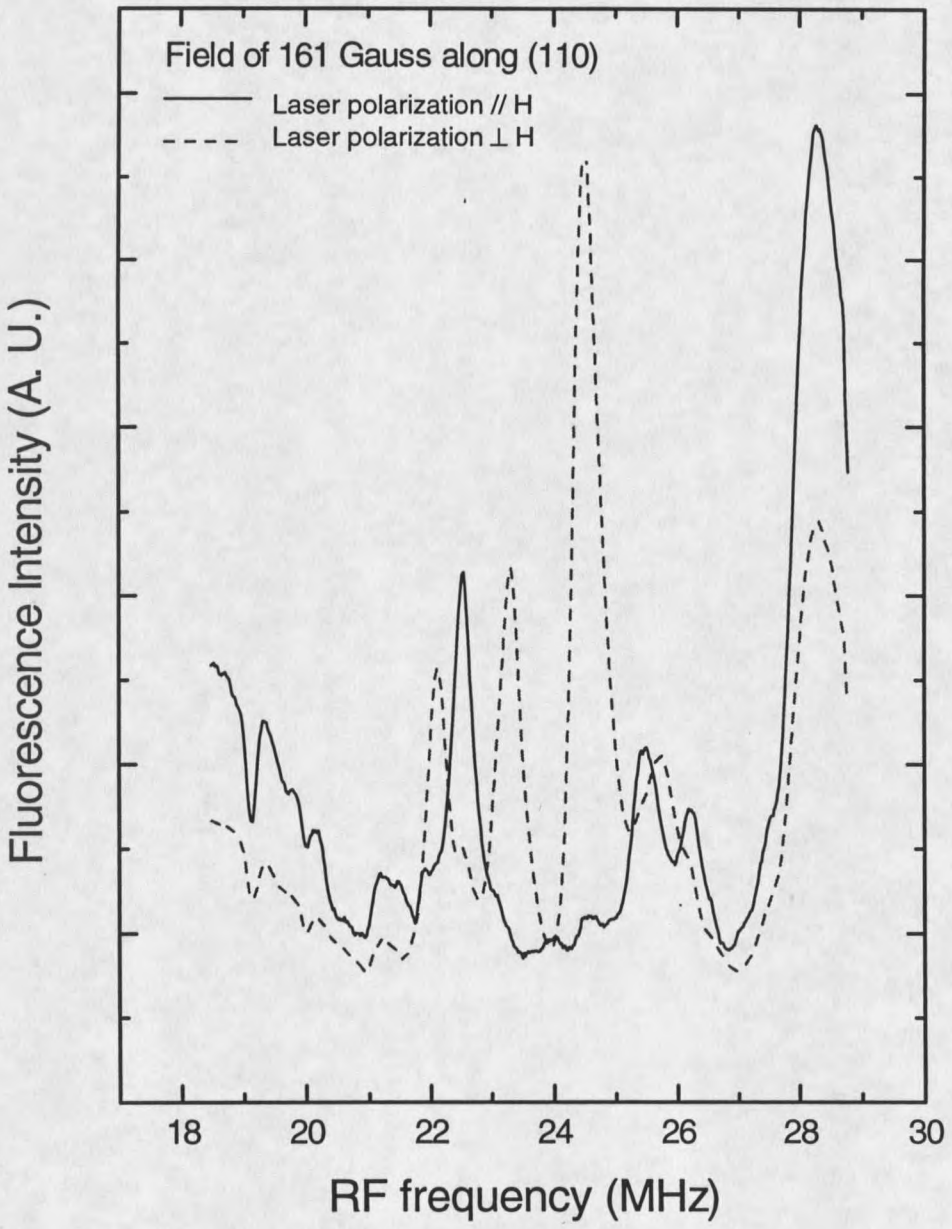

Figure 44. The 161 Gauss field-split spectrum of the Pr^{3+} $|\pm 1/2\rangle \leftrightarrow |\pm 3/2\rangle$ transition with the field direction along (110).

Hyperfine transition frequencies measured from the ODNMR spectra with the magnetic field rotating in a plane perpendicular to $(1\,\bar{1}\,0)$ are shown in Figure 45. The fit to the experimental data yielded the following six parameters: gyromagnetic ratios γ_x = 5.87 kHz/G, γ_y =1.81 kHz/G, γ_z = 23.5 kHz/G and angles (α=10°, β=21°, γ=50°) for local site principal axis orientation. Generally it is a good fit. Some small deviations are probably due to the crystal misalignment with the magnetic field. The maximum misalignment is less than 2 degrees according to a numerical study on the effect of the misalignment to the intrinsic site results. The misalignment can cause the maxima of the curves to move and the curves to become unsymmetric.

Discussion

In order to discuss the fitting of the experimental ODNMR results for the defect site, local crystallographic structures for the intrinsic site and the defect site need to be described. As indicated in

Table 1, Y^{3+} ions are normally in the *c* site, which we refer to as the intrinsic site and which has D_2 symmetry; the intrinsic Y^{3+} ion site is surrounded by four Al^{3+} ions that are located in *a* sites. With an Y^{3+} ion at (0, 1/4, 1/8) in the unit cell, the Al^{3+} ion locations are (0, 0, 0), (0, 1/2, 0), (1/4, 1/4, 1/4), and (-1/4, 1/4, 1/4). The 3 C_2 axes for the Y^{3+} ion are along (110), (1-10) and (001) as shown in Figure 46. When a Pr^{3+} ion substitutes for an Y^{3+} ion in the *c* site, the principal axes of the Pr^{3+} Hamiltonian are constrained to these directions. These principal axes were measured with Raman heterodyne ODNMR in this

chapter to within ± 2 degrees of the expected directions, an accuracy within experimental error. This confirms, with precision far exceeding that of other optical experiments, that most Pr^{3+} ions substitute for Y^{3+} ions in sites with D_2 symmetry.

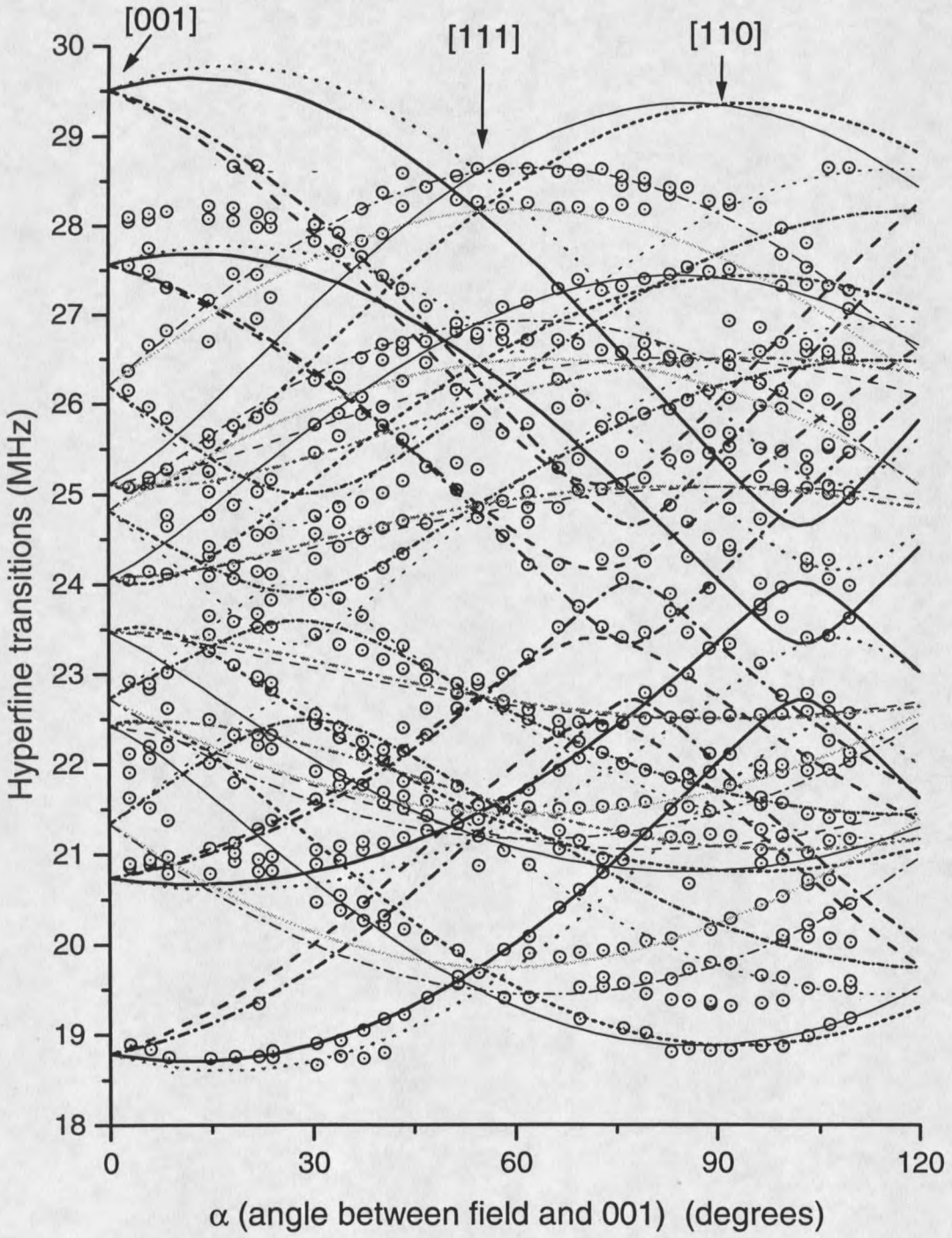

Figure 45. Zeeman splittings are mapped for the $|\pm 1/2\rangle \leftrightarrow |\pm 3/2\rangle$ transitions for a 161-G magnetic field rotating in a plane perpendicular to $(1\,\bar{1}\,0)$. α is the angle between the magnetic field and (001). The circles are data points while the curves are theoretical fits. Curves of the same line type arise from a single site orientation.

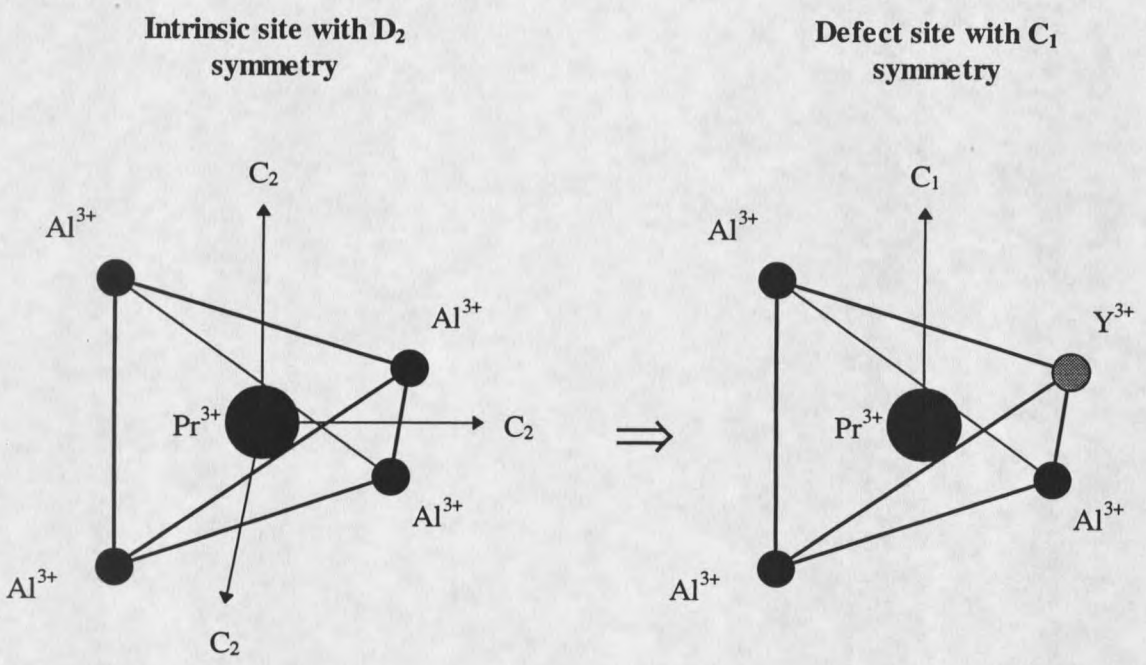

Figure 46. The intrinsic Y^{3+} site has D2 symmetry and is surrounded by four Al^{3+} ions and four O^{2-} ions. When an excess Y^{3+} ion replaces one of the four Al^{3+} ions which are near neighbors to a Pr^{3+} ion, the local symmetry of the *c* site reduces from D_2 to C_1.

Now we consider possible defect site structures that are consistent with the observations for the defect site studied here. Earlier investigation shows that, as a consequence of high temperature growth, $Y_3Al_5O_{12}$ crystals have a slight deviation from the expected stoichiometric composition, and this deviation can be specified by the formula $Y_3(Al_{0.985}Y_{0.015})_2Al_3O_{12}$.[29] If an excess Y^{3+} ion replaces one of the four Al^{3+} ions described above, the local symmetry of the Y^{3+} ion *c* site is reduced from D_2 to C_1 as shown in Figure 42. When a Pr^{3+} ion is doped into this perturbed Y^{3+} site, there will be no

special direction to constrain the orientation of the principal axes of the the Pr^{3+} ion Hamiltonian.

That situation is compatible with the fitting results presented in the last section for the defect site. The principal axis orientation for the hyperfine interaction for the defect experimentally studied here is specified by (α=10°, β=21°, γ=50°) and is not along any C_4, C_3, or C_2 symmetry axis of the crystal.

The presence of the excess Y defect is also supported by conventional spectroscopy in Chapter 2. The high resolution white light absorption measured the percentage of Pr^{3+} ions in defect sites. The observed percentage could be attributed to 1% of the Y^{3+} ions substituting for neighboring Al^{3+} ions.

We can be sure that the defect studied by Zeeman ODNMR is definitely not caused by an excess of Y^{3+} ions substituting for Al^{3+} in *d* sites. Our results show the defect site has C_1 symmetry, but this substitution could only reduce the D_2 symmetry of nearest-neighbor *c* sites to C_2 with the symmetry axis along (001).

Oxygen vacancies or anionic impurities such as OH^{-1} can also reduce the D_2 symmetry of a *c* site to C_1. However there is not yet enough spectroscopic data to determine the effect of such impurities on the defects.

To further study the defects, additional experiments need to be done. One future project is to study $Er_3Al_5O_{12}$. A small percentage of Er^{3+} ions may substitute for Al^{3+} ions in *a* sites. Since the *a* site (C_{3i} symmetry) has inversion symmetry, electric dipole transitions are forbidden and the magnetic dipole transitions are weakly allowed only when $\Delta J = 0, \pm 1$. Preliminary absorption spectra were taken in a sample of this compound.

In the $^4S_{3/2}$ region shown in Figure 47, the expected electric-dipole-allowed intrinsic site electronic transitions and associated vibronic transitions were observed for the intrinsic site Er^{3+} ions, but in addition, some weak vibronic transitions were observed without an electronic transition beside them. These weak vibronic transitions extend for about 500 cm^{-1} above the zero-phonon line and have the same pattern as the vibronic transitions for the intrinsic Er^{3+} site; this may indicate that these vibronic transitions originate from Er^{3+} in *a* sites (C_{3i} symmetry). Further experiments could be done by observing the fluorescence while pumping these anomalous $^4S_{3/2}$ vibronic transitions. Magnetic-dipole-allowed infrared absorption for the $^4I_{15/2} \leftrightarrow {}^4I_{13/2}$ transitions may provide information on the extent of Er^{3+} ions substituting for Al^{3+} ions. Other techniques, such as applying a dc electric field to destroy the inversion symmetry of the *a* sites may induce some new electronic transitions in $^4S_{3/2}$ region, allowing the electronic origin transiton to be observed. Since the centrosymmetric C_{3i} symmetry defect sites would have a long lifetime of the $^4I_{13/2}$ multiplet, time-resolved fluorescence at 1.5 μm also could be adequate to separate the centrosymmetric site from the intrinsic sites.

Conclusion

Using ODNMR, we have studied the defect sites of $Pr^{3+}:Y_3Al_5O_{12}$ for which we have no predetermined structural information. From the Zeeman ODNMR spectra we were able to determine the principal directions of the hyperfine tensor and the gyromagnetic ratios for one defect site. The local symmetry of the defect site was determined to be C_1. The mechanism proposed for the defect center studied is that a few

percent of excess Y^{3+} ions substitute for Al^{3+} ions in *a* sites, but confirmation of that assignment requires further study.

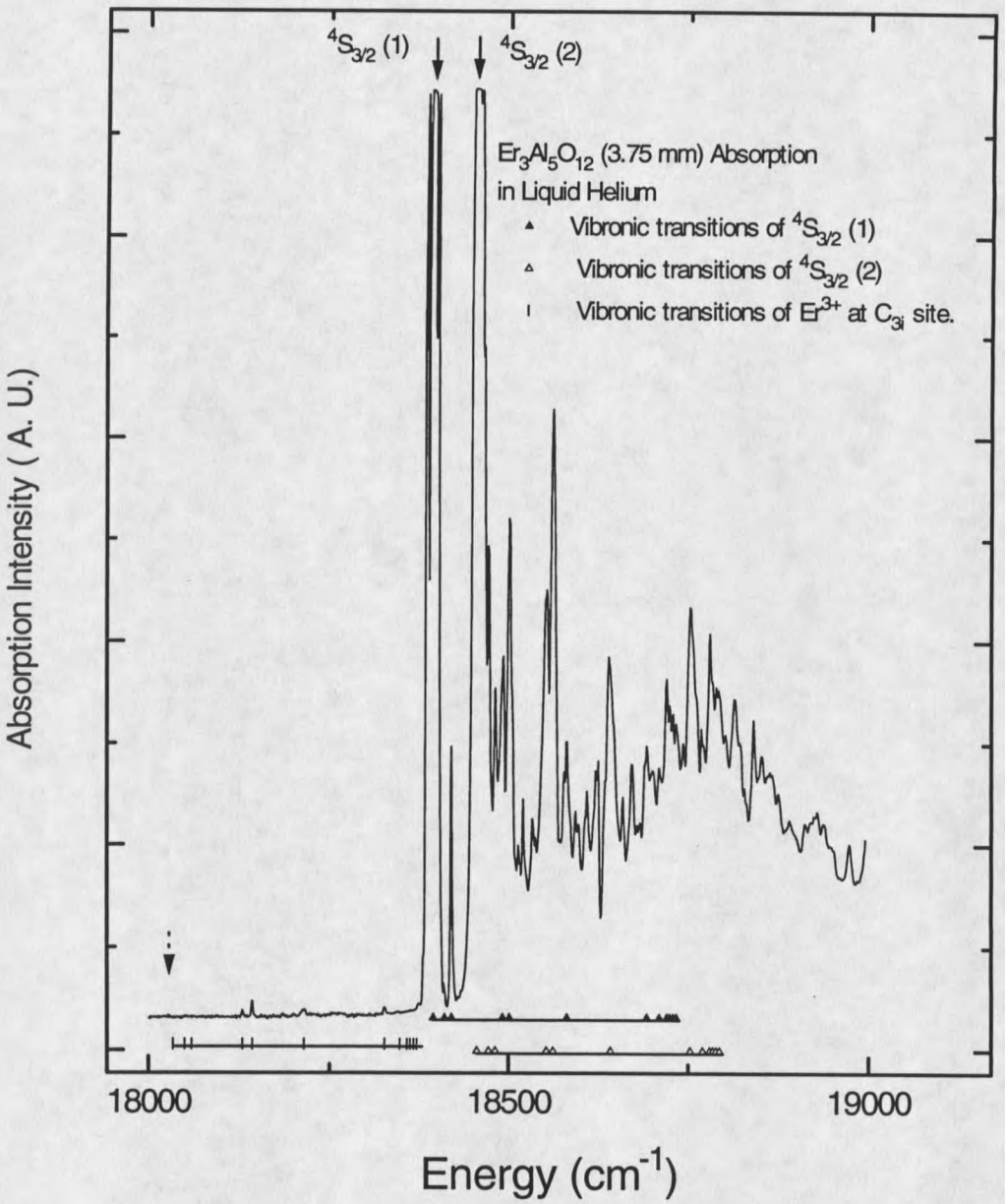

Figure 47. Absorption spectrum of $^4S_{3/2}$ of $Er_3Al_5O_{12}$ at 1.4 K. The two solid arrows indicate two allowed electronic transitions to $^4S_{3/2}$ (1) and $^4S_{3/2}$ (2) of Er^{3+} at the intrinsic D_2 site. They are saturated. The solid and open triangles mark the vibronic transitions accompanying the two electronic transitions. The dashed arrow indicates the possible energy level position of Er^{3+} at a C_{3i} site. The vertical bars are the vibronic transitions of Er^{3+} at the C_{3i} site.

References for Chapter 3

1. R. M. Macfarlane and R. M. Shelby, in *Spectroscopy of Solids Containing Rare Earth Ions*, edited by A. A. Kaplyanskii and R. M. Macfarlane (North-Holland, Amsterdam, 1987), p. 51-184.

2. J. Mlynek, N. C. Wong, R. G. DeVoe, E. S. Kintzner and R. G. Brewer, Phys. Rev. Lett. **50**, 993 (1983).

3. M. Mitsunaga, E. S. Kintzer and R. G. Brewer, Phys. Rev. Lett. **52**, 1484 (1984).

4. M. Mitsunaga, E. S. Kintzer and R. G. Brewer, Phys. Rev. B **31**, 6947 (1985).

5. D. R. Taylor, Opt. Commun. **52**, 1484 (1984).

6. E. S. Kintzer, M. Mitsunaga and R. G. Brewer, Phys. Rev. B **31**, 6958 (1985).

7. L. E. Erickson, Phys. Rev. B **19**, 4412 (1979).

8. L. E. Erickson, Phys. Rev. B **24**, 5388 (1981).

9. R. M. Macfarlane and R. M. Shelby, Opt. Lett. 6, 96 (1981)

10. B. R. Reddy and L. E. Erickson, Phys. Rev. B **27**, 5217 (1983).

11. R. M. Shelby, A. C. Tropper, R. T. Harley and R. M. Macfarlane, Opt. Lett. **8**, 304 (1983).

12. P. D. Bloch, W. S. Brocklesby, R. T. Harley and D. R. Taylor, J. DE Physique Colloque C7, **46**, c7-523 (1985).

13. M. K. Kim, and R. Kachru, Phys. Rev. B **40**, 2082 (1989).

14. B. Bleaney, J. Appl. Phys. **34**, 1024 (1963).

15. P. Hu, R. Leigh and S. R. Hartmann, Phys. Lett. A **40**, 164 (1972).

16. P. F. Liao, P. Hu, R. Leigh and S. R. Hartmann, Phys.Rev. A **9**, 332 (1974).

17. L. E. Erickson, Opt. Commun. **21**, 147 (1977).

18. M. A. Teplov, Zh. Eksp. Teor. Fiz. **53**, 1510 (1967). [Sov. Phys. -- JETP **26**, 872 (1968)].

19. N. C. Wong, E. S. Kintzer, J. Mlynek, R. G. DeVoe, and R. G. Brewer, Phys. Rev. B **28**, 4993 (1983).

20. Y. Sun, Ph. D Thesis (Montana State University, Bozeman, 1993).

21. R. L. Cone, M. J. M. Leask, M. G. Robinson, and B. E. Watts, J. Phys. C **21**, 3361 (1988).

22. W. T. Carnall, P. R. Fields and R. Sarup, J. Chem. Phys. **51**, 2587 (1969).

23. R. Bayerer and J. Heber and D. Mateika. Z. Phys. B - Condensed Matter **64**, 201 (1986).

24. M. D. Seltzer, M. E. Hills and J. B. Gruber, Phys. Rev. B **46**, 8007 (1992).

25. Yu. K. Voronko, N. A. Eskov, and L. M. Ershova, Optics and Spectroscopy, **70**, 608 (1991).

26. H. Gross, J. Neukum, and J. Heber, Phys. Rev. B 48, 9264 (1993).

27. V. Lupei, A. Lupei, C. Tiseanu, S. Georgescu, C. Stoicescu, and P. M. Nanau, Phys. Rev. B **51**, 8 (1995).

28. E. A. Wood, *Crystals and light; an introduction to optical crystallography* (D. Van Nostrand, 1964).

29. S. Geller, G. P. Espinosa, L. D. Fullmer, and P. B. Crandall, Mater. Res. Bull. **7**, 1219 (1972).

CHAPTER 4

OPTICAL DEPHASING MECHANISMS IN Tm^{3+}:$Y_2Si_2O_7$

Introduction

Demonstrations of practical optical signal processing and optically-addressed data storage[1-11] have stimulated a search for new materials with better capabilities. Several limits on material performance are a) the inhomogeneous linewidth, which limits the data bandwidth, b) the theoretical storage density per pixel given by the ratio of the inhomogeneous to homogenous linewidths Γ_{inh}/Γ_h, and c) the optical coherence time $T_2 = 1/(\pi\Gamma_h)$, which limits the length of data pulse trains.[12] There is particular interest in Tm^{3+} doped materials, since the $^3H_6$ (1) $\rightarrow$ $^3H_4$ (1) transition of Tm^{3+} occurs in the 790 nm wavelength region accessible by GaAlAs semiconductor lasers. Recently, Tm^{3+}:$Y_3Al_5O_{12}$ has been shown[13] to be a suitable material with a ratio $\Gamma_{inh}/\Gamma_h \sim 10^7$, and it has been used in demonstrations of both signal processing and time domain data storage.[11] The silicate material reported here opens a new region of parameter space with potentially much higher data rates, since the Tm^{3+} $^3H_6$ (1) $\rightarrow$ $^3H_4$ (1) transition has an inhomogeneous linewidth a factor of five larger than $Y_3Al_5O_{12}$ while preserving the large ratio $\Gamma_{inh}/\Gamma_h \sim 10^7$.

Rare-earth ions with an even number of 4f electrons have non-magnetic singlet electronic states when doped into crystalline sites of less than axial symmetry and are thus relatively insensitive to homogeneous broadening by fluctuating local magnetic fields arising from mutual nuclear spin flips of host lattice nuclei or electronic spin flips of other ions.[14] The Tm^{3+} ion ($4f^{12}$) is therefore a good candidate for long optical coherence times at low temperatures. Since Tm^{3+} has nuclear spin I = 1/2, it has the further advantage that there are no zero-field hyperfine splittings to contribute modulation in optical coherent transients with short-pulse excitation or to create a complicated pattern of sideholes and antiholes in a hole burning spectrum. The storage time in Tm^{3+} materials is limited to ~10 ms, the population lifetime of the $^3F_4$ metastable levels; nevertheless, there are potential applications in signal processors and cache memories.

Yttrium silicates are desirable host materials since the nuclear magnetic moment of ^{16}O is zero, that of ^{89}Y is very small, and ^{29}Si has low isotopic abundance. This minimization of the effect of nuclear spins should result in narrow homogeneous linewidths for even-electron dopant ions. The expected narrow homogeneous linewidths have been verified for $Pr^{3+}:Y_2SiO_5$ and $Eu^{3+}:Y_2SiO_5$,[15, 7, 16] so $Tm^{3+}:Y_2SiO_5$[17] and $Tm^{3+}:Y_2Si_2O_7$ are particularly interesting candidates for optical memory and signal processing applications.

In solids doped with rare-earth ions like Tm^{3+}, the homogeneous linewidth Γ_h may be written as a sum of contributions,

$$\Gamma_h = \Gamma_{pop} + \Gamma_{Tm\text{-}Tm} + \Gamma_{Tm\text{-}host} + \Gamma_{phonon}. \qquad (4.1)$$

The natural linewidth $\Gamma_{pop} = 1/(2\pi T_1)$ arises from the excited state lifetime T_1. The second term $\Gamma_{Tm\text{-}Tm}$ arises from Tm-Tm interactions and can be minimized by using a low concentration of dopant ions such as 0.1% and by using low excitation intensity to reduce instantaneous spectral diffusion effects.[18-20] The $\Gamma_{Tm\text{-}host}$ term is due to the interaction of the dopant ions with fluctuating spins of the host lattice, and as noted above, it can be minimized by choosing an appropriate host crystal that has constituent ions with zero or small nuclear magnetic moments. The Γ_{phonon} contribution can usually be suppressed by working at temperatures below 2 K; however, for Tm^{3+}:$Y_2Si_2O_7$ the lowest excited component of the ground $^3H_6$ multiplet is only 6 cm^{-1} above the ground state, and the Γ_{phonon} contribution continues to decrease down to 1.2 K.

Experiment and Results

Single crystals of yttrium disilicate doped with 0.1% thulium were provided by K. W. Godfrey and F. R. Wondre at Clarendon Laboratory, University of Oxford, United Kingdom. The crystals were grown by slow cooling at high temperature from a bismuth oxide flux stabilized with boron and vanadium oxides.[21] The starting materials were sealed into a platinum crucible and heated to 1240°C, soaked for 20 hours then cooled at 1.5°C/hr to 1120°C. After inverting the crucible, to separate the crystals from the flux, it was cooled to room temperature and the crystals were mechanically recovered. They were identified by X-ray powder diffraction as type D yttrium disilicate, which is monoclinic, belonging to the $P2_1/a$ spacegroup.[22]

Measurements are reported here for the transition from the lowest level of the $^3H_6$ ground state multiplet, $^3H_6$ (1), to the lowest level of the $^3H_4$ excited state multiplet, $^3H_4$ (1), which is a metastable level of interest for long dephasing times. The $^3H_6$ (1) $\rightarrow$ $^3H_4$ (1) transition at 790.427 nm (12651.4 cm^{-1}) had a peak absorption coefficient of $\alpha = 0.4$ cm^{-1} for our unoriented sample; the crystal was 0.5 mm thick and had 2% absorption. The inhomogeneous linewidth was 100 GHz, a value significantly larger than the 20 GHz we have obtained for 0.1% Tm^{3+}:$Y_3Al_5O_{12}$. This larger value of the inhomogeneous linewidth for Tm^{3+}:$Y_2Si_2O_7$ translates into an important potential for higher system data bandwidths in signal processing and cache storage applications. The fluorescence lifetime of the $^3H_4$ (1) level was found to be $T_1 = 68 \pm 3$ μs, making a contribution of $\Gamma_{pop} = 2.3 \pm 0.1$ kHz to the homogeneous linewidth.

Two-pulse photon-echo measurements were made using a Coherent 899-21 single-mode cw Ti:sapphire laser and the apparatus described previously.[16] The laser was focused onto the sample with a beam waist of radius $w_0 = 75$ μm. Photon echoes were excited using 0.5 μs pulses at a repetition rate of 7 Hz to allow ample time for population relaxation of metastable multiplets such as $^3F_4$. The sample was immersed in liquid helium, and the temperature was regulated by controlling the helium vapor pressure.

Contributions to the homogeneous linewidth were characterized by recording photon echo decays as a function of laser excitation intensity, temperature, and magnetic field. Echo decays for the $^3H_6$ (1) $\rightarrow$ $^3H_4$ (1) transition recorded at temperatures of 1.24 K and 2.17 K using a laser excitation intensity of 9.6 W/cm^2 are shown in Figure 48. These

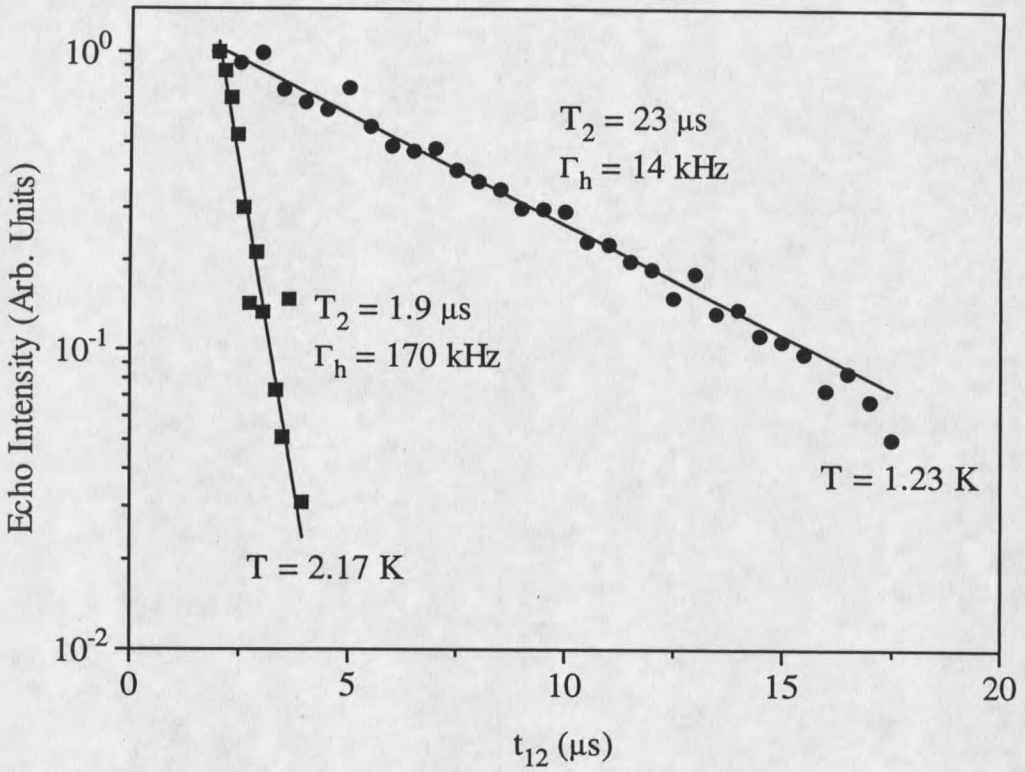

Figure 48. Photon echo decays for the $^3H_6(1) \rightarrow {}^3H_4(1)$ transition of $Tm^{3+}:Y_2Si_2O_7$ recorded at temperatures of 1.24 K and 2.17 K using an excitation power density of 9.6 W/cm^2 and excitation pulse widths of 0.5 μs. These conditions yielded dephasing times of T_2 = 23 μs and T_2 = 1.9 μs corresponding to homogeneous linewidths of 14 kHz and 170 kHz respectively.

conditions yielded dephasing times of $T_2 = 23 \pm 2$ μs and $T_2 = 1.9 \pm 0.2$ μs corresponding to homogeneous linewidths of 14 ± 2 kHz and 170 ± 20 kHz respectively. Figure 49 shows the laser excitation intensity dependence of the homogeneous linewidth arising from instantaneous spectral diffusion at 1.45 K. The instantaneous diffusion contribution to the homogeneous linewidth is proportional to the number of ions N changing state during the echo pulse sequence; this causes abrupt random shifts of the energy levels of

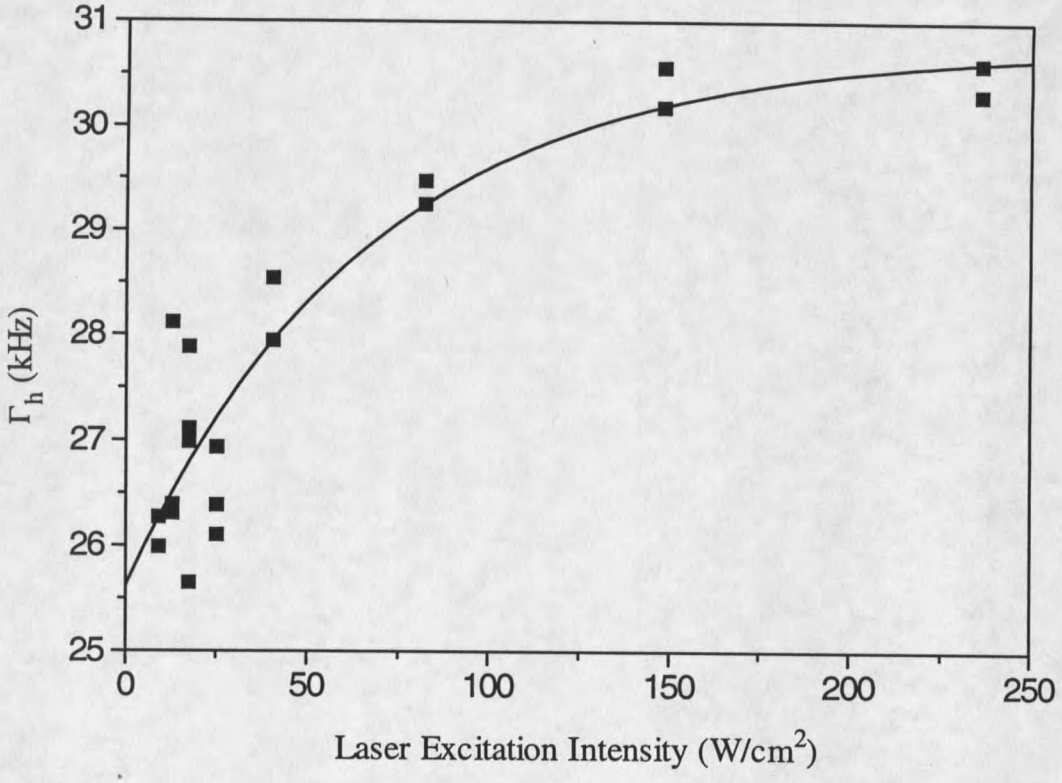

Figure 49. Dependence of homogeneous linewidth on excitation power density recorded at a temperature of 1.45 K showing the contribution from instantaneous spectral diffusion. Both echo excitation pulses had the same intensity, and their intensities were varied simultaneously. The solid line is a fit to a simple rate equation model.

neighboring ions resulting in incomplete rephasing and an apparent broadening of the homogeneous linewidth.[18-20] Since $T_1 >> T_2/4$, the number of ions changing state due to population decay during the echo measurement process is small, and thus the effects due to the first pulse are negligible.[18] The data in Figure 49 were extrapolated to zero excitation intensity using a simple rate equation model that accounted for the onset of

two-level saturation. This gave a zero-excitation-intensity homogeneous linewidth of $\Gamma_0 = 25.6 \pm 0.5$ kHz at 1.45 K.

The extrapolated linewidth Γ_0 = 25.6 kHz contains contributions from the ^{89}Y nuclear spin fluctuations as well as significant phonon-induced contributions. To explore the effects of ^{89}Y nuclear spin fluctuations, echo decays were recorded in an applied magnetic field of ~100 G. No measurable narrowing of the homogeneous linewidth was observed, a result that may be explained by comparison with Pr^{3+}:Y_2SiO_5 and Eu^{3+}:Y_2SiO_5, where contributions from ^{89}Y nuclear spin fluctuations were found to be ~1 kHz, and ~100 Hz respectively.[16] The nuclear magnetic moment of Tm (-0.231 μ_N) is considerably smaller than that of Pr (4.09 μ_N), so the contribution for Tm from ^{89}Y mutual nuclear spin fluctuations is expected to be only several hundred Hz, which is within the experimental uncertainty of these measurements.

There was a strong temperature dependence of the homogeneous linewidth, even below 2 K, as shown in Figure 50. For crystalline hosts, there are two primary mechanisms for phonon-induced contributions to the homogeneous linewidth, a direct process and a two phonon Raman process.[23] The direct process involving resonant-phonon-induced transitions between two adjacent electronic states results in a temperature dependence for the dephasing rate described by[23]

$$\frac{1}{T_2} = \frac{1}{T_1} e^{-\Delta / kT}, \tag{4.2}$$

where here T_1 is the spontaneous relaxation time of the second crystal field level of the multiplet and Δ is the energy separation of the two levels. The temperature dependence

observed for this material between 1.24 K and 2.17 K is well described by resonant phonon interactions between the $^3H_6$ (1) ground state and the next higher crystal field level $^3H_6$ (2). The data of Figure 50 were fitted to Eq. (4.2), yielding T_1 = 40 ns and Δ = 6.7 cm^{-1}. This crystal field splitting is in good agreement with the 6 ± 1 cm^{-1} value measured in fluorescence experiments. The T = 0 K homogeneous linewidth of 6 ± 2 kHz obtained from the fit contains the contribution Γ_{pop} = 2.3 ± 0.1 kHz plus a contribution from instantaneous spectral diffusion that can be estimated from the data of Figure 49 to be ~ 0.5 kHz. The residual 3.2 kHz is within the experimental and fitting uncertainties, although some portion of this width is undoubtedly due to ^{89}Y nuclear spin fluctuations. There is also a small contribution from vanadium electron spin fluctuations; V^{4+} is present as a consequence of flux growth at a concentration of 0.01% estimated from the intensity of an eight-line $^{50}V^{4+}$ (I = 7/2) pseudo-S-state EPR spectrum. These crystals also had a broad absorption band starting at 410 nm extending beyond 300 nm which we attribute to V^{4+}.

Conclusion

In conclusion, we have characterized the optical dephasing mechanisms for a new material, Tm^{3+}:$Y_2Si_2O_7$. These studies were motivated by a search for materials with a broad inhomogeneous linewidth Γ_{inh} and long optical dephasing time T_2 (narrow Γ_h), as these are advantages for optically-addressed data storage and signal processing. The broad Γ_{inh} of 100 GHz for the $^3H_6$ (1) → $^3H_4$ (1) transition of Tm^{3+}:$Y_2Si_2O_7$ provides five times

greater signal processing bandwidth than provided by previously known Tm^{3+} materials; furthermore, this transition at 790 nm is well suited for use with available semiconductor diode-lasers. Our earlier studies of silicates[16, 17] had indicated that $Y_2Si_2O_7$ should be a good host for exceptionally long dephasing times on this transition; however, this was not the case due to a strong temperature-dependent phonon-induced dephasing and a relatively short fluorescence lifetime. The temperature dependence arose from an "accidentally" small ground state crystal field splitting of 6 cm^{-1}. Even though Γ_h is broader than expected, the theoretical storage density $\Gamma_{inh}/\Gamma_h = 7 \times 10^6$ is competitive with other known materials such as $Tm^{3+}:Y_3Al_5O_{12}$. Some decrease in the homogeneous linewidth might be achieved with material purity improvements that are under way. Other "low nuclear magnetism" hosts remain to be investigated.

This work has been published in Optics Letters.[24]

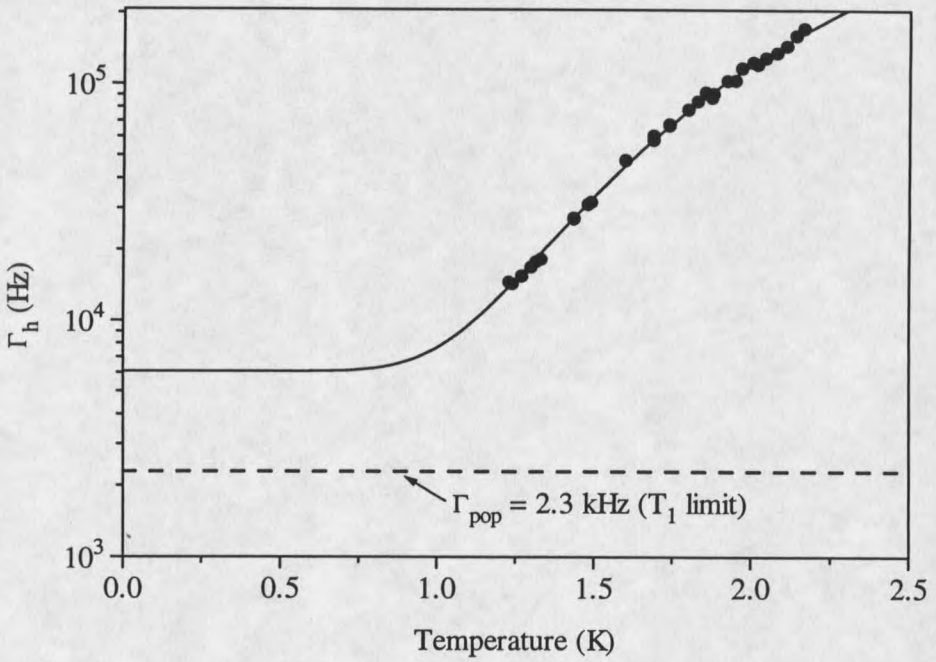

Figure 50. Temperature dependence of homogeneous linewidth of the $^3H_6$ (1) $\rightarrow$ $^3H_4$ (1) transition of 0.1% Tm^{3+} in $Y_2Si_2O_7$. The solid line is a fit to Eq. (4.2) representing the direct phonon process. All measurements were obtained using an excitation power density of 9.6 W/cm^2.

References for Chapter 4

1. *Persistent Spectral Hole-Burning: Science and Applications*, Vol. 44 Topics in Current Physics, Edited by W. E. Moerner, (Springer, 1988).

2. T. W. Mossberg, Opt. Lett. **7**, 77 (1982).

3. W. R. Babbitt and T. W. Mossberg, Opt. Commun. **65**, 185 (1988).

4. M. Mitsunaga, R. Yano, and N. Uesugi, Opt. Lett. **16**, 1890 (1991).

5. T. W. Mossberg Opt. Lett. **17**, 535 (1992).

6. R. Yano, M. Mitsunaga, and N. Uesugi, J. Opt. Soc. Am. B **9**, 992 (1992).

7. Y. S. Bai and R. Kachru, Opt. Lett. **18**, 1189 (1993); X. A. Shen, and R. Kachru, Opt. Lett. **18**, 1967 (1993); X. A. Shen, E. Chiang, and R. Kachru, Opt. Lett. **19**, 1246 (1994).

8. W. R. Babbitt and T. W. Mossberg, J. Opt. Soc. Am B **11**, 1948 (1994).

9. W. R. Babbitt and T. W. Mossberg, Opt. Lett. **20**, 910 (1995).

10. W. R. Babbitt and J. A. Bell, Appl. Opt. **33**, 1538 (1994).

11. H. Lin, T. Wang, G. A. Wilson, and T. W. Mossberg, Opt. Lett. **20**, 91 (1995); H. Lin, T. Wang, and T. W. Mossberg, Opt. Lett. **20**, 1658 (1995).

12. The swept carrier method of references 5 and 11 can overcome this limitation, but the ratio Γ_{inh}/Γ_h remains a figure of merit of materials for these applications.

13. R. M. Macfarlane, Opt. Lett. **18**, 1958 (1993).

14. R. M. Macfarlane and R. M. Shelby, in *Spectroscopy of Solids Containing Rare Earth Ions*, edited by A. A. Kaplyanskii and R. M. Macfarlane (North-Holland, Amsterdam, 1987), p. 51-184.

15. R. Yano, M. Mitsunaga, and N. Uesugi, Opt. Lett. **16**, 1884 (1991).

16. R. W. Equall, Y. Sun, R. L. Cone and R. M. Macfarlane, Phys. Rev. Lett. **72**, 2179 (1994); R. W. Equall, R. L. Cone, and R. M. Macfarlane, Phys. Rev. B 52, 3963 (1995).

17. R. W. Equall, G. M. Wang, R. L. Cone, R. M. Macfarlane, and R. L. Hutcheson, Submitted to Phys. Rev. B.

18. G. K. Liu, M. F. Joubert, R. L. Cone, and B. Jacquier, J. Luminescence **38**, 34 (1987); G. K. Liu and R. L. Cone, Phys. Rev. B **41**, 6193 (1990).

19. J. Huang, J. Zhang, A. Lezama, and T. W. Mossberg, Phys. Rev. Lett. **63**, 78 (1989); J. Huang, J. Zhang, and T. W. Mossberg, Opt. Commun. **75**, 29 (1990).

20. M. Mitsunaga, T. Takagahara, R. Yano, and N. Uesugi, Phys. Rev. Lett. **68**, 3216 (1992).

21. A. Maqsood, B. M. Wanklyn and G. Garton, J. Cryst. Growth **46,** 671 (1979).

22. J. Felsche, J. Less-Common Metals **21,** 1 (1970).

23. R. Orbach, Proc. R. Soc. London, Ser. A **264**, 458 (1961); D. E. McCumber and M. D. Sturge, J. Appl. Phys. **34**, 1682 (1963).

24. G. M. Wang, R. W. Equall, R. L. Cone, M. J. M. Leask, K. W. Godfrey, and F. R. Wondre, Opt. Lett. **21**, 818 (1996).

CHAPTER 5

SYMMETRY CONSIDERATIONS REGARDING LIGHT PROPAGATION AND LIGHT POLARIZATION FOR COHERENT INTERACTION WITH IONS IN CRYSTALS

Introduction

Coherent interactions of light beams with ions in crystals have been studied extensively.[1] Recently a number of new opto-electronic devices have been invented based on the principles of optical coherent transients, spectral holeburning, and spatial-spectral holography. Applications include time-domain optical data storage, real-time optical signal processing, and optical data routing in networks.[2-13] For a laser with arbitrary propagation and polarization directions the differently oriented sites in a crystal cause the coherent interaction of the laser and the ions to involve macroscopic material polarizations oscillating at a number of different optical "Rabi" frequencies; this difference in optical Rabi frequencies generally reduces the effectiveness of the devices as a result of optical interference and the associated complex transient material polarization behavior. For example, this interference can limit the system bandwidth (time response and data handling capability) in all of the application areas listed above. It can also reduce the diffraction efficiency (efficiency of signal selection or deflection) in

an optical data router for optical communications networks and wavelength-division multiplexing system.

In this chapter we provide a general solution to this material polarization interference problem for any crystal, resulting in a simple cooperative oscillation of all actively oscillating ions in the material at a single optical Rabi frequency and a consequent increase in the efficiency and bandwidth (speed-potential) of the optical electronic devices. The existence of this general solution means that the material polarization interference problem is no longer a constraint on the choice of active materials for constructing the optical-electronic devices; previously, efficiency could be optimized only for materials with orientationally equivalent sites.

Optical nutations have been used to study the coherent interaction. A detailed theory for optical nutation was provided by A. I. Alekseev and A. M. Basharov.[14] Here we give a brief introduction to optical nutation and use the results derived by A. I. Alekseev et al.

A perfect two-level system that is driven by a resonant, monochromatic field will exhibit optical nutation. If an atom is initially in the lower level, the probability that it will be in the upper state at t_0 after the field is switched on is

$$P_{upper} = \sin^2\left[\int_0^{t_0} (\mu E / \hbar) dt\right], \qquad (5.1)$$

where μ is the dipole transition strength and E is the optical electric field.

There are three groups of factors in a real system that can modify and damp the sinusoidal oscillation. First, spontaneous decay and other dephasing mechanisms will

change the phase and number of oscillating atoms, and consequently the nutation signal will show reduced modulation depth with time. Second, the laser frequency distribution and laser spatial distributions (transverse and longitudinal) over the sample will cause different ensembles of atoms to have different nutation frequencies; signals from the ensembles will beat with each other and damp the oscillation. Third, different sites in a crystal usually have different nutation frequencies due to the different projections of $\vec{E}$ along the local dipoles on orientationally-inequivalent sites. To observe the third effect, we carefully chose a two-level system consisting of the $^3H_4(1)$ and $^3H_6(1)$ electronic states of 0.1% Tm^{3+}:$Y_3Al_5O_{12}$. This crystal had been studied[13] and used for demonstrations in several applications.[12] It has a long spontaneous decay time (T_1 ~ 800 μs) and a long dephasing time (T_2 ~ 200 μs) at 1.4 K. In this system the first group of factors has much less effect than the second and the third. The second group of factors could significantly damp the oscillation. After integrating the laser frequency distribution and laser spatial distributions (transverse and longitudinal), for a square input laser pulse, the optical nutation signal shown on the transmitted light intensity is

$$I \propto (\mu E)^2 f(\mu E t), \tag{5.2}$$

where E is the electric field in the center of the distributions, f is a damped oscillating function with its shape dependent on the details of the distributions and its amplitude independent of E. For a crystal with different sites the third effect becomes important, and the nutation signal is

$$I \propto \sum_i (\mu E_i)^2 f(\mu E_i t), \tag{5.3}$$

where E_i is the projection of $\vec{E}$ along the local i dipole. Due to the beating between different frequencies, the sum normally has a complicated irregular shape and smaller oscillation amplitude than expected in a single dipole situation. Similar effects have been observed in atomic beam systems with magnetic substate degeneracy.[15,16]

An appropriately chosen $\vec{E}$ field direction in a crystal can make E_i in Eq. (5.3) the same for all excited dipoles and thus give a simple nutation signal like that given in Eq. (5.2) for a crystal with single dipole. The site structure and the selection rules for electric and magnetic dipole transitions for R^{3+}:$Y_3Al_5O_{12}$ were presented in Chapter 1. The transition dipoles necessarily lie along either x, y, or z for different states. Since the local x, y, z axes of the six sites are oriented differently from each other, even though the sites are crystallographically-equivalent, the six classes of dipoles (arising from the six classes of Y^{3+} sites) may be oriented differently. The electric or magnetic field vector generally makes unequal angles with each of the six classes of dipoles, resulting in unequal transition intensities for different sites and consequently different nutation frequencies. However when the electric or magnetic field vector is along certain special directions, the light field vector (light polarization) may have the same angles relative to all the excited dipoles resulting in the identical transition intensities. From the $Y_3Al_5O_{12}$ symmetry structure, we predicted two polarization directions applicable to the six transition dipoles in garnet. They are (111), (001) and their equivalents.

Experiment and Results

A 0.1% Tm^{3+}:$Y_3Al_5O_{12}$ crystal was cut with $(1\bar{1}0)$ and (111) faces, 3.6 mm along $(1\bar{1}0)$ and 5.3 mm along (111). The crystal was immersed in liquid helium at 1.4 K. The $^3H_6(1) \leftrightarrow {}^3H_4(1)$ transition (793.374 nm in vacuum) has a linewidth of 20 GHz, and an absorption coefficient of 2.1 cm^{-1} at the center of the transition.

The experimental setup is shown in Figure 51. A single mode cw ring Ti/sapphire laser (Coherent 899) pumped by an argon ion laser (Coherent Sabre 20/4) was used in this experiment. It has 1 MHz frequency jitter. A laser power controller (Cambridge LPC) maintained constant laser power on the crystal in different experimental conditions. Two A/O modulators were used to generate square pulses with 20 μs duration at 20 Hz repetition rate. The laser was focused into the A/O modulators to produce pulses with a fast rising edge of about 50 ns. An aperture was used to clip the edge of the collimated laser beam to make the transverse laser intensity distribution more uniform, thus reducing the damping of the nutation signal. Changing the laser polarization direction was accomplished by rotating a λ/2 retarder and a Glan-Taylor polarizing prism. An 8-cm lens was used to focus the laser onto the crystal with 14 μm waist radius. The crystal was oriented so that the laser propagated either along the $(1\bar{1}0)$ or the (111) direction. The transmitted light was measured by an EG&G FDN-100 photodiode and averaged with a digitizing oscilloscope.

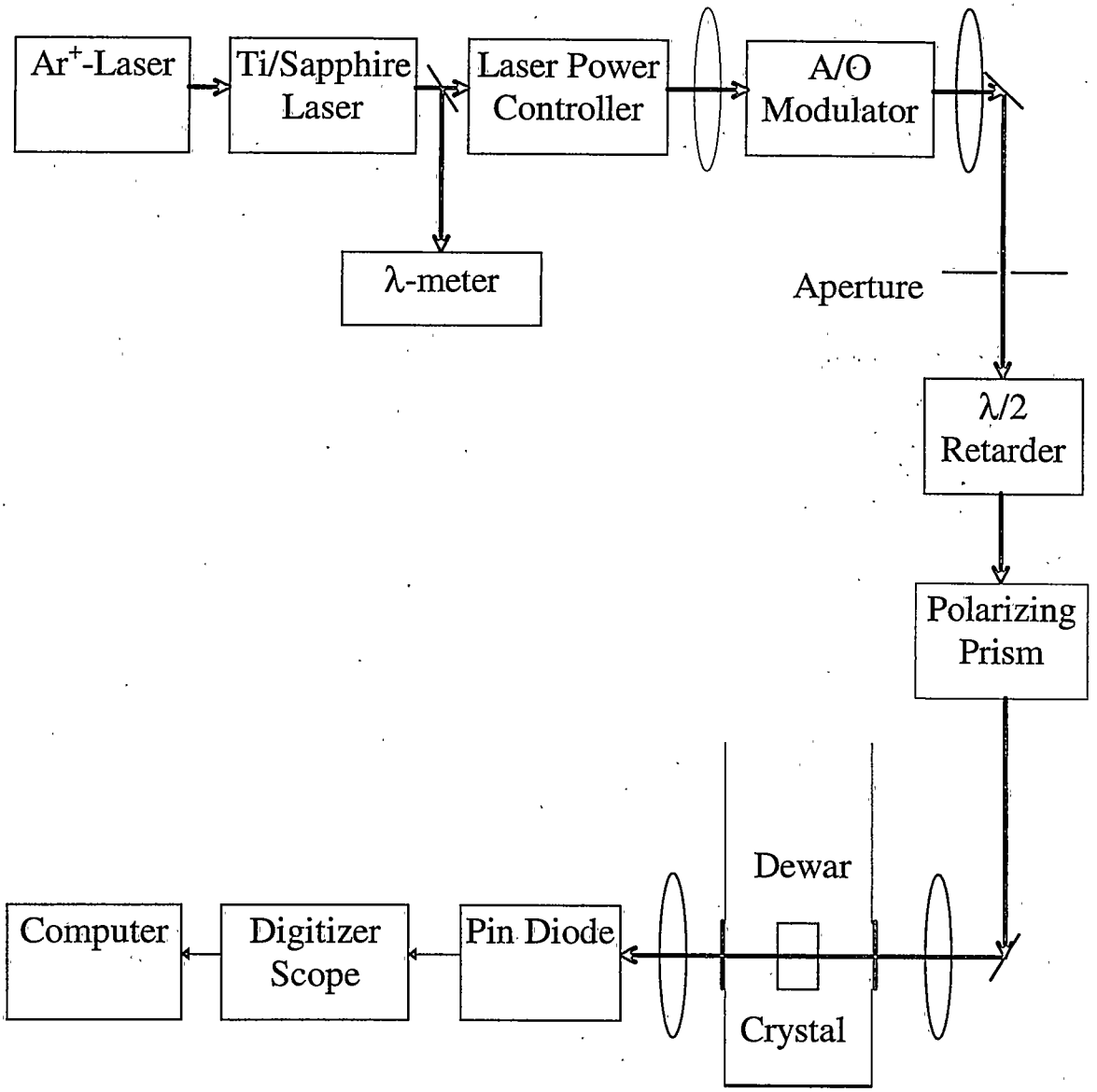

Figure 51. Schematic of the experimental setup for optical nutation.

Since $^3H_6(1)$ has Γ_2 symmetry and $^3H_4(1)$ has Γ_1 symmetry,[20] the $^3H_6(1) \leftrightarrow {}^3H_4(1)$ transition (793.374 nm in vacuum) is electric dipole allowed, and the transition dipole between these states is necessarily directed along the local y axis. When the electric field vector of the laser is along any of the three-fold symmetry axes [(111) and its equivalents], the laser induces transition at identical Rabi frequencies for 3 sites (# 1, 4, 6 in Figure 2) and has no interaction with the remaining three. Data are presented in Figure 52 for light propagating along the $(1\,\bar{1}\,0)$ direction, where the special single Rabi frequency optical nutation behavior for light polarized along (111) is evident for the solid trace. The dashed trace in Figure 52 shows another single Rabi frequency optical nutation which occurs for polarization along any of the crystal's four-fold symmetry axes [(001) and its equivalents], where the laser induces transitions at identical Rabi frequencies for 4 sites (# 3, 4, 5, 6 in Figure 2) and has no interaction with the remaining two. Using Eq. (5.3), the nutation signals for $\vec{E}$ along (111) and (001) are

$$I_{(111)} = 3C\left(\sqrt{\frac{2}{3}}E\right)^2 f\left(\sqrt{\frac{2}{3}}Et\right) \quad \text{and} \quad I_{(001)} = 4C\left(\sqrt{\frac{1}{2}}E\right)^2 f\left(\sqrt{\frac{1}{2}}Et\right).$$

From the above equations, we expect $I_{(111)}$ and $I_{(001)}$ to have the same amplitudes and the oscillation of $I_{(111)}$ to be 15% faster than $I_{(001)}$ under the same laser power. Both of these are consistent with the nutation traces shown Figure 52. The damping of each trace is mostly due to the laser spatial intensity distributions. Clipping the edge of the laser beam with an aperture improves the uniformity of the laser spatial intensity distributions and, in turn decreases the damping. The optical nutation signal $I_{(111)}$ was recorded as a function of laser power. The laser power was adjusted from 0.3 to 800 mW. We found the nutation

frequencies to be proportional to the laser electric field and nutation amplitudes proportional to the laser intensity as shown in Figure 53. These are expected according to Eq. (5.2).

The bottom trace of Figure 54 is an experimental nutation trace for $\vec{E}$ along a typical (multiple Rabi frequency) direction which is 12° from (110) and 78° from $(00\bar{1})$. Since $\vec{E}$ is in the $(1\,\bar{1}\,0)$ plane, it induces three kinds of transitions from site 1, sites 3 and 5, and sites 4 and 6. These three single dipole components can be calculated from the $I_{(111)}$ data by adjusting the amplitude and horizontal scale according to the projection of $\vec{E}$ on the dipoles. These calculated signals are plotted in Figure 54 and their sum according Eq. (5.3) is in good agreement with the real nutation data.

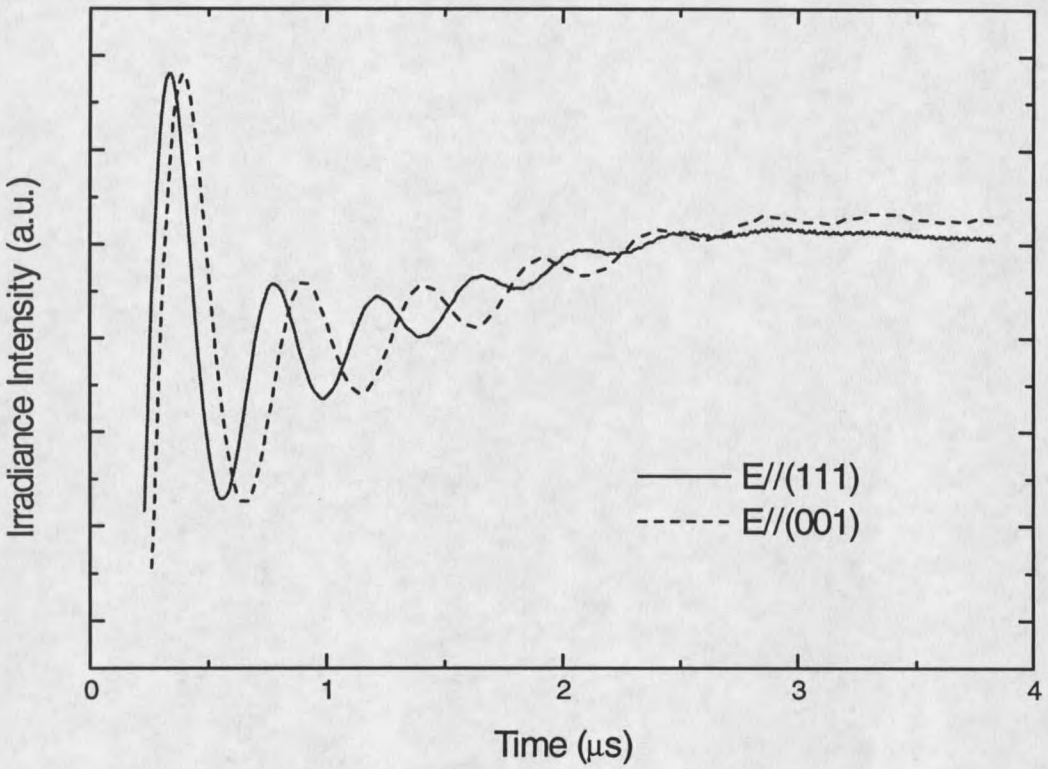

Figure 52. Observed nutation signal of the $^3H_6(1) \leftrightarrow {}^3H_4(1)$ transition of the 0.1% Tm^{3+}:$Y_3Al_5O_{12}$ crystal for a laser propagating along the $(1\,\bar{1}\,0)$ direction. The solid trace is with the light electric field polarized along (111), the dashed trace is with the light electric field along (001).

The optical nutation for light propagating along the (111) direction was also studied. As the electric field vector was rotated, the nutation signal was recorded. None of them has a special single Rabi frequency optical nutation behavior since the electric field vector does not have same projection on all the dipoles. We also observed that the nutation traces repeat themselves as the $\vec{E}$ was rotated by 60°, since the (111) direction is a three fold symmetry axis and the inversion symmetry of the electric dipoles.

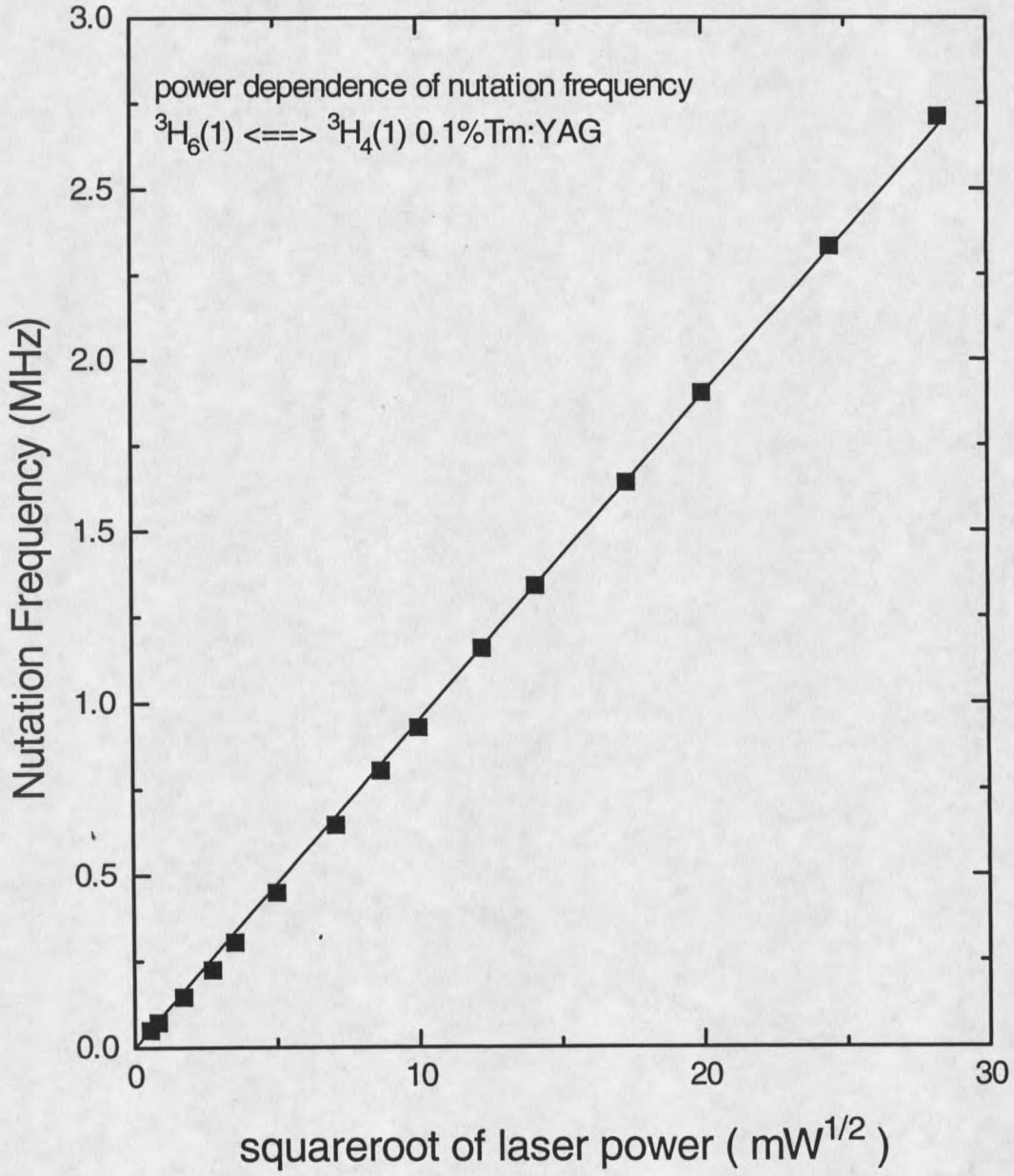

Figure 53. The nutation frequencies vs. the laser electric field. The laser electric field vector is along (111). The solid line is a linear fit through the origin.

In summary, after carefully considering the $Y_3Al_5O_{12}$ crystal symmetry, we found two special polarization directions (111) and (001), for which all sites being excited by the light have the same projection of the light field onto the transition dipoles. This was verified by optical nutation signals for Tm^{3+} in this host. In each of the "single-dipole" cases, the crystal exhibits the desired cooperative properties under coherent illumination. The complicated irregular shape of some optical nutation signals for arbitrary polarization directions is due to the beating of the different frequency signals from several sites in the crystal.

For arbitrary crystal symmetry, a general procedure for finding single Rabi frequency directions for a crystal with *m* independent transition dipole directions has been developed:

a) Find a direction with equal projections on a subset *n* of the *m* different local dipole directions ($n \leq m$) where *n* is chosen to make this direction perpendicular to the remaining (m-n) dipoles.

b) Propagate the light beam perpendicular to the direction chosen in step a).

c) Choose the light polarization along the direction chosen in step a).

This procedure was applied to Eu:Y_2O_3,[21-26] Pr:LaF_3,[27-30] Pr:$YAlO_3$,[29,31-35] and Eu:Y_2SiO_5[36-38] which have been extensively studied for optical coherent interactions. Single Rabi frequency directions were predicted for each of them. The detailed results are shown in Table 18.

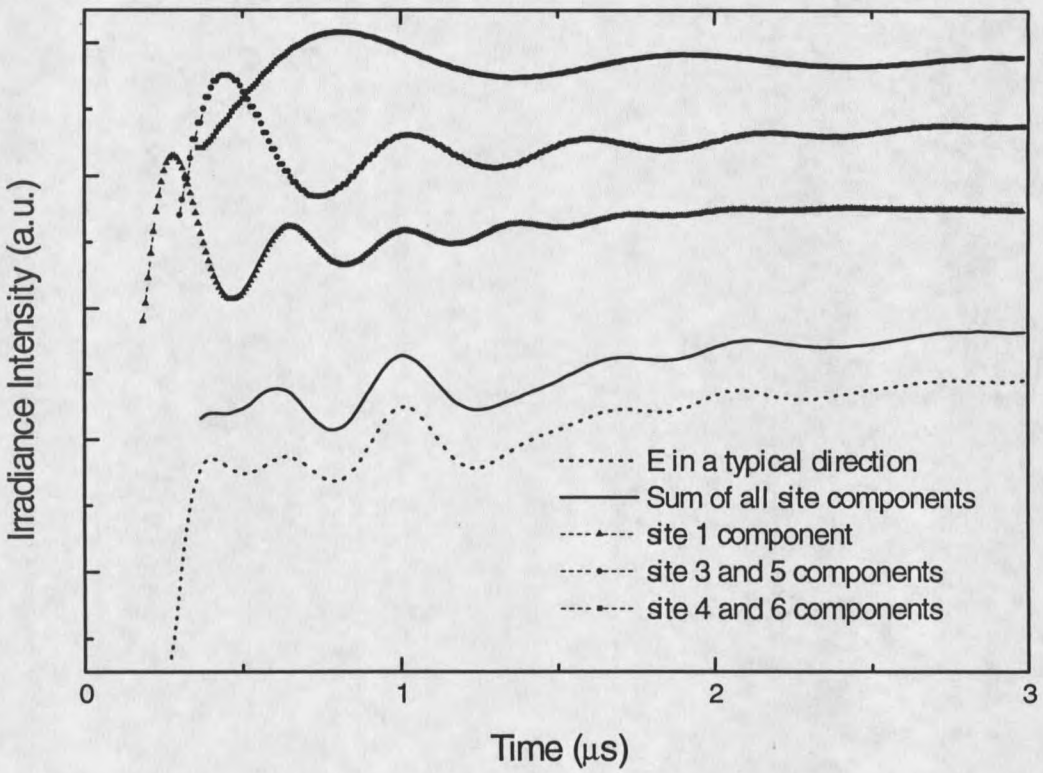

Figure 54. Nutation signal of the $^3H_6(1) \leftrightarrow {}^3H_4(1)$ transition of 0.1% Tm^{3+}:$Y_3Al_5O_{12}$ for a laser propagating along the $(1\,\bar{1}\,0)$ direction. The dotted trace is the experimental trace with the electric field vector of the light polarized 12° from (110) and 78° from $(00\,\bar{1})$. The three dashed traces are simulated nutation signals for the three kinds of dipoles using the single Rabi frequency data. The sum of the three dashed traces according to Eq. (3) is shown in the solid trace which is in good agreement with the experimental nutation data (dotted trace), for that direction.

Table 18. Single Rabi frequency directions for several important rare earth doped crystals.

	$Tm:Y_3Al_5O_{12}$	$Eu:Y_2O_3$	$Pr:LaF_3$	$Pr:YAlO_3$	$Eu:Y_2SiO_5$
Space Group	Cubic Ia3d	Cubic Ia3	Trigonal $P\bar{3}c1$	Orthorhombic Pbnm	Monoclinic C2/c
Site Symmetry	D_2	C_2 (C_{3i} nonactive)	C_2	C_{1h}	C_1 for two inequivalent crystallograpic sites
# of Orientationally-Inequivalent Sites	6	6	3	2	2 for each crystallographic site
Transition	$^3H_6(0) \leftrightarrow {}^3H_4(0)$	$^7F_0 \leftrightarrow {}^5D_0$	$^3H_4(0) \leftrightarrow {}^1D_2(0)$	$^3H_4(0) \leftrightarrow {}^1D_2(0)$	$^7F_0 \leftrightarrow {}^5D_0$
Dipole Nature and Directions	ED // (110) and its equivalents	ED // (001) and its equivalents.	ED // local C_2 axes which are $\perp$ crystal *c* axis	ED $\perp$ crystal *c* axis	NA
Single Rabi Frequency Directions	// (111), (001) and their equivalents(This work)	// (111), (001), (110) and their equivalents	$\perp$ any local C_2 axis, most efficient when also $\perp$ crystal *c* axis	In *ac* or *bc* plane, most efficient when // *a* axis or // *b* axis	In two planes which bisect the two dipole moments

Note: ED - Electric Dipole

Conclusion

In conclusion, a general procedure is provided to select a "single-dipole" in crystals. It was applied to the garnet system and two special directions were confirmed using optical nutation. In applications utilizing coherent interaction, this procedure solves the material polarization interference problem, while allowing use of materials with otherwise ideal properties that would have been rejected.

References for Chapter 5

1. L. Allen and J. H. Eberly, *Optical Resonance and Two-Level Atoms* (Dover, New York 1987); M. D. Levenson, *Introduction to Nonlinear Laser Spectroscopy* (Academic, New York, 1982). R. G. Brewer, in *Coherence in Spectroscopy and Modern Physics*, edited by F. T. Arecchi, R. Bonifacio and M. O. Scully (Plenum, New York, 1978), p. 41-84; A. Yariv, *Quantum Electronics* (Wiley, New York 1989).

2. *Persistent Spectral Hole-Burning: Science and Applications*, Vol. 44 Topics in Current Physics, Edited by W. E. Moerner, (Springer, 1988).

3. T. W. Mossberg, Opt. Lett. **7**, 77 (1982).

4. W. R. Babbitt and T. W. Mossberg, Opt. Comm. **65**, 185 (1988).

5. M. Mitsunaga, R. Yano, and N. Uesugi, Opt. Lett. **16**, 1890 (1991).

6. T. W. Mossberg Opt. Lett. **17**, 535 (1992).

7. R. Yano, M. Mitsunaga, and N. Uesugi, J. Opt. Soc. Am. B **9**, 992 (1992).

8. Y. S. Bai and R. Kachru, Opt. Lett. **18**, 1189 (1993); X. A. Shen, and R. Kachru, Opt. Lett. **18**, 1967 (1993); X. A. Shen, E. Chiang, and R. Kachru, Opt. Lett. **19**, 1246 (1994).

9. W. R. Babbitt and T. W. Mossberg, J. Opt. Soc. Am B **11**, 1948 (1994).

10. W. R. Babbitt and T. W. Mossberg, Opt. Lett. **20**, 910 (1995).

11. W. R. Babbitt and J. A. Bell, Appl. Opt. **33**, 1538 (1994).

12. H. Lin, T. Wang, G. A. Wilson, and T. W. Mossberg, Opt. Lett. **20**, 91 (1995); H. Lin, T. Wang, and T. W. Mossberg, Opt. Lett. **20**, 1658 (1995).

13. R. M. Macfarlane, Opt. Lett. **18**, 1958 (1993).

14. A. I. Alekseev and A. M. Basharov, J. Phys. B **15**, 4269 (1982).

15. B. W. Shore, Phys. Rev. A **17**, 1739 (1978).

16. A. Kastberg. P. Villemoes, A. Arnesen, F. Heijkenskjöld, and A. Langereis, Opt. Commun. **101**, 25 (1993).

17. S. Geller, Z. Kristallogr. **125**, 1 (1967).

18. J. R. Dillon, Jr., and L. R. Walker, Phys. Rev. **124**, 1401 (1961).

19. G. F. Koster, J. O. Dimmock, R. G. Wheeler, and H. Statz, *Properties of the Thirty-two Point Groups* (MIT Press, Cambridge, MA, 1963).

20. J. B. Gruber, M. E. Hills, R. M. Macfarlane, C. A. Morrison, G. A. Turner, G. J. Quarles, G. J. Kintz and L. Esterowitz, Spectra and energy levels of Tm^{3+}:$Y_3Al_5O_{12}$, Phys. Rev. B **40**, 9464 (1989).

21. J. Dexpert-Ghys and M. Faucher, Phys. Rev. B, **20**, 10 (1979).

22. R. M. Macfarlane and R. M. Shelby, Opt. Commun. **39**, 169 (1981).

23. W. R. Babbitt, A. Lezama and T. W. Mossberg, Phys. Rev. B **39**, 1987 (1989).

24. Jin Huang, J. M. Zhang, and T. W. Mossberg, Opt. Commun. **75**, 29 (1990).

25. G. P. Flinn, K. W. Jang, Joseph Ganem, M. L. Jones, R. S. Meltzer and R. M. Macfarlane, Phys. Rev. B **49**, 5821 (1994).

26. M. J. Sellars, R. S. Meltzer, P. T. H. Fisk, N. B. Manson, J. Opt. Soc. Am. B **11**, 1468 (1994).

27. A. Zalkin, D. H. Templeton and T. E. Hopkins, Inorg. Chem. **5**, 1466 (1966).

28. B. R. Reddy and L. E. Erickson, Phys. Rev. B **27**, 5217 (1983).

29. R. M. Macfarlane, R. M. Shelby, and R. L. Shoemaker, Phys. Rev. Lett. **43**, 1726 (1979).

30. S. C. Rand, A. Wokaun, R. G. DeVoe and R. G. Brewer, Phys. Rev. Lett. **43**, 1868 (1979).

31. S. Geller and E. A. Wood, Acta Crystallogr. **9**, 563 (1956).

32. G. H. Dieke, *Spectra of Energy Levels of Rare Earth Ions in Crystals* (Interscience, New York, 1968), p. 122.

33. L. E. Erickson, Phys. Rev. B **19**, 4412 (1979).

34. L. E. Erickson, Phys. Rev. B **24**, 5388 (1981).

35. M. Mitsunaga, E. S. Kintzer and R. G. Brewer, Phys. Rev. B **31**, 6947 (1985).

36. B. A. Maksimov, Yu. A. Kharitonov, V. V. Ilyukhin and N. V. Belov, Dokl. Akad, Nauk SSSR, **183**, 1072 (1968).

37. R. Yano, M. Mitsunaga, and N.. Uesugi, Opt. Lett. **16**, 1884 (1991), R. Yano, M. Mitsunaga, and N.. Uesugi, J. Opt. Soc. Am. **9**, 992 (1992).

38. R. W. Equall, Y. Sun, R. L. Cone, and R. M. Macfarlane, Phys. Rev. Lett. **72**, 2179 (1994).

CHAPTER 6

SUMMARY

A systematic study of defect and coherent transient optical spectroscopy of rare earth doped crystals has been presented.

In this study, the spectroscopic properties for R^{3+} doped $Y_3Al_5O_{12}$ crystals are related to the crystal structures. The ideal local symmetry of the Y^{3+} ions in $Y_3Al_5O_{12}$ crystal is D_2. When the R^{3+} ions are doped into the $Y_3Al_5O_{12}$ crystal, they will primarily substitute for the Y^{3+} ions, and one expects the D_2 symmetry to be preserved. The recorded transitions in white light absorption and fluorescence spectra of the R^{3+} ions were consistent with the transition selection rules of D_2 symmetry, confirming this expectation.

The R^{3+} ions in sites with D_2 symmetry have their nuclear principal axes constrained to (001), (1-10), and (110). These directions were measured and confirmed to within $\pm$ 2 degrees with the Raman heterodyne ODNMR on Pr^{3+}:$Y_3Al_5O_{12}$.

The D_2 symmetry was also confirmed in optical nutation measurements on Tm^{3+}:$Y_3Al_5O_{12}$. According to the local D_2 symmetry and garnet's cubic crystal symmetry, the optical nutation will show single Rabi frequency behavior, when a laser polarization is along one of the two special directions. These directions were experimentally verified

as along (111) and (001). A general procedure was provided to find single Rabi frequency directions for other crystals based on symmetry considerations.

Within ± 60 cm^{-1} of the intrinsic site optical transitions, weak satellite transitions were observed in white light absorption spectra. They are transitions of the R^{3+} ions in slightly perturbed Y^{3+} sites. A quantitative study of the absorption intensities indicates that 4-7% of the dopants appeared in the defect sites for the Eu^{3+}, Ho^{3+}, Er^{3+} and Tm^{3+} doped $Y_3Al_5O_{12}$ crystals, and 15-21% of the dopants appeared in the defect sites for Pr^{3+} and Nd^{3+} doped $Y_3Al_5O_{12}$ crystals. These percentages of the defect concentrations were found to be independent of the dopant concentration. It was known that during $Y_3Al_5O_{12}$ crystal growth at high temperature, a 1% excess of Y^{3+} ions substitute for Al^{3+} ions causing the composition to deviate slightly from stoichiometry. These excess Y^{3+} ions can perturb a certain small percentage of the normal Y^{3+} sites. When R^{3+} ions are doped into the crystal, some R^{3+} ions appear at these perturbed sites and possibly resulting in the weak satellite transitions mentioned above.

The structure and symmetry of defect sites for Pr^{3+}:$Y_3Al_5O_{12}$ crystal were investigated using Raman heterodyne ODNMR data. One defect site was determined to have C_1 symmetry. The defect site could be attributed to a perturbed Y^{3+} site with one of its nearest neighboring Al^{3+} ion substituted by an excess Y^{3+} ion. This substitution would reduce the local site symmetry from D_2 to C_1.

Further defect study on $Er_3Al_5O_{12}$ has been proposed. In addition to Er^{3+} ions in sites with D_2 symmetry, some excess Er^{3+} ions are expected to substitute for Al^{3+} ions in C_{3i} sites. Although the electric dipole transition of Er^{3+} in a C_{3i} site is forbidden, some

magnetic dipole transitions are allowed. A preliminary white light absorption measurement showed a set of vibronic transitions which might originate from the Er^{3+} in C_{3i} sites. More experiments for these magnetic dipole transition could provide new insights into defect site structure in garnets.

Optical dephasing measurements for $Tm^{3+}:Y_2Si_2O_7$ have also been presented. The optical dephasing for $Tm^{3+}:Y_2Si_2O_7$ has a strong temperature dependence that is due to phonon coupling between the closely spaced states $^3H_6(1)$ and $^3H_6(2)$. A homogeneous linewidth of 14 kHz was measured at 1.24 k for the $^3H_6(1) \rightarrow {}^3H_4(1)$ transition via photon echo measurements. The inhomogeneous linewidth of 100 GHz was measured via white light absorption. This relatively broad inhomogeneous linewidth combined with the narrow homogeneous linewidth, a transition wavelength suitable for GaAlAs semiconductor lasers, and the absence of hyperfine structure hole burning make this material an interesting candidate for time-domain signal processing and transient optically-addressed data storage.

APPENDIX

Programs for Angle Dependent ODNMR Data Analysis in $Y_3Al_5O_{12}$ Crystals

Batch File for Combining the Fitting, Drawing, and Plotting Programs with Data Files

```
REM all files to to "c:\users\guangming\program\fortran\datayag\defect"
CD c:\users\guangming\program\fortran\datayag\defect\
c:\users\guangming\program\fortran\angle_yg\angle_yg.exe
c:\users\guangming\program\fortran\drawyag\drawyag.exe
start c:\users\guangming\program\fortran\plotyag\plotyag.exe
```

Program: angle_yg.for

```
PROGRAM angle_yg
CC   Revised from angle_fit for YAG crystal fitting
CC   Nov. 1, 1996 by Guangming Wang
c    replace 16 with 48
c     this program need to link with the program fdf_yag
c     a fitting program to get the directions of the nuclear quadrupole
c     axes from angular dependent odnr zeeman data
c     x,y represent the data pairs
c     a holds the parameters to be fitted
c     b is the zeeman field at input and used as the measure of the
c     splittings later on
c     sig records the standard deviations for individual data points
c     chisq tells how good is the fit. chi squared
c     fdf_yag is the function to calculate the function fitting into y and its
c     jacobian.  See numerical recipes for the uses of the subroutines
c     typed in capital letters


      implicit none
      integer i,j,k,l,ma,lista(20),mfit,ndata(48)
      real x(48,100),y(48,100),xl,a(20),b,xxx,p,eta,z,test
      real sig(48,100),covar(20,20),alpha(20,20),chisq,alamda
      real alp,beta,gamma
      character*title*20
      external fdf_yag

c     total 8 parameters dependent, 6 are to be fitted
      mfit=6
      ma=6
c     xl is the conversion factor between degree and radian, pi/180
      xl=0.01745329

CC    input the parameters from 'param1.dat'
      open(unit=4,status='old',file='param1.dat')
CC    The units are: MHz, ,Gauss,degree,degree,degree,degree,kHz/g,kHz/g,kHz/g
      read(4,*)  p
      read(4,*)  eta
      read(4,*)  z
      read(4,*)  xxx
      read(4,*)  a(1)
```

```
      read(4,*)  a(2)
      read(4,*)  a(3)
      read(4,*)  a(4)
      read(4,*)  a(5)
      read(4,*)  a(6)
      close(unit=4)

C     debug used
      write(*,*)  p
      write(*,*)  eta
      write(*,*)  z
      write(*,*)  xxx
      write(*,*)  a(1)
      write(*,*)  a(2)
      write(*,*)  a(3)
      write(*,*)  a(4)
      write(*,*)  a(5)
      write(*,*)  a(6)
c     initialize the list of the parameters to be fitted
      do 1001 i=1,mfit
      lista(i)=i
1001  continue
c     input of the data
c     a fake standard deviation of each data point.
c     Better if we have them and read them in
c     namelist is the file that contains all the filenames of the
c     different lines in the spectrum
      open(unit=2,status='old',file='namelist.dat')
      do 1111 i=1,48
      read(2,1112)title
      read(2,1112)title
      if (title .eq. 'none')  then
      ndata(i)=0
      goto 1111
      end if
      open(unit=3,status='old',file=title)
      write(*,*)title
      do 1113 k=1,100
      read(3,*,end=1115)x(i,k),y(i,k)
c     write(*,*)x(i,k),y(i,k)
      x(i,k)=(x(i,k)-xxx)*xl

1113  continue
```

```
1115  ndata(i)=k-1
      close(unit=3)
1111  continue
1112  format(a20)
C     1114  format(2f13.6)
      close(unit=2)
      do 3001 j=1,48
      do 3002 k=1,100
      sig(j,k)=0.04
3002  continue
3001  continue



c       1.0559 MHz/KG for 151Eu nuclei.
      a(1)=a(1)*xl
      a(2)=a(2)*xl
      a(3)=a(3)*xl
      a(4)=a(4)*z/1000
      a(5)=a(5)*z/1000
      a(6)=a(6)*z/1000

c       a(4-6) correspond to betas now
c       required alamda < 0 to initialize the program
      alamda=-0.1
      test=0
      do 1002 j=1,100
      write (*,*) 'start looping'
      call mrqmin(x,y,sig,ndata,a,ma,lista,mfit,
     &          covar,alpha,mfit,chisq,fdf_yag,alamda)
      write (*,*) 'end looping'
c       converting back to what we like to see
      write (*,*) 'Iteration number =', j
      write(*,*)a(1)/xl,a(2)/xl,a(3)/xl
      write(*,*)1000*a(4)/z,1000*a(5)/z,1000*a(6)/z
      write(*,*) 'chisq=',chisq
      test=abs(test-chisq)
      write(*,*) 'test=',test
      if( test .lt. 0.0001*chisq ) then

      write(*,*)'give a one digit number to continue, 2 digit to stop'
      read(*,*)k
      if(k .lt. 10)  goto 1002
```

```
      alamda=0.
      call mrqmin(x,y,sig,ndata,a,ma,lista,mfit,
     &          covar,alpha,mfit,chisq,fdf_yag,alamda)
      write(*,*)a(1)/xl,a(2)/xl,a(3)/xl
      write(*,*)1000*a(4)/z,1000*a(5)/z,1000*a(6)/z
      write(*,*)chisq


CC    Output the parameters to 'param1.dat'
      open(unit=4,status='old',file='param1.dat')
      write(4,*)  p
      write(4,*)  eta
      write(4,*)  z
      write(4,*)  xxx
      write(4,*)  a(1)/xl
      write(4,*)  a(2)/xl
      write(4,*)  a(3)/xl
      write(4,*)  1000*a(4)/z
      write(4,*)  1000*a(5)/z
      write(4,*)  1000*a(6)/z
      close(unit=4)
      goto 1014
      else
      test=chisq
      end if
1002  continue

1014  write(*,*)'done'
      end



c     These routines are copied from Numerical recipes
      SUBROUTINE MRQMIN(x,y,SIG,NDATA,A,MA,LISTA,MFIT,
     *    COVAR,ALPHA,NCA,CHISQ,FUNCS,ALAMDA)
      PARAMETER (MMAX=20)
      DIMENSION X(48,100),Y(48,100),SIG(48,100),A(MA),LISTA(MA),
     *
COVAR(NCA,NCA),ALPHA(NCA,NCA),ATRY(MMAX),BETA(MMAX),DA(MMA
X)
      DIMENSION NDATA(48)
      external funcs
```

```
      real alamda
      IF(ALAMDA .LT. 0)THEN
      KK=MFIT+1
      DO 12 J=1,MA
       IHIT=0
       DO 11 K=1,MFIT
        IF(LISTA(K).EQ.J)IHIT=IHIT+1
11       CONTINUE
       IF (IHIT.EQ.0) THEN
        LISTA(KK)=J
        KK=KK+1
       ELSE IF (IHIT.GT.1) THEN
        PAUSE 'Improper permutation in LISTA'
       ENDIF
12     CONTINUE
      IF (KK.NE.(MA+1)) PAUSE 'Improper permutation in LISTA'
      ALAMDA=0.001
      CALL
MRQCOF(X,Y,SIG,NDATA,A,MA,LISTA,MFIT,ALPHA,BETA,NCA,CHISQ,
     & FUNCS)
      OCHISQ=CHISQ
      DO 13 J=1,MA
       ATRY(J)=A(J)
13     CONTINUE
      ENDIF
      DO 15 J=1,MFIT
      DO 14 K=1,MFIT
       COVAR(J,K)=ALPHA(J,K)
14     CONTINUE
      COVAR(J,J)=ALPHA(J,J)*(1.+ALAMDA)
      DA(J)=BETA(J)
15    CONTINUE
      CALL GAUSSJ(COVAR,MFIT,NCA,DA,1,1)
      IF(ALAMDA.EQ.0.)THEN
      CALL COVSRT(COVAR,NCA,MA,LISTA,MFIT)
      RETURN
      ENDIF
      DO 16 J=1,MFIT
      ATRY(LISTA(J))=A(LISTA(J))+DA(J)
16    CONTINUE
      CALL
MRQCOF(X,Y,SIG,NDATA,ATRY,MA,LISTA,MFIT,COVAR,DA,NCA,CHISQ,
     & funcs)
```

```
      IF(CHISQ.LT.OCHISQ)THEN
      ALAMDA=0.1*ALAMDA
      OCHISQ=CHISQ
      DO 18 J=1,MFIT
       DO 17 K=1,MFIT
        ALPHA(J,K)=COVAR(J,K)
17       CONTINUE
       BETA(J)=DA(J)
       A(LISTA(J))=ATRY(LISTA(J))
18     CONTINUE
      ELSE
      ALAMDA=10.*ALAMDA
      CHISQ=OCHISQ
      ENDIF
      RETURN
      END

c     called by mrqmin
      SUBROUTINE MRQCOF(X,Y,SIG,ndata,A,MA,LISTA,MFIT,ALPHA,BETA,
     * NALP,CHISQ,FUNCS)
      PARAMETER (MMAX=20)
      DIMENSION X(48,100),Y(48,100),SIG(48,100),ALPHA(NALP,NALP),
     * BETA(MA),DYDA(MMAX),LISTA(MFIT),A(MA),ndata(48)
      DO 12 J=1,MFIT
      DO 11 K=1,J
       ALPHA(J,K)=0.
11     CONTINUE
      BETA(J)=0.
12    CONTINUE
      CHISQ=0.
      DO 151 JJ=1,48
      IF(NDATA(JJ) .LE. 1) GOTO 151
      DO 15 I=1,NDATA(JJ)
      CALL FUNCS(X(JJ,I),A,YMOD,DYDA,MA,JJ)
      SIG2I=1./(SIG(JJ,I)*SIG(JJ,I))
      DY=Y(JJ,I)-YMOD
      DO 14 J=1,MFIT
       WT=DYDA(LISTA(J))*SIG2I
       DO 13 K=1,J
        ALPHA(J,K)=ALPHA(J,K)+WT*DYDA(LISTA(K))
13      CONTINUE
       BETA(J)=BETA(J)+DY*WT
14     CONTINUE
```

```
      CHISQ=CHISQ+DY*DY*SIG2I
15    CONTINUE
151     CONTINUE
      DO 17 J=2,MFIT
      DO 16 K=1,J-1
       ALPHA(K,J)=ALPHA(J,K)
16     CONTINUE
17    CONTINUE
      RETURN
      END

c called by Mrqmin
      SUBROUTINE COVSRT(COVAR,NCVM,MA,LISTA,MFIT)
      DIMENSION COVAR(NCVM,NCVM),LISTA(MFIT)
      DO 12 J=1,MA-1
      DO 11 I=J+1,MA
       COVAR(I,J)=0.
11     CONTINUE
12    CONTINUE
      DO 14 I=1,MFIT-1
      DO 13 J=I+1,MFIT
       IF(LISTA(J).GT.LISTA(I)) THEN
        COVAR(LISTA(J),LISTA(I))=COVAR(I,J)
       ELSE
        COVAR(LISTA(I),LISTA(J))=COVAR(I,J)
       ENDIF
13     CONTINUE
14    CONTINUE
      SWAP=COVAR(1,1)
      DO 15 J=1,MA
      COVAR(1,J)=COVAR(J,J)
      COVAR(J,J)=0.
15    CONTINUE
      COVAR(LISTA(1),LISTA(1))=SWAP
      DO 16 J=2,MFIT
      COVAR(LISTA(J),LISTA(J))=COVAR(1,J)
16    CONTINUE
      DO 18 J=2,MA
      DO 17 I=1,J-1
       COVAR(I,J)=COVAR(J,I)
17     CONTINUE
18    CONTINUE
      RETURN
```

```
      END
c     called by mrqcof
      SUBROUTINE GAUSSJ(A,N,NP,B,M,MP)
      PARAMETER (NMAX=50)
      DIMENSION
A(NP,NP),B(NP,MP),IPIV(NMAX),INDXR(NMAX),INDXC(NMAX)
      DO 11 J=1,N
      IPIV(J)=0
11    CONTINUE
      DO 22 I=1,N
      BIG=0.
      DO 13 J=1,N
       IF(IPIV(J).NE.1)THEN
        DO 12 K=1,N
         IF (IPIV(K).EQ.0) THEN
        IF (ABS(A(J,K)).GE.BIG)THEN
        BIG=ABS(A(J,K))
        IROW=J
        ICOL=K
        ENDIF
         ELSE IF (IPIV(K).GT.1) THEN
      PAUSE 'Singular matrix'
         ENDIF
12        CONTINUE
       ENDIF
13     CONTINUE
      IPIV(ICOL)=IPIV(ICOL)+1
      IF (IROW.NE.ICOL) THEN
       DO 14 L=1,N
        DUM=A(IROW,L)
        A(IROW,L)=A(ICOL,L)
        A(ICOL,L)=DUM
14      CONTINUE
       DO 15 L=1,M
        DUM=B(IROW,L)
        B(IROW,L)=B(ICOL,L)
        B(ICOL,L)=DUM
15      CONTINUE
      ENDIF
      INDXR(I)=IROW
      INDXC(I)=ICOL
      IF (A(ICOL,ICOL).EQ.0.) PAUSE 'Singular matrix.'
      PIVINV=1./A(ICOL,ICOL)
```

```
      A(ICOL,ICOL)=1.
      DO 16 L=1,N
       A(ICOL,L)=A(ICOL,L)*PIVINV
16     CONTINUE
      DO 17 L=1,M
       B(ICOL,L)=B(ICOL,L)*PIVINV
17     CONTINUE
      DO 21 LL=1,N
       IF(LL.NE.ICOL)THEN
        DUM=A(LL,ICOL)
        A(LL,ICOL)=0.
        DO 18 L=1,N
         A(LL,L)=A(LL,L)-A(ICOL,L)*DUM
18      CONTINUE
        DO 19 L=1,M
      B(LL,L)=B(LL,L)-B(ICOL,L)*DUM
19        CONTINUE
       ENDIF
21     CONTINUE
22    CONTINUE
      DO 24 L=N,1,-1
      IF(INDXR(L).NE.INDXC(L))THEN
       DO 23 K=1,N
        DUM=A(K,INDXR(L))
        A(K,INDXR(L))=A(K,INDXC(L))
        A(K,INDXC(L))=DUM
23      CONTINUE
      ENDIF
24    CONTINUE
      RETURN
      END
```

Program: fdf_yag.for

```
CC   Revised from fdf for YAG crystal fitting
CC   Nov. 1, 1996 by Guangming Wang
c     this is a subroutine to be used by the angle_yg program
c     it calculates eigenvalues of the nuclear quadruple hamiltonian and
c     the difference between certain two sets of the eigenvalue.
c     At the same time, it will calculate the jacobian relative to the
c     parameters
c     x is the angle data and y is the frequency data
c     a in the order of alpha,beta,gamma,bx,by,bz

      subroutine fdf_yag(x,a,y,dyda,na,label)
          dimension a(na),dyda(na),b(8)
          y=f(a,x,label)
          do 11 i=1,na
          b(i)=a(i)+0.0001
          dyda(i)=(f(b,x,label)-y)/0.0001
          b(i)=a(i)
11      continue
          return
          end

c     depending which curve we are fitting to,the arguments of d should be
c     changed, lup is the upper level
c     llo is the lower level of the transition
c     lal tells where we are looking
c     1----closest to the c-a plane
c     2 and 3 looking through ca' plane
c     4---- farthest
          function f(para,x,label)
      real para(8),x,a(12,12),d(12),v(12,12),eta,dir(3),eul(3,3),hpi,phi
          integer nrot,n,np,label,label1,upper,lower
      integer s
      real coord(12,3)
          external jacobi
          n=12
          np=12
c     intrinsic site  11.36, 0.733    defect 8.773, 0.6172
c      p=11.36
c     eta=0.733
```

```
      p=8.773
      eta=0.6172
C     twelve sites under cubic symmetry
      label1=mod(label,4)
      if(label1 .eq. 1) then
      upper= 5
      lower= 11
      else if(label1 .eq. 2) then
      upper= 5
      lower= 9
      else if(label1 .eq. 3) then
      upper= 7
      lower= 11
      else
      upper= 7
      lower= 9
      end if

      s=int((label-1)/4)+1
      coord(s,1)=(-1)**(s+1)*para(1)-1.5707963*(int((s+1)/2)-1)
      coord(s,2)=para(2)
      coord(s,3)=(-1)**(s+1)*para(3)
      call euler(coord(s,1), coord(s,2), coord(s,3),eul)

C     field direction rotate from 001 to 110
C     the 4 top sites and the 8 side sites have different views
      if (s .LE. 4) then
       dir(1)=sin(x)/2**0.5
       dir(2)=sin(x)/2**0.5
       dir(3)=cos(x)
      else
       dir(1)=-cos(x)
       dir(2)=sin(x)/2**0.5
       dir(3)=sin(x)/2**0.5
      end if

          call trans(eul,dir)
          call matrix(a,p,eta,dir,para)
          call jacobi(a,n,np,d,v,nrot)
          call eigsrt(d,v,n,np)
          f=d(upper)-d(lower)
          return
          end
```

```
c
      subroutine matrix(a,p,eta,dir,para)
      dimension a(12,12),a1(6,6),b(6,6),para(6)
      real eta,dir(3),p,bx,by,bz,x,y,z,xi,xi0
      integer i,j,k
c     this is to create a hamiltonian matrix for nuclear quadruple and
c     nuclear zeeman interaction, according to p.8.5 of Hansen thesis
c     real part of the matrix,symmetric
      bx=para(4)
      by=para(5)
      bz=para(6)
      do 1100 i=1,12
      do 1200 j=1,12
      a(i,j)=0.
1200  continue
1100  continue

      do 10 i=1,6
      do 20 j=1,i
      a1(i,j)=0.
20    continue
10    continue
      x=dir(3)*bz
      y=dir(1)*bx
      a1(1,1)=10.*p/3.+2.5*x
      a1(2,1)=sqrt(5.)/2.*y
      a1(3,1)=sqrt(10.)*eta*p/3.
      a1(2,2)=-2.*p/3.+1.5*x
      a1(3,2)=sqrt(2.)*y
      a1(4,2)=sqrt(2.)*eta*p
      a1(3,3)=-8.*p/3.+x/2.
      a1(4,3)=1.5*y
      a1(5,3)=a1(4,2)
      a1(4,4)=-8./3.*p-x/2.
      a1(5,4)=a1(3,2)
      a1(6,4)=a1(3,1)
      a1(5,5)=-2.*p/3.-1.5*x
      a1(6,5)=a1(2,1)
      a1(6,6)=10.*p/3.-2.5*x
      do 30 i=1,6
      do 40 j=i,6
      a1(i,j)=a1(j,i)
40    continue
```

```
30    continue

cc    imaginary part, b(i,j)=-b(j,i)
c     only three independent quatities
        x=by*dir(2)
        y=sqrt(2.)*x
        z=1.5*x
        x=sqrt(5.)/2.*x
        do 50 i=1,6
        do 60 j=1,i
        b(i,j)=0.
60    continue
50    continue
        b(2,1)=x
        b(3,2)=y
        b(4,3)=z
        b(5,4)=y
        b(6,5)=x
        do 70 i=1,6
        do 80 j=i,6
        b(i,j)=-b(j,i)
80    continue
70    continue

cc    completed
cc    need to put these two together
cc    |a1  -b|
cc    |b   a1|
c     this is a symmetric matrix
        do 110  i=1,6
        do 100  j=1,6
        a(i,j)=a1(i,j)
100   continue
110   continue
        do 130  i=1,6
        do 120  j=7,12
        a(i,j)=-b(i,j-6)
120   continue
130   continue
        do 150 i=7,12
        do 140 j=1,6
        a(i,j)=b(i-6,j)
140   continue
```

```
150   continue
      do 170 i=7,12
      do 160 j=7,12
      a(i,j)=a1(i-6,j-6)
160   continue
170   continue

      return
      end


c     copied from numerical recipes, eigsrt puts eigenvalues in order
c       according to the magnitude
      SUBROUTINE EIGSRT(D,V,N,NP)
      DIMENSION D(NP),V(NP,NP)
      DO 13 I=1,N-1
         K=I
         P=D(I)
         DO 11 J=I+1,N
          IF(D(J).GE.P)THEN
            K=J
            P=D(J)
          ENDIF
11       CONTINUE
         IF(K.NE.I)THEN
          D(K)=D(I)
          D(I)=P
          DO 12 J=1,N
            P=V(J,I)
            V(J,I)=V(J,K)
            V(J,K)=P
12        CONTINUE
         ENDIF
13    CONTINUE
      RETURN
      END

c       Jocobi method to find the eigenvalues of a matrix
      SUBROUTINE JACOBI(A,N,NP,D,V,NROT)
      PARAMETER (NMAX=100)
      DIMENSION A(NP,NP),D(NP),V(NP,NP),B(NMAX),Z(NMAX)
      DO 12 IP=1,N
         DO 11 IQ=1,N
```

```
          V(IP,IQ)=0.
11      CONTINUE
          V(IP,IP)=1.
12    CONTINUE
      DO 13 IP=1,N
          B(IP)=A(IP,IP)
          D(IP)=B(IP)
          Z(IP)=0.
13    CONTINUE
      NROT=0
      DO 24 I=1,50
          SM=0.
          DO 15 IP=1,N-1
           DO 14 IQ=IP+1,N
            SM=SM+ABS(A(IP,IQ))
14        CONTINUE
15      CONTINUE
          IF(SM.EQ.0.)RETURN
          IF(I.LT.4)THEN
           TRESH=0.2*SM/N**2
          ELSE
           TRESH=0.
          ENDIF
          DO 22 IP=1,N-1
           DO 21 IQ=IP+1,N
            G=100.*ABS(A(IP,IQ))
            IF((I.GT.4).AND.(ABS(D(IP))+G.EQ.ABS(D(IP)))
     *      .AND.(ABS(D(IQ))+G.EQ.ABS(D(IQ))))THEN
             A(IP,IQ)=0.
            ELSE IF(ABS(A(IP,IQ)).GT.TRESH)THEN
             H=D(IQ)-D(IP)
             IF(ABS(H)+G.EQ.ABS(H))THEN
                 T=A(IP,IQ)/H
             ELSE
                 THETA=0.5*H/A(IP,IQ)
                 T=1./(ABS(THETA)+SQRT(1.+THETA**2))
                 IF(THETA .LT. 0.)T=-T
             ENDIF
             C=1./SQRT(1+T**2)
             S=T*C
             TAU=S/(1.+C)
             H=T*A(IP,IQ)
             Z(IP)=Z(IP)-H
```

```
            Z(IQ)=Z(IQ)+H
            D(IP)=D(IP)-H
            D(IQ)=D(IQ)+H
            A(IP,IQ)=0.
            DO 16 J=1,IP-1
               G=A(J,IP)
               H=A(J,IQ)
               A(J,IP)=G-S*(H+G*TAU)
               A(J,IQ)=H+S*(G-H*TAU)
16          CONTINUE
            DO 17 J=IP+1,IQ-1
               G=A(IP,J)
               H=A(J,IQ)
               A(IP,J)=G-S*(H+G*TAU)
               A(J,IQ)=H+S*(G-H*TAU)
17          CONTINUE
            DO 18 J=IQ+1,N
               G=A(IP,J)
               H=A(IQ,J)
               A(IP,J)=G-S*(H+G*TAU)
               A(IQ,J)=H+S*(G-H*TAU)
18          CONTINUE
            DO 19 J=1,N
               G=V(J,IP)
               H=V(J,IQ)
               V(J,IP)=G-S*(H+G*TAU)
               V(J,IQ)=H+S*(G-H*TAU)
19          CONTINUE
            NROT=NROT+1
            ENDIF
21       CONTINUE
22    CONTINUE
         DO 23 IP=1,N
            B(IP)=B(IP)+Z(IP)
            D(IP)=B(IP)
            Z(IP)=0.
23    CONTINUE
24  CONTINUE
    PAUSE '50 iterations should never happen'
    RETURN
    END
c     the following gives the transformation matrix by euler angles
c     make sure the input for angles are in radians
```

```
      subroutine     euler(alp,bet,gam,eul)
      real alp,bet,gam,eul(3,3)
      eul(1,1)=-sin(alp)*sin(gam)+cos(alp)*cos(bet)*cos(gam)
      eul(1,2)=cos(alp)*sin(gam)+sin(alp)*cos(bet)*cos(gam)
      eul(1,3)=-sin(bet)*cos(gam)
      eul(2,1)=-sin(alp)*cos(gam)-cos(alp)*cos(bet)*sin(gam)
      eul(2,2)=cos(alp)*cos(gam)-sin(alp)*cos(bet)*sin(gam)
      eul(2,3)=sin(bet)*sin(gam)
      eul(3,1)=cos(alp)*sin(bet)
      eul(3,2)=sin(alp)*sin(bet)
      eul(3,3)=cos(bet)
      return
      end

      subroutine trans(eul,dir)
c     thos routine transforms the lab coordinates into the local
c     coordinates for the defects
      real eul(3,3),dir(3),x,y
      x=eul(1,1)*dir(1)+eul(1,2)*dir(2)+eul(1,3)*dir(3)
      y=eul(2,1)*dir(1)+eul(2,2)*dir(2)+eul(2,3)*dir(3)
      dir(3)=eul(3,1)*dir(1)+eul(3,2)*dir(2)+eul(3,3)*dir(3)
      dir(1)=x
      dir(2)=y
      return
      end
```

Program: drawyag.for

```
c     The method listed in section 11.4 in NR is used for the calculation of
c     the eigenvalues of the Hermitian matrix


cc    driver for routines of eigenvalue calculation
CC    Oct 29, 1996
CC    Revise from draw.for for YAG cubic symmetry
CC    16 sites
c     implicit none
c     a is the working matrix and also output the eigenvectors
c     d will output the eigenvalues
c     e is working array for nondiagonal elements. no useful output
      real a(12,12),d(12),e(12),v(12,12),dir(3)
c     lines(sites, transitions,angles)
      real l(12, 8, 100)
      real p,eta,theta,phi,beta,x(200),y,z,bx,by,bz,xi,xi0
c     coordinates (sites, angles)
      real alp,bet,gam, coord(12,3)
      real eul(3,3),dat1(2048),dat2(2048)
      integer i,j,k,n,np,nrot,m
      integer s,t
      n=12
      np=12
c         write(*,*)'input of p,eta'
c         read(*,*)p,eta
c         p=5.77
c         eta=0.0001

CC    input the parameters from 'param1.dat'
      open(unit=4,status='old',file='param1.dat')
      read(4,*)  p
      read(4,*)  eta
      read(4,*)  z
      read(4,*)  xi0
      read(4,*)  alp
      read(4,*)  bet
      read(4,*)  gam
      read(4,*)  bx
      read(4,*)  by
      read(4,*)  bz
```

```
      close(unit=4)

c       p=11.36
c       eta=0.733

c      bx=0.78
c      by=0.78
c      bz=0.78
      dpi=0.017453292
      alp=alp*dpi
      bet=bet*dpi
      gam=gam*dpi

C     twelve sites under cubic symmetry
      Do S=1, 12
      coord(s,1)=(-1)**(s+1)*alp-1.5707963*(int((S+1)/2)-1)
      coord(s,2)=bet
      coord(s,3)=(-1)**(s+1)*gam
      write(*,*) coord(s,1), coord(s,2), coord(s,3)
      END DO

      bx= bx*z/1000
      by= by*z/1000
      bz= bz*z/1000
      open(unit=2,status='old',file='data1.dat')

      DO 300 S=1, 12
      call euler(coord(s,1), coord(s,2), coord(s,3),eul)
      do 200 k=1,91
      x(k)=float(2*k-2)
      xi=dpi*x(k)
C     field direction rotate from 001 to 110
C     the 4 top sites and the 8 side sites have different views
      if (s .LE. 4) then
       dir(1)=sin(xi)/2**0.5
       dir(2)=sin(xi)/2**0.5
       dir(3)=cos(xi)
      else
       dir(1)=-cos(xi)
       dir(2)=sin(xi)/2**0.5
       dir(3)=sin(xi)/2**0.5
      end if
      call trans(eul,dir)
```

```
      call matrix(a,p,eta,dir,bx,by,bz)
      call jacobi(a,n,np,d,v,nrot)
      call eigsrt(d,a,n,np)
C     output transitions 3/2-5/2 and 1/2-3/2 to arrays
      l(s,1,k)=d(1)-d(7)
      l(s,2,k)=d(1)-d(5)
      l(s,3,k)=d(3)-d(7)
      l(s,4,k)=d(3)-d(5)
      l(s,5,k)=d(5)-d(11)
      l(s,6,k)=d(5)-d(9)
      l(s,7,k)=d(7)-d(11)
      l(s,8,k)=d(7)-d(9)
200   continue
300   continue
C     output transitions 3/2-5/2 and 1/2-3/2 to file
      do 400 k=1,91
      write(2,111) 2*k-2,(l(s,1,k),
     &l(s,2,k),l(s,3,k),l(s,4,k), s=1, 12),
     &(l(s,5,k),l(s,6,k),l(s,7,k),l(s,8,k),s=1, 12)
400   continue
      write(*,*) "finished"
111   format(I3,' ',96f6.2)
      stop
      end
c
      subroutine matrix(a,p,eta,dir,bx,by,bz)
      dimension a(12,12),a1(6,6),b(6,6)
      real eta,dir(3),p,bx,by,bz,x,y,z,xi,xi0
      integer i,j,k
c     this is to create a hamiltonian matrix for nuclear quadruple and
c     nuclear zeeman interaction, according to p.8.5 of Hansen thesis
c     real part of the matrix,symmetric
      do 1100 i=1,12
      do 1200 j=1,12
      a(i,j)=0.
1200  continue
1100  continue

      do 10 i=1,6
      do 20 j=1,i
      a1(i,j)=0.
20    continue
10    continue
```

```
      x=dir(3)*bz
      y=dir(1)*bx
      a1(1,1)=10.*p/3.+2.5*x
      a1(2,1)=sqrt(5.)/2.*y
      a1(3,1)=sqrt(10.)*eta*p/3.
      a1(2,2)=-2.*p/3.+1.5*x
      a1(3,2)=sqrt(2.)*y
      a1(4,2)=sqrt(2.)*eta*p
      a1(3,3)=-8.*p/3.+x/2.
      a1(4,3)=1.5*y
      a1(5,3)=a1(4,2)
      a1(4,4)=-8./3.*p-x/2.
      a1(5,4)=a1(3,2)
      a1(6,4)=a1(3,1)
      a1(5,5)=-2.*p/3.-1.5*x
      a1(6,5)=a1(2,1)
      a1(6,6)=10.*p/3.-2.5*x
      do 30 i=1,6
      do 40 j=i,6
      a1(i,j)=a1(j,i)
40    continue
30    continue

cc    imaginary part, b(i,j)=-b(j,i)
c     only three independent quatities
      x=by*dir(2)
      y=sqrt(2.)*x
      z=1.5*x
      x=sqrt(5.)/2.*x
      do 50 i=1,6
      do 60 j=1,i
      b(i,j)=0.
60    continue
50    continue
      b(2,1)=x
      b(3,2)=y
      b(4,3)=z
      b(5,4)=y
      b(6,5)=x
      do 70 i=1,6
      do 80 j=i,6
      b(i,j)=-b(j,i)
80    continue
```

```
70    continue

cc    completed
cc    need to put these two together
cc    |a1  -b|
cc    |b   a1|
c     this is a symmetric matrix
      do 110  i=1,6
      do 100  j=1,6
      a(i,j)=a1(i,j)
100   continue
110   continue
      do 130  i=1,6
      do 120  j=7,12
      a(i,j)=-b(i,j-6)
120   continue
130   continue
      do 150 i=7,12
      do 140 j=1,6
      a(i,j)=b(i-6,j)
140   continue
150   continue
      do 170 i=7,12
      do 160 j=7,12
      a(i,j)=a1(i-6,j-6)
160   continue
170   continue

      return
      end

c
      SUBROUTINE EIGSRT(D,V,N,NP)
      DIMENSION D(NP),V(NP,NP)
      DO 13 I=1,N-1
      K=I
      P=D(I)
      DO 11 J=I+1,N
       IF(D(J).GE.P)THEN
         K=J
         P=D(J)
       ENDIF
11    CONTINUE
```

```
      IF(K.NE.I)THEN
       D(K)=D(I)
       D(I)=P
       DO 12 J=1,N
        P=V(J,I)
        V(J,I)=V(J,K)
        V(J,K)=P
12      CONTINUE
      ENDIF
13    CONTINUE
      RETURN
      END

      SUBROUTINE JACOBI(A,N,NP,D,V,NROT)
      PARAMETER (NMAX=100)
      DIMENSION A(NP,NP),D(NP),V(NP,NP),B(NMAX),Z(NMAX)
      DO 12 IP=1,N
      DO 11 IQ=1,N
       V(IP,IQ)=0.
11     CONTINUE
      V(IP,IP)=1.
12    CONTINUE
      DO 13 IP=1,N
      B(IP)=A(IP,IP)
      D(IP)=B(IP)
      Z(IP)=0.
13    CONTINUE
      NROT=0
      DO 24 I=1,50
      SM=0.
      DO 15 IP=1,N-1
       DO 14 IQ=IP+1,N
        SM=SM+ABS(A(IP,IQ))
14      CONTINUE
15     CONTINUE
      IF(SM.EQ.0.)RETURN
      IF(I.LT.4)THEN
       TRESH=0.2*SM/N**2
      ELSE
       TRESH=0.
      ENDIF
      DO 22 IP=1,N-1
       DO 21 IQ=IP+1,N
```

```
      G=100.*ABS(A(IP,IQ))
      IF((I.GT.4).AND.(ABS(D(IP))+G.EQ.ABS(D(IP)))
     *    .AND.(ABS(D(IQ))+G.EQ.ABS(D(IQ))))THEN
       A(IP,IQ)=0.
      ELSE IF(ABS(A(IP,IQ)).GT.TRESH)THEN
       H=D(IQ)-D(IP)
       IF(ABS(H)+G.EQ.ABS(H))THEN
       T=A(IP,IQ)/H
       ELSE
       THETA=0.5*H/A(IP,IQ)
       T=1./(ABS(THETA)+SQRT(1.+THETA**2))
       IF(THETA.LT.0.)T=-T
       ENDIF
       C=1./SQRT(1+T**2)
       S=T*C
       TAU=S/(1.+C)
       H=T*A(IP,IQ)
       Z(IP)=Z(IP)-H
       Z(IQ)=Z(IQ)+H
       D(IP)=D(IP)-H
       D(IQ)=D(IQ)+H
       A(IP,IQ)=0.
       DO 16 J=1,IP-1
       G=A(J,IP)
       H=A(J,IQ)
       A(J,IP)=G-S*(H+G*TAU)
       A(J,IQ)=H+S*(G-H*TAU)
16       CONTINUE
       DO 17 J=IP+1,IQ-1
       G=A(IP,J)
       H=A(J,IQ)
       A(IP,J)=G-S*(H+G*TAU)
       A(J,IQ)=H+S*(G-H*TAU)
17       CONTINUE
       DO 18 J=IQ+1,N
       G=A(IP,J)
       H=A(IQ,J)
       A(IP,J)=G-S*(H+G*TAU)
       A(IQ,J)=H+S*(G-H*TAU)
18       CONTINUE
       DO 19 J=1,N
       G=V(J,IP)
       H=V(J,IQ)
```

```
        V(J,IP)=G-S*(H+G*TAU)
        V(J,IQ)=H+S*(G-H*TAU)
19        CONTINUE
        NROT=NROT+1
      ENDIF
21      CONTINUE
22    CONTINUE
    DO 23 IP=1,N
     B(IP)=B(IP)+Z(IP)
     D(IP)=B(IP)
     Z(IP)=0.
23    CONTINUE
24  CONTINUE
    PAUSE '50 iterations should never happen'
    RETURN
    END
    subroutine trans(eul,dir)
c     thos routine transforms the lab coordinates into the local
c     coordinates for the defects
    real eul(3,3),dir(3),x,y
    x=eul(1,1)*dir(1)+eul(1,2)*dir(2)+eul(1,3)*dir(3)
    y=eul(2,1)*dir(1)+eul(2,2)*dir(2)+eul(2,3)*dir(3)
    dir(3)=eul(3,1)*dir(1)+eul(3,2)*dir(2)+eul(3,3)*dir(3)
    dir(1)=x
    dir(2)=y
    return
    end

c     the following gives the transformation matrix by euler angles
c     make sure the input for angles are in radians
    subroutine     euler(alp,bet,gam,eul)
    real alp,bet,gam,eul(3,3)
    eul(1,1)=-sin(alp)*sin(gam)+cos(alp)*cos(bet)*cos(gam)
    eul(1,2)=cos(alp)*sin(gam)+sin(alp)*cos(bet)*cos(gam)
    eul(1,3)=-sin(bet)*cos(gam)
    eul(2,1)=-sin(alp)*cos(gam)-cos(alp)*cos(bet)*sin(gam)
    eul(2,2)=cos(alp)*cos(gam)-sin(alp)*cos(bet)*sin(gam)
    eul(2,3)=sin(bet)*sin(gam)
    eul(3,1)=cos(alp)*sin(bet)
    eul(3,2)=sin(alp)*sin(bet)
    eul(3,3)=cos(bet)
    return
    end
```

Program: plotwin.for

```
CC  plotwin.FOR
CC  some freq. used functions in this program
CC  0 black 7 white 1 blue
CC  status = setcolor(color)
CC  status = settextcolor(color)
CC  call settextposition (12,10,curpos)
CC  call outtext('HELLO WORLD!')
CC  CALL SETLINESTYLE( )
CC  CALL moveto_w( x,y,xy )
CC  status = LINETO_w( x ,y)


CC

      INCLUDE  'FGRAPH.FI'
      INCLUDE  'FGRAPH.FD'


      INTEGER*2  i, j,k, s,ndp
      INTEGER*2  status, x, y

c     datay(sites, transitions,angles)
      DOUBLE PRECISION datax(100), datay(12,8,100)
      real    rawx(2000), rawy(2000)
      DOUBLE PRECISION minx, miny, maxx, maxy, stepx, stepy, rx, ry
      character title*20
      real p, eta, z, xi0, alp, bet, gam, bx, by, bz



      RECORD / wxycoord /     xy
      RECORD / xycoord /     curpos
      RECORD / videoconfig / vc

CC    Find graphics mode.

      CALL GETVIDEOCONFIG( vc )
      x = vc.numxpixels
      y = vc.numypixels
```

```
CC    open file or (data1.dat) for inputting data


      write(*,*) 'Draw 1/2 <-> 3/2 lines for'
      write(*,*) 'data1.dat'
      ndp=0
      OPEN (UNIT = 12, FILE
     &='data1.dat')
      DO 100 i=1, 100
      read(12,*,end=101) datax(i),(datay(s,1,i),datay(s,2,i),
     &datay(s,3,i),datay(s,4,i), s=1,12),(datay(s,5,i),datay(s,6,i),
     &datay(s,7,i),datay(s,8,i),s=1,12)
      ndp=ndp+1
C     write (*,*) datax(i), datay(i)
100   continue

CC    find the min, max for setting up the plotting window


101   minx=datax(1)
      miny=datay(1,5,1)
      maxx=datax(1)
      maxy=datay(1,5,1)
      DO i=1, ndp
      if (minx .GT. datax(i))  minx=datax(i)
      if (maxx .LT. datax(i))  maxx=datax(i)
      END DO
      DO i=1, ndp
c     only 1/2 <-> 3/2 lines : j=5,8
      DO j=5, 8
      DO s=1, 12
      if (miny .GT. datay(s,j,i))  miny=datay(s,j,i)
      if (maxy .LT. datay(s,j,i))  maxy=datay(s,j,i)
      END DO
      END DO
      END DO
CC    extend 5% to each end of the axes
      minx=minx-(maxx-minx)/20
      maxx=maxx+(maxx-minx)/20
      miny=miny-(maxy-miny)/20
      maxy=maxy+(maxy-miny)/20

C     CALL CLEARSCREEN( $GVIEWPORT )
```

```
      CALL SETVIEWPORT( 220, 0, x, y-70)
      status = SETWINDOW( .TRUE., minx, miny, maxx, maxy )
      status = SETCOLOR(15)
      status = RECTANGLE_W( $GBORDER, minx, miny, maxx, maxy )
CC    Draw some  labels  and  some ticks
      stepx=(maxx-minx)/60
      stepy=(maxy-miny)/60
      DO i = 0 , 9
      call settextposition(62,int(25+13.3*i),curpos)
      write (*,200)  (minx+stepx*i*6)
      call settextposition(int(60-5.9*i),21,curpos)
      write (*,200)  (miny+stepy*i*6)
200   format (F8.2)

      CALL moveto_w( minx+stepx*i*6,miny, xy )
      status = LINETO_w(minx+stepx*i*6,miny+stepy)
      CALL moveto_w( minx,miny+stepy*i*6, xy )
      status = LINETO_w(minx+stepx,miny+stepy*i*6)
      CALL moveto_w( minx+stepx*i*6,maxy, xy )
      status = LINETO_w(minx+stepx*i*6,maxy-stepy)
      CALL moveto_w( maxx,miny+stepy*i*6, xy )
      status = LINETO_w(maxx-stepx,miny+stepy*i*6)
      END DO


CC    plotting the data1.dat (the resulting file from draw.exe)

      DO j=5, 8
      DO s=1, 12
      if (s .eq. 1) then
      status = setcolor(14)
      else
      status = setcolor(15)
      end if
      CALL moveto_w( datax(1),datay(s,j,1), xy )
      DO i=2, ndp
      status = LINETO_w(datax(i),datay(s,j,i))
      END DO
      END DO
      END DO
CC    plotting the data (the real data files in "namelist.dat")
      rx=stepx/5.0
      ry=stepy/5.0
```

```
      call settextposition(4,0,curpos)
      write(*,*) 'Plotting points for files in'
      write(*,*)  'namelist.dat'
      open(unit=2,status='old',file='namelist.dat')
      status = setcolor(14)
      do 1111 i=1,48
      read(2,1112) title
      read(2,1112) title
      if (title .eq. 'none')  then
      write(*,*) 'none'
      goto 1111
      end if
      open(unit=3,status='old',file=title)
      write(*,*)  title
      do 1113 k=1,100
      read(3,*,end=1115) datax(k),datay(1,i,k)
      status = ellipse_w($GFILLINTERIOR, datax(k)-rx, datay(1,i,k)+ry,
     + datax(k)+rx,  datay(1,i,k)-ry)
c     x(i,k)=x(i,k)-xxx
1113  continue
1115  close(unit=3)
1111  continue
      close(unit=2)
1112  format(a20)
1114  format(2f8.3)

CC    input the parameters from 'param1.dat'
      open(unit=4,status='old',file='param1.dat')
      read(4,*)  p
      read(4,*)  eta
      read(4,*)  z
      read(4,*)  xi0
      read(4,*)  alp
      read(4,*)  bet
      read(4,*)  gam
      read(4,*)  bx
      read(4,*)  by
      read(4,*)  bz
      close(unit=4)
CC    write the parameters to screen
      write(*, 1116)'p      ', p
      write(*,1116) 'eta    ', eta
```

```
      write(*,1116) 'z      ', z
      write(*,1116) 'xi0    ', xi0
      write(*,1116) 'alp    ', alp
      write(*,1116) 'beta   ', bet
      write(*,1116) 'gam    ', gam
      write(*,1116) 'bx     ', bx
      write(*,1116) 'by     ', by
      write(*,1116) 'bz     ', bz
1116  format(a9, f8.3)

CC    plotting the "raw.dat"
c     rx=rx/2.0
c     ry=ry/2.0
      open(unit=2,status='old',file='raw.dat')
      status = setcolor(7)
      do 2113 k=1,2000
      read(2,*,end=2115) rawx(k),rawy(k)
      status = ellipse_w($GBORDER, rawx(k)-rx, rawy(k)+ry,
     + rawx(k)+rx, rawy(k)-ry)
2113  continue
2115  close(unit=2)

      READ (*,*) ! Wait for ENTER to be pressed
      CALL CLEARSCREEN( $GVIEWPORT )

      END
```

MONTANA STATE UNIVERSITY LIBRARIES
3 1762 10293277 7